ELECTROSTATIC LAYER-BY-LAYER ASSEMBLY OF HYBRID THIN FILMS USING POLYELECTROLYTES AND INORGANIC NANOPARTICLES

A Dissertation
Presented to
The Academic Faculty

by

Chunqing Peng

In Partial Fulfillment
of the Requirements for the Degree
Doctor of Philosophy in the
School of Materials Science and Engineering

Georgia Institute of Technology
May, 2011

ELECTROSTATIC LAYER-BY-LAYER ASSEMBLY OF HYBRID THIN FILMS USING POLYELECTROLYTES AND INORGANIC NANOPARTICLES

Approved by:

Dr. Rosario A. Gerhardt, Advisor
School of Materials Science and Engineering
Georgia Institute of Technology

Dr. Yonathan S. Thio, Co-advisor
School of Materials Science and Engineering
Georgia Institute of Technology

Dr. Vladimir V. Tsukruk
School of Materials Science and Engineering
Georgia Institute of Technology

Dr. Yulin Deng
School of Chemical & Biomolecular Engineering
Georgia Institute of Technology

Dr. Sven H. Behrens
School of Chemical & Biomolecular Engineering
Georgia Institute of Technology

Date Approved: March 16, 2011

To my parents and my wife, for their unconditional love and support

ACKNOWLEDGEMENTS

First and foremost, I want to express my appreciation to my advisor Professor Rosario Gerhardt and my co-advisor Professor Yonathan Thio for their guidance and advisement through my Ph.D. study at Georgia Tech. Dr. Gerhardt's constant encouragement, invaluable input, and helpful suggestions to my work, as well as her endless passion for science made me become a real researcher. Dr Thio's creative questions and comments always encouraged me to continue exploring. I would also like to acknowledge the scholarship funding from Institute of Paper Science and Technology (IPST) at Georgia Tech.

I would like to thank my committee members, including Professor Vladimir Tsukruk, Professor Yulin Deng, and Professor Sven Behrens, for their helpful suggestions. In addition, I want thank Professor Nils Kröger and his group members for allowing me to use their Zetasizer unlimitedly. Thanks to Professor Tannenbaum's research group, especially Dr Lex Nunnery and Il Tae Kim, for frequent access to their equipment and helpful discussions. Thanks to Professor C.P. Wong and Dr Kyoung-Sik Moon for allowing me to use their UV/Ozone and TGA. Thanks to Professor Z.L. Wang and Dr Yong Ding for allowing me to use their UV/Vis/NIR Spectrophotometer. Thanks to Professor Faisal Alamgir for allowing me to obtain pure water from his lab. Thanks to Mr. Shaobo Pan in the IPST for his generous help and training for papermaking. Thanks to Dr Valeria Lauter, Dr Haile Ambaye, and Dr Ilia Ivanov at Oak Ridge National Lab (ORNL) for their help with the acquision and the simulation of neutron reflectometry experiments and the supply of some materials. Thanks to Salil Joshi for taking the TEM pictures, and thanks to Danny Jeong for help with some experiments. Thanks to Professor Eugenia Kharlampieva, Dr Veronika Kozlovskaya, Dr Zhe Cheng, Dr Fei Peng, James Hardin, Sehoon Chang, Ryan Kincer, Michelle Schlea, Xuxia Yao, Wei Zhang, Lei Yang,

Wei Lin, Zhuo Li, and many others who helped me with experiments and gave me suggestions.

I would like to express my appreciation for many past and present group members of both Professor Gerhardt's research group and Professor Thio's research group, including but not limited to Dr V. Siva Kumar G. Kelekanjeri, Dr Charles Capozzi, Dr. Cantwell Carson, Dr Mihir Oka, Dr Sungwon Ma, Dr Bilge Gurun, Brian Bertram, Jake Waddell, Laurissa Prystaj, John Boyea, Katie Campbell, Ricky Whelchel, Salil Joshi, Will Gibson, Tim Pruyn, Lianghui Huang, and Rachel Muhlbauer. Their assistance and friendship made my work and life in Georgia Tech enjoyable and memorable.

Last, but certainly not least, I want to thank my family for their unconditional love the unwavering support that they have offered me throughout my life. My parents and my sister are the best parents and sister that I could ask for, and they always understand, encourage, and support me throughout my life. I also very much appreciate the support of my parents-in-law in the past few years and many years to come. I feel I am the luckiest man on the earth to have my wife, Wei Zhuang, by my side. Without her love and support at every turn, my PhD and this thesis would not be possible.

TABLE OF CONTENTS

LIST OF TABLES

LIST OF FIGURES

LIST OF SYMBOLS AND ABBREVIATIONS

LbL	Layer-by-Layer
ITO	Indium tin oxide
ζ-potential	Zeta potential
IEP	Isoelectric point
PEI	Polyethyleneimine
PAH	poly(allylamine hydrochloride)
PDDA	poly(diallyldimethylammonium hydrochloride)
PSS	Poly(sodium 4-styrenesulfonate)
PAA	Poly(acrylic acid)
TCOs	Transparent conductive oxides
IR	Infrared
κ	Reciprocal Debye length
FTIR	Fourier Transform infrared spectroscopy
PEMs	Polyelectrolyte multilayers
PLL	Poly(l-Lysine)
MUA	Mercaptoundecanoic acid
SAM	Self-assembled monolayer
l-LbL	Linear LbL
e-LbL	Exponential LbL
MTM	Na^+-montmorillonite
CHI	Chitosan
TEM	Transmission electron microscopy
QCM	Quartz crystal microbalance

$-\Delta f$	Total frequency change of QCM crystals during LbL assembly
$\Delta(-\Delta f)$	Frequency change of QCM crystals per LbL assembly step
AFM	Atomic force microscopy
RMS	Root-mean-square
TGA	Thermogravimetric analysis
SEM	Scanning electron microscopy
EDS	Energy dispersive spectroscopy
EIS	Electrochemical impedance spectroscopy
SCE	Saturated calomel electrode
R_{ct}	Charge transfer resistance
Q_{dl}	Double layer capacitance
t_{dl}	Double layer thickness
R_s	Solution resistance
NR	Neutron reflectometry
SLD	Scattering length density
TOF	Time-of-flight
IP	In-plane
TT	Through-the-thickness
σ_{ac}	AC conductivity
σ_{dc}	DC conductivity
R_{dc}	DC resistance
β	*e*-LbL growth strength
CVD	Chemical vapor deposition

SUMMARY

Polymer/inorganic nanoparticle hybrid thin films, primarily composed of functional inorganic nanoparticles, are of great interest to researchers because of their interesting electronic, photonic, and optical properties. In the past two decades, layer-by-layer (LbL) assembly has become one of the most powerful techniques to fabricate such hybrid thin films. This method offers an easy, inexpensive, versatile, and robust fabrication technique for multilayer formation, with precisely controllable nanostructure and tunable properties. In this thesis, various ways to control the structure of hybrid thin films, primarily composed of polyelectrolytes and indium tin oxide (ITO), are the main topics of study. ITO is one of the most widely used conductive transparent oxides (TCOs) for applications such as flat panel displays, photovoltaic cells, and functional windows.

In this work, polyethyleneimine (PEI) was used to stabilize the ITO suspensions and improve the film buildup rate during the LbL assembly of poly(sodium 4-styrenesulfonate) (PSS) and ITO. The growth rate was doubled due to the stronger interaction forces between the PSS and PEI-modified ITO layer. The assembly of hybrid films was often initiated by a polyelectrolyte precursor layer, and the characteristics of the precursor layer were found to significantly affect the assembly of the hybrid thin films. The LbL assembly of ITO nanoparticles was realized on several substrates, including cellulose fibers, write-on transparencies, silicon wafers, quartz crystals, and glasses. By coating the cellulose fibers with ITO nanoparticles, a new type of conductive paper was manufactured. By LbL assembly of ITO on write-on transparencies, transparent conductive thin films with conductivity of 10^{-4} S/cm and transparency of over 80 % in the visible range were also prepared.

As a result of this work on the mechanisms and applications of LbL grown films, the understanding of the LbL assembly of polyelectrolytes and inorganic nanoparticles was significantly extended. In addition to working with ITO nanoparticles, this thesis also demonstrated the ability to grow bicomponent $[PEI/SiO_2]_n$ thin films. It was further demonstrated that under the right pH conditions, these films can be grown exponentially (*e*-LbL), resulting in much thicker films, consisting of mostly the inorganic nanoparticles, in much fewer assembly steps than traditional linearly grown films (*l*-LbL). These results open the door to new research opportunities for achieving structured nanoparticle thin films, whose functionality depends primarily on the properties of the nanoparticles.

CHAPTER 1

INTRODUCTION

In the past two decades, Layer-by-Layer (LbL) assembly has become one of the most powerful "bottom-up" nanofabrication techniques.[1-5] It offers an easy, inexpensive, versatile, and robust method for multilayer formation with precisely controllable nanostructure and allows a variety of materials to be incorporated within the film structure. Due to its versatility, it has been widely applied in interdisciplinary fields for applications such as sensors,[6-8] drug delivery,[9-11] biomimetic structures,[12-14] selective membranes,[15-17] and functionalized coatings.[18-20]

Hybrid LbL thin films, which incorporate functional inorganic nanoparticles, are of primary interest for this thesis, because of the possibility of controlling their electronic, photonic and optical properties.[21] Particularly, the thesis focuses on the fabrication of bicomponent hybrid LbL thin films, which incorporate one polyelectrolyte material and one type of inorganic nanoparticle. The functional inorganic nanoparticles incorporated into the LbL thin films in this study were indium tin oxide (ITO) nanoparticles. ITO is well-known for its optical transparency and its high electrical conductivity.[22-24] The transparent conductive thin films from ITO nanoparticles can be potentially used in optoelectronic devices, such as photovoltaic cells, electronic displays, and functional windows.[23] Compared to traditional film deposition methods, LbL assembly can increase the efficiency of the ITO utilization and allow for coatings to be deposited onto flexible and complex-shaped substrates.

The fundamental understanding of LbL assembly of thin films, composed of polyelectrolytes and inorganic nanoparticles, lags behind its wide applications.[17, 21] The LbL assembly of polyelectrolytes and inorganic nanoparticles often exhibits complex and contradictory responses to variables such as the ionic strength, pH, and the details of the

precursor layers used. For these reasons, this thesis will focus on these variables. In subsequent sections, a brief summary of the background literature will be given which focuses on all of the main topics related to the thesis: (1) Background on ITO, (2) Background on Colloidal Solutions, (3) Background on LbL Assembly.

1.1. Indium Tin Oxide (ITO)

Transparent conductive oxides (TCOs) materials were first discovered by Badeker et al. in 1907, when they found that Cd metal thin film deposited in a glow discharge chamber could be oxidized to become transparent while maintaining its conductivity.[25] Owing to their special properties of combining the high transparency and the high conductivity, TCOs have found wide application in the optoelectronic devices ranging from flat-panel displays to thin film photovoltaics.[23] Since the 1960s, the most widely used TCO for optoelectronic device applications has been tin-doped indium oxide, which is often called indium tin oxide (ITO).[24, 26, 27]

The transparency of ITO is due to the Sn doping into indium oxide.[28] As shown in the figure, prior to doping, the conduction band is unfilled, and the energy required to excite an electron from the filled valence band to the conduction band is E_{g0}. Due to the doping, the bottom of the conduction band is filled with free electron, and thus the energy required to excite an electron from the valence band to the lowest unfilled state in the conduction band is increased to E_g. This band-gap widening due to the blocking of the bottom of the conduction band from the doping is well known as the Burstein-Moss shift.[29, 30] The band energy increase of ΔE_g is a function of the electron density, as well as the density-of-states effective electron masses in the valence band and the conduction band.[31] The intrinsic band gap of the single crystalline In_2O_3 is 3.75 eV,[32] while the band-gap widening (ΔE_g) at an electron density of ~10^{21} cm^{-3} can be as much as 0.8 eV.[28]

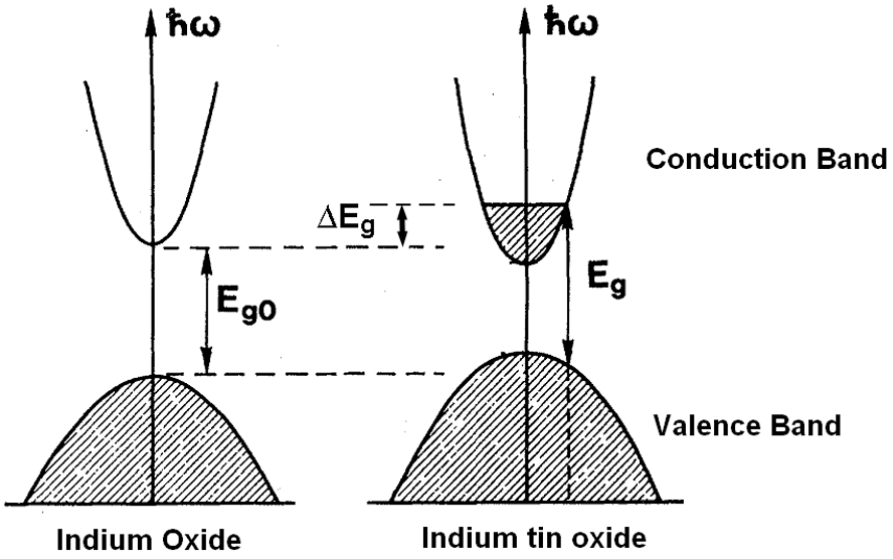

Figure 1.1 Schematic of the band-gap shift from indium oxide to the indium tin oxide due to the doping.[28] (The figure has been modified from the reference.)

The transmittance of ITO thin films is dependent on the free electron density (n_e). As shown in Figure 1.2, the ITO transmittance in the visible range is around 80%. This transmittance will decrease to zero due to the plasma edge in the infrared (IR) region.[31] The position of this plasma edge depends on the n_e. The higher the n_e is, the lower the wavelength of the plasma edge is. At a free electron density of 3×10^{21} cm^{-3}, the transmittance of ITO in the visible range starts to decrease due to the low plasma edge. In addition, as shown in Figure 1.2, the transmittance of ITO exhibits an uneven value in the highest transparent region. This phenomenon is due to the reflection of the ITO film.

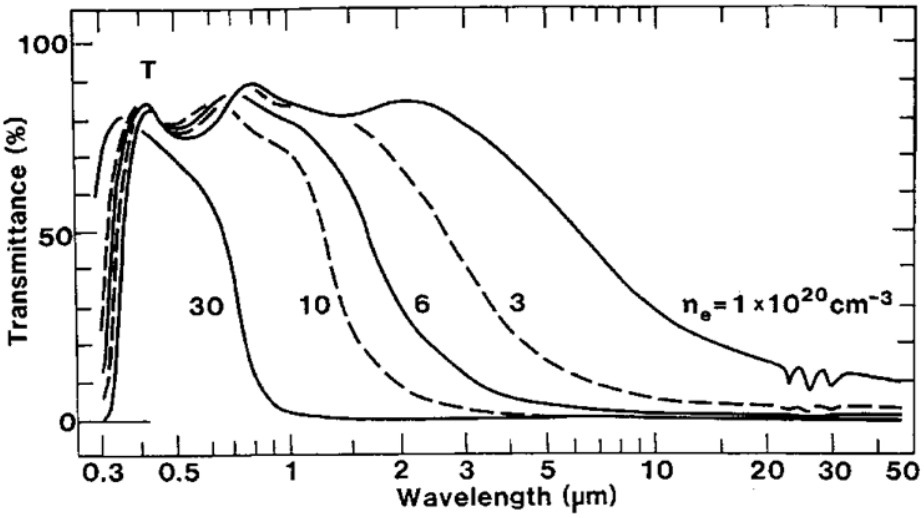

Figure 1.2 Calculated transmittance of ITO as a function of the free electron density n_e.[22]

The transparent conductive ITO thin films can be prepared using evaporation, sputtering, reactive ion plating, chemical vapor deposition, spray pyrolysis, etc.[33] Sputter coating is one of the most extensively used techniques for the ITO deposition. The ITO can be sputtered from metallic targets or oxide targets (In_2O_3 and SnO_2). The sputtering from oxide targets renders a far better control over the stoichiometry, and it has been used most frequently in industry.[33, 34] Using these methods, ITO thin films with high transparency (over 80%) and high conductivity (over 10^3 S/cm) can be prepared.[33]

Although sputtering can render high quality films, these methods result in poor target utilization and possible health hazards. Due to the naturally multidirectional deposition method, a majority of the ITO is wasted during the sputter coating. According to the United States Geological Survey, only about 15% of the ITO is made into ITO thin films, and the rest (85%) becomes waste.[35, 36] Furthermore, the preparation of the ITO targets usually involve wet surface grinding, which potentially results in severe health hazards for the workers.[37, 38] In order to address these issues with the sputtering methods, researchers began to study other methods to deposit the colloidal ITO particles onto substrates.[39, 40]

1.2. Colloidal Suspensions

1.2.1. Surface Charges and Electrostatic Potentials

The assembly of inorganic nanoparticles is usually performed using nanoparticle colloidal suspensions. Many methods of preparing colloidal suspensions will yield particles that possess surface charges. These surface charges can be generated by ionization of surface groups, adsorption of ions, dissolution of ionic solids, or substitution of ions.[41] As shown in Figure 1.3, the colloidal surface charges are balanced by an excess of ions containing opposite charges that surround the particles. These counter ions form electrical double layers, including one layer of charges firmly attached to the nanoparticle surface, the stern layer, and a diffuse layer of charges.

As a result of the surface charge, the particle surface acquires a surface electrostatic potential. This surface potential decays exponentially following the Debye-Hückel equation:[41]

$$\psi(x) = \psi_s \exp(-\kappa x) \qquad (1.1)$$

In this equation, the $\psi(x)$ and ψ_s represent the electrostatic potential at a distance x from the particle surface and the electrostatic potential at the particle surface, respectively. The constant κ has a dimension of reciprocal length, and $1/\kappa$, the distance at which the electrostatic potential falls to 37% of the surface potential, is referred as the Debye length. Usually, one times the Debye length can give a measure of the thickness of the electrical double layer, two times the Debye length gives an approximate measure of the electric field that extends from the surface, and four times the Debye length gives an indication of the distance between two adjacent particles at which the electrostatic interaction can begin.[42] The Debye length is significantly dependent on the ionic strength of a colloidal suspension. For an aqueous colloidal suspension that contains only NaCl, the Debye length at the NaCl concentration of 100, 10, 1, and 0.1 mM is 1, 3, 10, and 30 nm, respectively.[41]

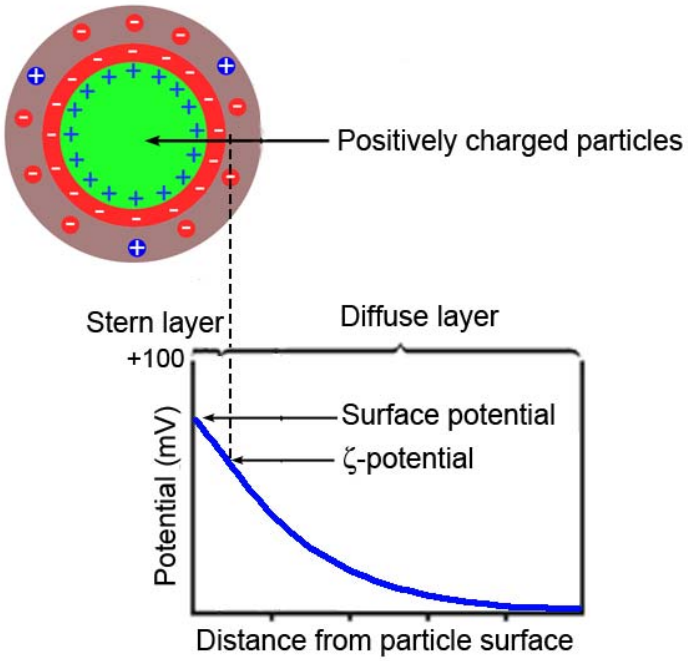

Figure 1.3 Illustration of the distribution of ions and the electrostatic potential profile around a positively charged particle.(The figure has been modified from the reference.)[43, 44]

As shown in Figure 1.3, the plane of shear is a plane within the diffuse layer that is very close to the stern layer, under which plane the counter ions can move together with the nanoparticles in the suspensions. The electric potential at this plane of shear is called the ζ-potential. ζ-potential can be measured easily using electrophoresis methods, and its value is often used to characterize the surface charge of colloidal particles. By measuring the electrophoretic mobility, *u*, of a spherical colloid particle, one can obtain the ζ-potential by using equation (1.2) or (1.3):[45]

$$u = \frac{2\varepsilon_r \varepsilon_0 \zeta}{3\eta} \quad for\ \kappa R << 1 \qquad (1.2)$$

$$u = \frac{\varepsilon_r \varepsilon_0 \zeta}{\eta} \quad for\ \kappa R > 100 \qquad (1.3)$$

in which, η is the viscosity of the solvent, the ε_0 is the permittivity of vacuum, the ε_r is the relative permittivity of the solvent, and the *R* is the radius of the colloidal particles.

The approximation of ζ-potential from electrophoretic mobility using equation (1.3) is referred to as Smoluchowski approximation.[45]

1.2.2. Mechanism for Colloidal Suspensions Stabilization

In order to perform assembly of nanoparticles, one has to prepare a stable colloidal suspension. There are generally several types of stabilization methods: electrostatic stabilization, steric stabilization, and electrosteric stabilization. As shown in Figure 1.4, when two particles approach each other, the ionic atmosphere on each particle overlaps and the local ion concentration between the particles will increase. The difference between this mid-point ion concentration and that in the bulk can result in an osmotic pressure acting to force the particles apart and thus stabilize the colloidal suspension.[41] The colloidal suspension stabilization due to this electrostatic repulsive force is called electrostatic stabilization. The electrostatic repulsive force can be evaluated by measuring the ζ-potential of the colloidal suspension. Generally, a colloidal suspension with high ζ-potential (i.e., either above +30 mV or below -30 mV) can be considered as a stable suspension.[46]

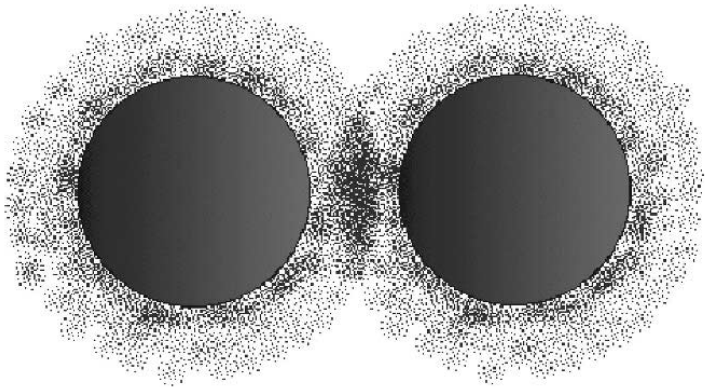

Figure 1.4 Illustration of the overlap of electrical double layers in adjacent particles.[41]

The colloidal suspension can also be stabilized by modifying the colloidal particle with polymers. As shown in Figure 1.5, when the polymer-modified particles approach each other, the polymer chains between the particles will start to overlap, and the polymer

concentration will start to increase. The local increase of the polymer concentration and the overlap of polymer chains results in a free energy penalty, and thus give rise to the steric repulsion.[41] This colloidal suspension stabilization due to the steric repulsive forces is called steric stabilization. In addition, it is also possible to have combinations of electrostatic and steric stabilization, which is termed electrosteric stabilization.

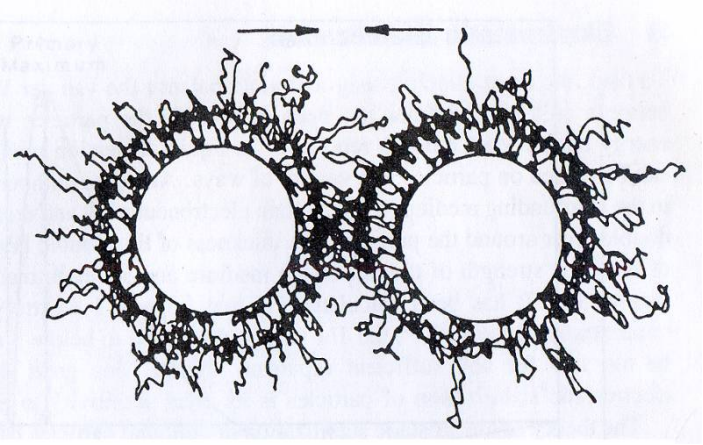

Figure 1.5 Illustration of the overlap of surface polymer chains between adjacent particles during steric stabilization.[47]

1.2.3. Stabilization of Colloidal Suspensions using Polyelectrolytes

Polyelectrolytes have long been used to stabilize colloidal suspensions through the electrosteric stabilization mechanism. Due to the surface charge of polyelectrolyte chains, the polyelectrolyte chains can adsorb onto oxide surfaces through electrostatic forces. For example, negatively charged PAA can adsorb onto the positively charged TiO_2 [48] and Al_2O_3[49] particle surfaces at relative low pH, and positively charged PEI can adsorb onto negatively charged Si_3N_4,[50] TiO_2,[51] SiO_2,[52] and ZrO_2[53, 54] particle surfaces at relatively high pH. The adsorption of positively charged PEI chains on colloidal particles can be followed by measuring their ζ-potential. As shown in Figure 1.6, after the adsorption of positively charged PEI, the ζ-potential of the Si_3N_4 particles increased to a higher positive value or reversed from negative value.

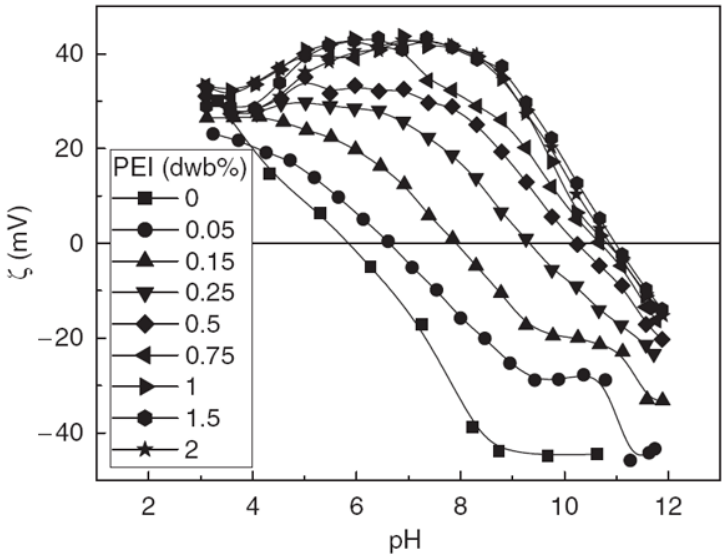

Figure 1.6 ζ-potential versus pH for 5 vol% Si_3N_4 suspension with various amounts of PEI.[50]

The adsorption of polyelectrolytes on solid particle surfaces will induce variations in the electron distribution of polymer functional groups and the polymer chain conformations. These variations can be investigated using Fourier Transform Infrared Spectroscopy (FTIR) and Surface Enhanced Raman Spectroscopy (SERS). For example, PEI will adsorb onto ZrO_2 nanoparticle surfaces due to the coordinate covalent bond between nitrogen (Lewis base) in PEI and Zr (Lewis acid).[54] The oxygen present in ZrO_2 is believed to not be involved in this interaction between PEI and ZrO_2. Under FTIR, two new peaks have been observed between 1580-1560 cm^{-1} and 1450-1350 cm^{-1} due to interaction between PEI and ZrO_2 can be observed.[54] Similar phenomena have also been observed when PEI is adsorbed onto Ag particles.[55] The ratio of symmetric CH_2 stretching over asymmetric CH_2 stretching decreases when PEI is adsorbed onto silver particles, which is due to the increase of trans-conformers in the aliphatic chain, in relation to the gauche ones of the PEI chain. A relative intensity decrease is observed for the bands corresponding to the aliphatic moieties, while a relative intensification is observed for the bands assigned to amino moieties.[55]

1.3. Layer-by-Layer (LbL) Assembly

In the past two decades, the fundamentals of the LbL assembly of polyelectrolytes have been extensively studied and well understood, while LbL assembly of polyelectrolytes and inorganic nanoparticles still needs more detailed studies.[17] Therefore, it is useful for us to revisit the fundamentals of LbL assembly of polyelectrolytes to understand the LbL assembly of polyelectrolytes and inorganic nanoparticles.

1.3.1. Polyelectrolytes Commonly Used in LbL Assembly

The structures of some conventional polyelectrolytes that were used for LbL assembly are shown in Figure 1.7. As shown in the figure, poly(diallyldimethylammonium hydrochloride) (PDDA), polyethyleneimine (PEI), and poly(allylamine hydrochloride) (PAH) are polycations, and they can gain positive charges through the amine groups. Poly(sodium 4-styrenesulfonate) (PSS) and poly(acrylic acid) (PAA) are polyanions, and they can gain negative charges through the sulfonic and carboxylic groups. PDDA and PSS are strong polyelectrolytes, which mean their degrees of ionization are not strongly affected by the pH of the solutions.[56] On the other hand, PAA, PAH and PEI are weak polyelectrolytes, and their degrees of ionization are significantly affected by the pH of the solutions.[57, 58] Figure 1.8 depicts the degrees of ionization of PAA, PAH, and PEI at the pH range of 2 to 12. As shown in the figure, the ionization degree of PAA is close to zero at a low pH, such as a pH of 2, but it increases with increasing pH of the PAA solution. On the other hand, the ionization degrees of PAH and PEI are at zero at a high pH, such as a pH of 12, and they increase with the decrease of pH.

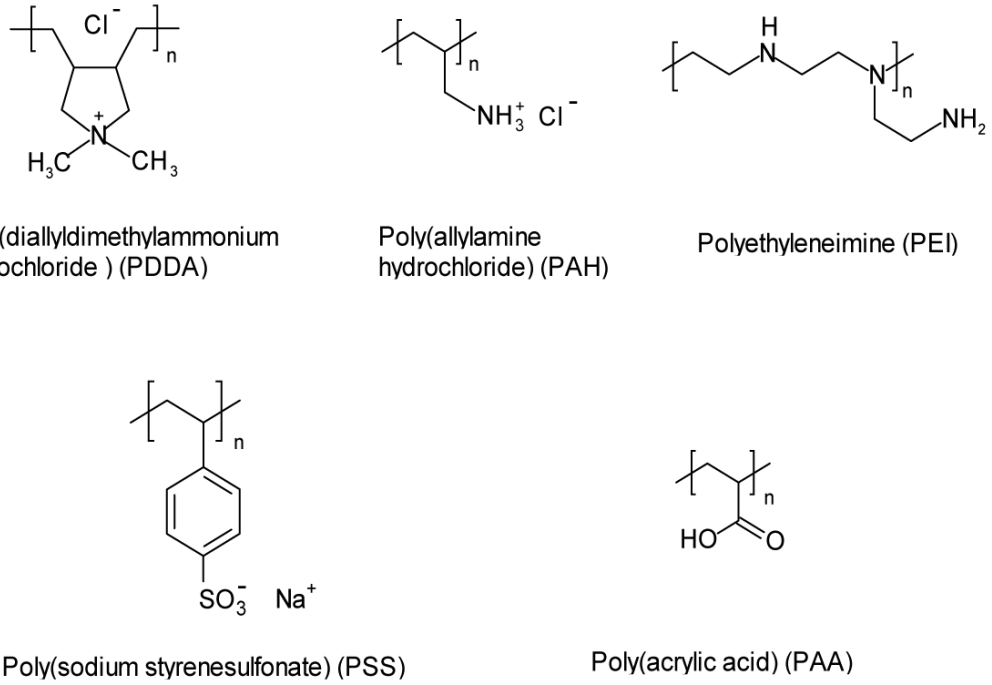

Figure 1.7 Illustration of the structure of polyelectrolytes often used for LbL assembly.

The relation between the pH of the polyelectrolyte solution and the ionization of the polyelectrolyte (α) can be described by the Henderson-Hasselbalch equation:[59-61]

$$pH = pK_a - \log\frac{1-\alpha}{\alpha} \qquad (1.4)$$

According to equation (1.4), when half of the functional groups is ionized (α equals to 0.5), the pH of the polyelectrolyte solution is defined as the pK_a of this solution. As shown in Figure 1.8(a) and (b), Choi et al. have summarized different study of the ionization of the PAA and PAH, and they have found that the pK_a of PAA and PAH is around 6.5 and 9, respectively.[57] The pK_a of polyelectrolyte solution is dependent on the ionic strength of the solution.[58] As shown in Figure 1.8(c), the pK_a of PEI without KCl and with 0.1M KCl is around 7 and 8, respectively. In other words, the ionization of the PEI chains can be increased increasing the ionic strength of the solution. It is worth

noting that the ionization curves for PAA and PAH shown in Figure 2.2 were obtained at an NaCl concentration of 0.01 M.[57]

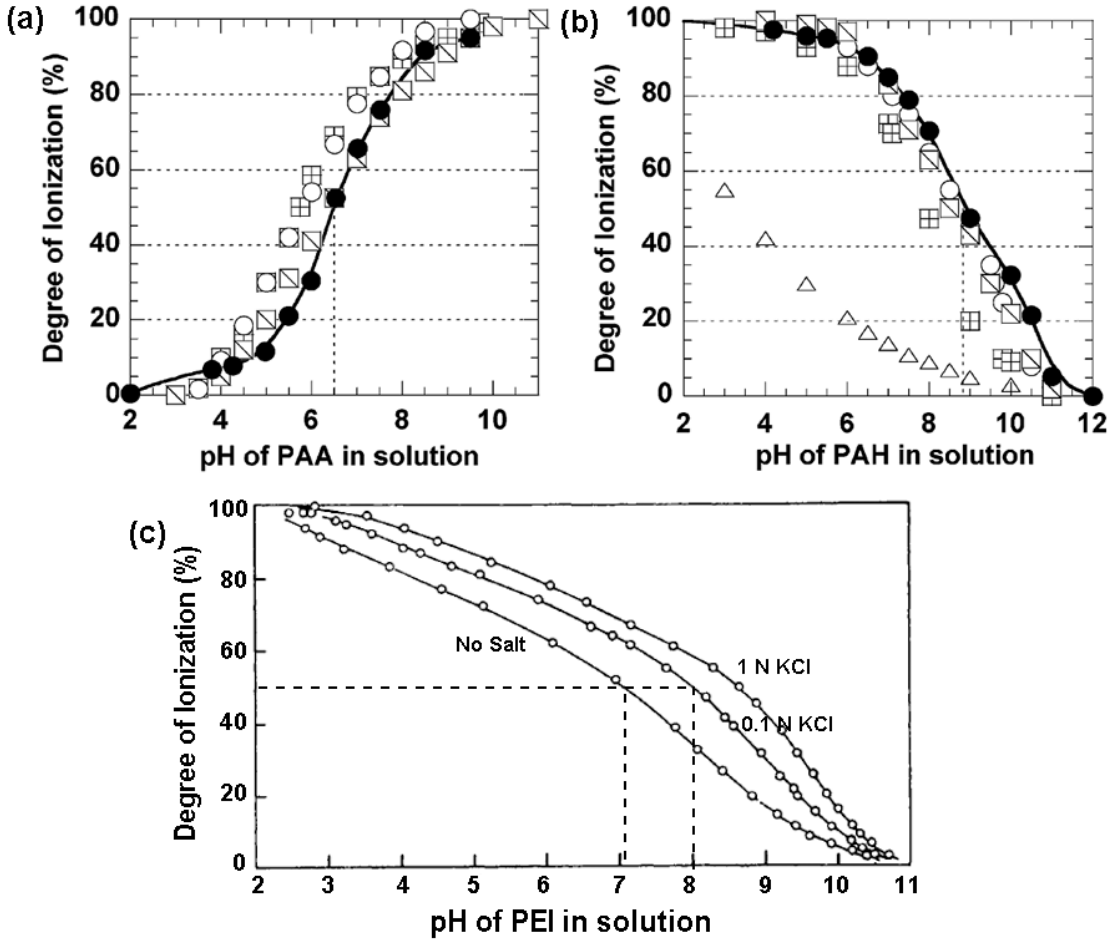

Figure 1.8 Degree of ionization of two weak polyelectrolytes depending on the pH of the polyelectrolyte solutions: (a) PAA,[57] (b) PAH,[57] and (c) PEI.[58] (The different symbols in (a) and (b) is from different studies summarized in ref [57], and all of the figures have been modified from the references.)

1.3.2. LbL Assembly of Polyelectrolytes

1.3.2.1. Fundamentals of LbL Assembly of Polyelectrolytes

The LbL assembly of polyelectrolytes was first demonstrated by Decher in 1990s.[2] As shown in Figure 1.9, the LbL assembly process can be conducted using the very simple dip-coating procedure. Two oppositely charged polyelectrolytes, the

polyanion and the polycation, can be deposited onto the substrate “layer by layer” in a cyclic manner.

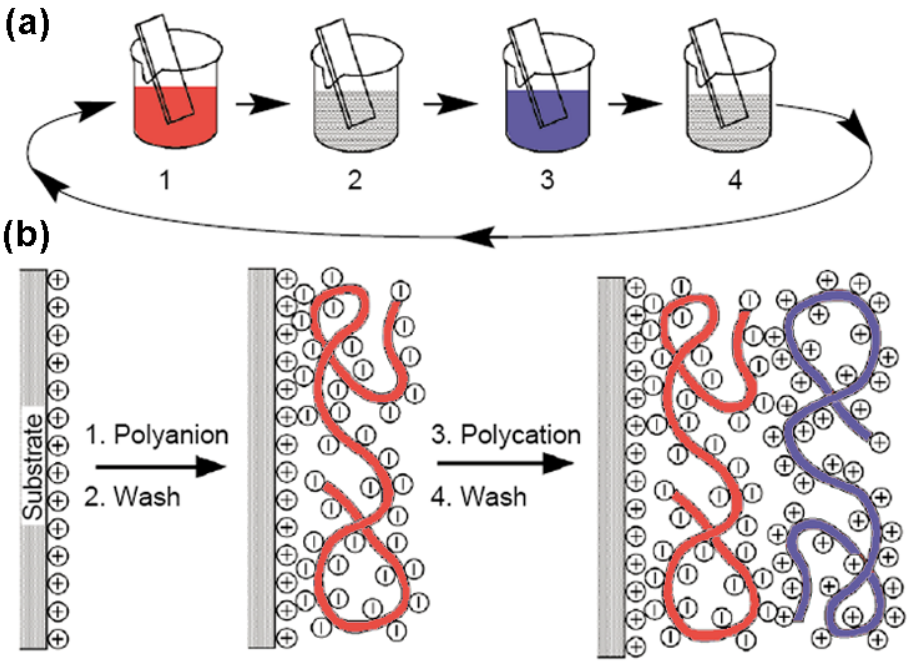

Figure 1.9 (a) Schematics of the dip coating procedure of the LbL assembly of polyanions and polycations, and (b) Simplified surface structure of one bilayer of polyanions and polycations. (The figure has been modified from the reference.)[2]

The LbL assembly of two oppositely charged polyelectrolytes is essentially a complexation process between the positive and negative polyelectrolyte segments and the release of the counterions (Figure 1.10).

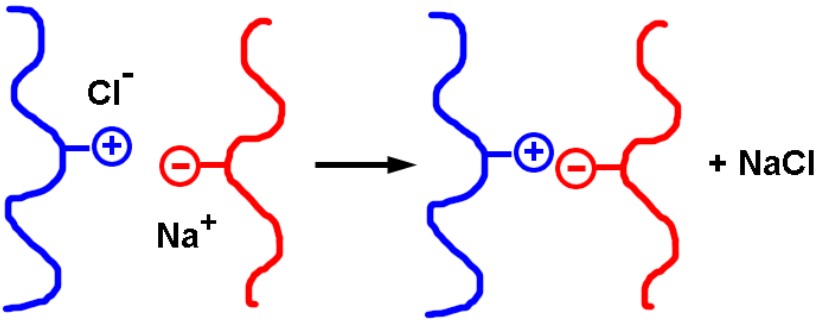

Figure 1.10 Complexation between positive polyelectrolyte and negative polyelectrolyte segments. (The figure has been modified from the reference.)[62]

During LbL assembly, the two adjacent oppositely charged polyelectrolyte layers do not form a 1:1 stoichiometric complex. Instead, as shown in Figure 1.11, only part of the electrical charges in a polyelectrolyte layer can be compensated by the subsequent oppositely charged polyelectrolyte layers. Therefore, one of the most important characteristics of the LbL assembly process is the overcompensation of the surface charges.

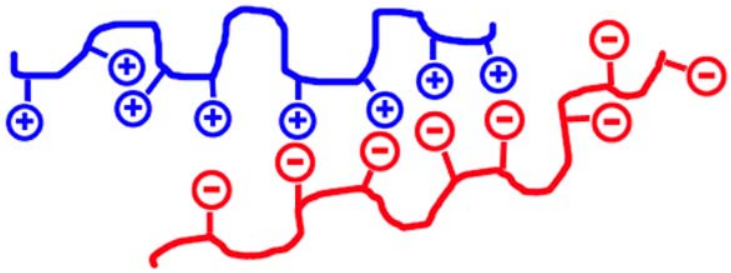

Figure 1.11 Illustration of the charge compensation between two adjacent oppositely charged polyelectrolyte layers.

The charge overcompensation has been observed in many LbL studies.[63-68] As shown in Figure 1.12, due to the charge overcompensation, the surface ζ-potential during the LbL assembly of PEI[PSS/PAH]$_5$ is seen to change sign after every assembly steps. In other words, the surface possesses excess surface charges after each assembly step.

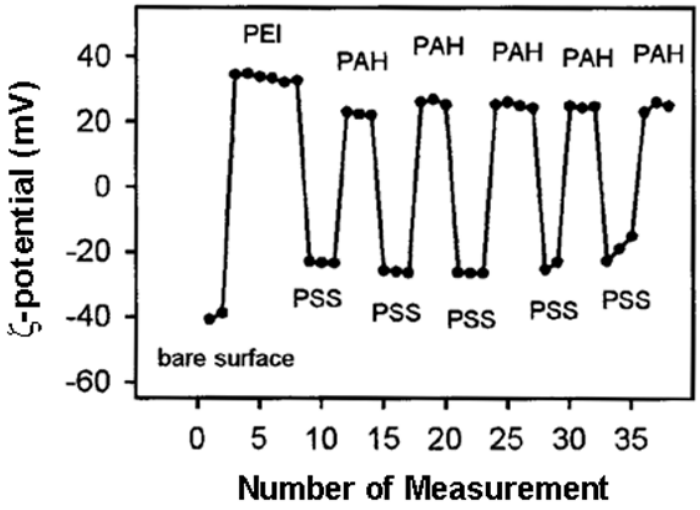

Figure 1.12 Surface ζ-potential measurements during the LbL assembly of $PEI[PSS/PAH]_5$. (The figure has been modified from the reference.)[65]

1.3.2.2. Ionic Strength Effect

The adsorption of polyelectrolyte on a substrate surface forms a typical loop-train structure (Figure 1.13).[69] The conformation of the adsorbed polyelectrolyte chains is controlled by the screening between polymer charges.[70, 71] The addition of salt, which will enhance the screening, decreases the interaction between the polymer and the surface, as well as the interaction between polymer segments, and thus permits more loop formation.[70, 71] As shown in Figure 1.13(a), at a low ionic strength, the polyelectrolyte chains extend due to the strong repelling forces between the polyelectrolyte charges. However, at a high ionic strength, the polyelectrolyte chains can form larger loop structures during the LbL assembly (Figure 1.13(b)). Therefore, each bilayer of the LbL assembled thin films will be thicker when the thin film is assembled at a high ionic strength. Moreover, at an extremely high ionic strength, the salt screening effect can promote the desorption of the polyelectrolyte chains.[71-73]

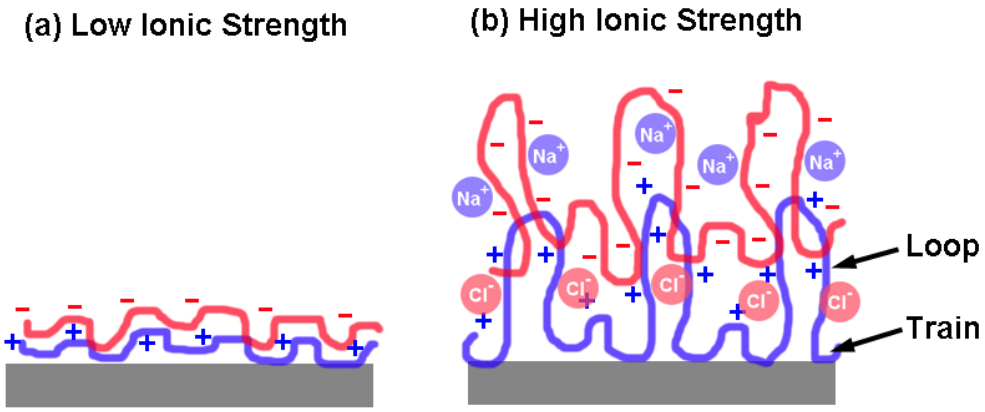

Figure 1.13 Illustration of the ionic strength effect on the conformation of adsorbed polyelectrolyte chains during the LbL assembly.

The effect of ionic strength on the LbL assembly of polyelectrolyte multilayers (PEMs) has been observed by many researchers.[16, 73-80] As shown in Figure 1.14, during the LbL assembly of poly(N-methyl-2-vinyl pyridinium chloride) (PM2VP) and PSS, the UV light absorbance of films, which is proportional to the film buildup rate, from polyelectrolyte solutions at the NaCl concentration of 0.1 M is significantly higher than that when no NaCl was added into the polyelectrolyte solution.[75] On the other hand, as shown in Figure 1.15, during the LbL assembly of poly(l-Lysine) (PLL) and poly(guanylic acid) (Poly[G]), increasing NaCl concentration below 0.5 M increases the film buildup rate, whereas increasing NaCl concentration above 0.5 M decreases the film buildup rate due to the strong salt screening.[73]

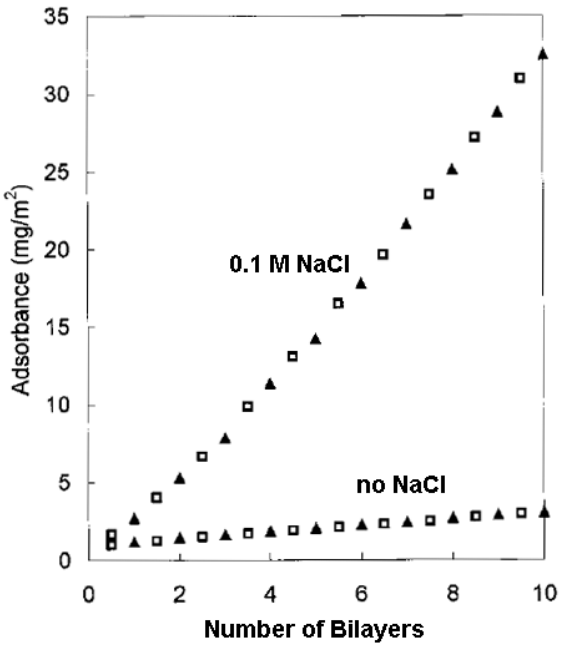

Figure 1.14 Buildup of the $[PM2VP/PSS]_n$ thin film from a solution containing 0.1 M NaCl or no NaCl. (The figure has been modified from the reference.)[75]

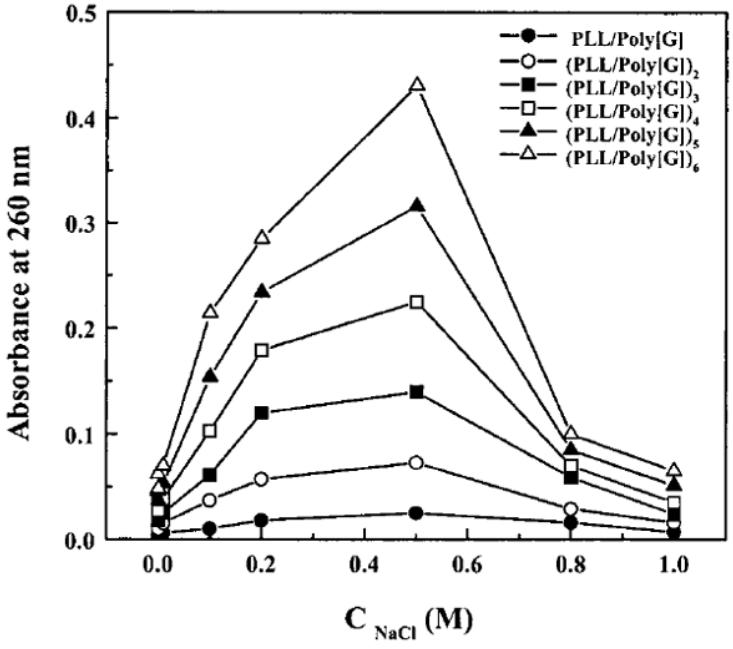

Figure 1.15 The effect of NaCl concentration on the LbL assembly of $[PLL/Poly[G]]_n$ films.[73]

1.3.2.3. pH Effect

The LbL assembly of polyelectrolyte multilayers (PEMs) can also be significantly affected by the pH of the polyelectrolyte solutions.[57, 74, 76, 81, 82] The pH effect on the buildup of the PEMs is primarily due to its influence on the electrical charges of weak polyelectrolytes, such as PEI, PAH, and PAA. If the polyelectrolytes are highly charged, the polymer chains will be extended due to the strong repelling forces between the charges. In this case, the conformation of chains that adsorbed on the substrates will be composed of mostly trains, and the multilayer thickness will be relatively thin (Figure 1.16(a)). On the contrary, if the polyelectrolytes have a low charge, the polymer chains will form a coil structure. In this case, the conformation of deposited polymer chains will possess primarily loops, and the multilayer layer will be much thicker than when the polymer chains conformation are mainly trains (Figure 1.16(b)).

As shown in Figure 1.17, the bilayer thickness that is contributed by one bilayer of $[PAH/PAA]_n$ PEMs is significantly affected by the pH of the PAH and the PAA solutions.[81] When the PEMs were assembled from both highly charged PAH (at low pH) and highly charged PAA (at high pH), the thickness of PEMs was at minimum. However, when the PEMs were assembled from both low charged PAH (at high pH) and low charged PAA (at low pH), the PEMs thickness was at a value of more than 120 Å nm per bilayer. When only one of the polyelectrolytes was low charged, the bilayer thickness was around 40 to 100 Å per bilayer.

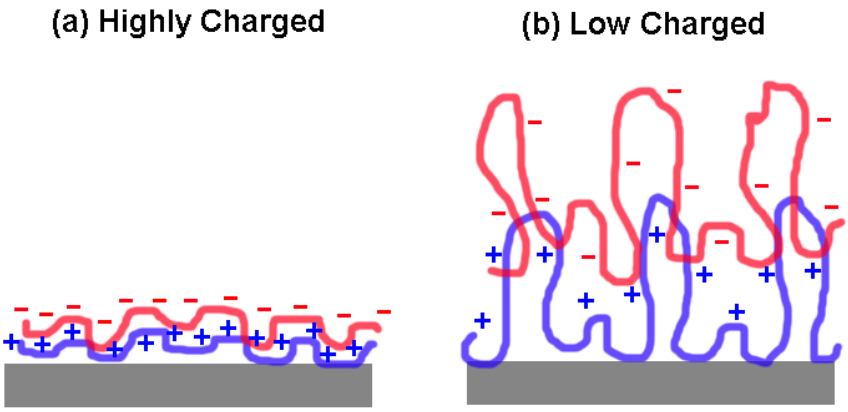

Figure 1.16 Illustration of the effect of electrical charge density of polyelectrolyte chains on the buildup of the polyelectrolyte multilayers (PEMs) from weak polyelectrolytes.

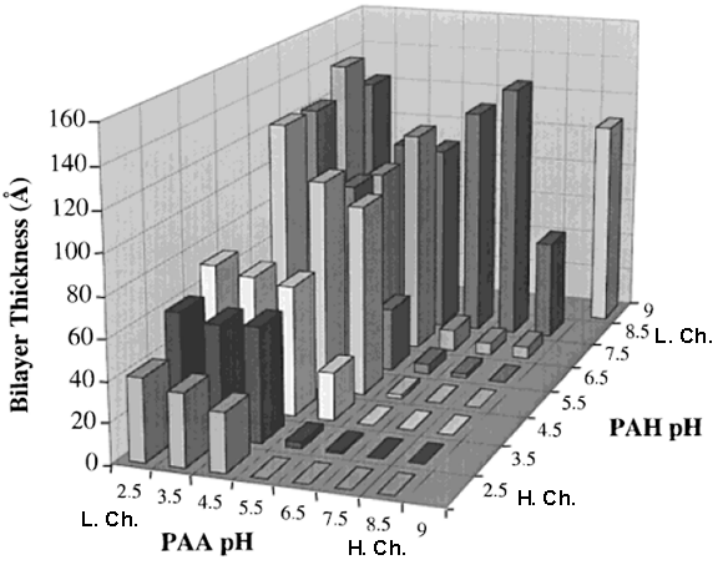

Figure 1.17 The average bilayers thickness of $[PAH/PAA]_n$ PEMs as a function of the pH of the PAH and PAA solutions. In the figure, the "H. Ch." and "L. Ch." stand for the "highly charged" and "low charged", respectively. (The figure has been modified from the reference.)[81]

Figure 1.18 depicts the average bilayer thickness of different combinations of counterions as a function of the pH of the polyelectrolyte solutions.[57] In this figure, at least one of the counterions is a weak polyelectrolyte: either PAA for polyanions or PAH for polycations. Poly(vinylsulfonic acid) (PVS), PSS, PDDA, and poly(4-vinylbenzyltrimethylammonium chloride) (PVTAC) are strong polyelectrolytes.

As shown in the figure, the average bilayer thickness of all thin films when they were assembled at the pH around 7 was at a minimum (around 5 Å), due to the high charge density of both the strong and weak polyelectrolytes at this pH. For the thin films assembled at low pH, the average bilayer thickness was at minimum (around 5 Å) when PSS or PVS was used as the polyanions, whereas the average bilayer thickness was between 70 and 160 Å when PAA was used at polyanions. On the other hand, for the thin films assembled at high pH, the average bilayer thickness was at minimum (around 5 Å) when PDDA or PVTAC were used as the polycation, whereas the average bilayer thickness was between 40 and 100 Å when PAH was used as the polycation.

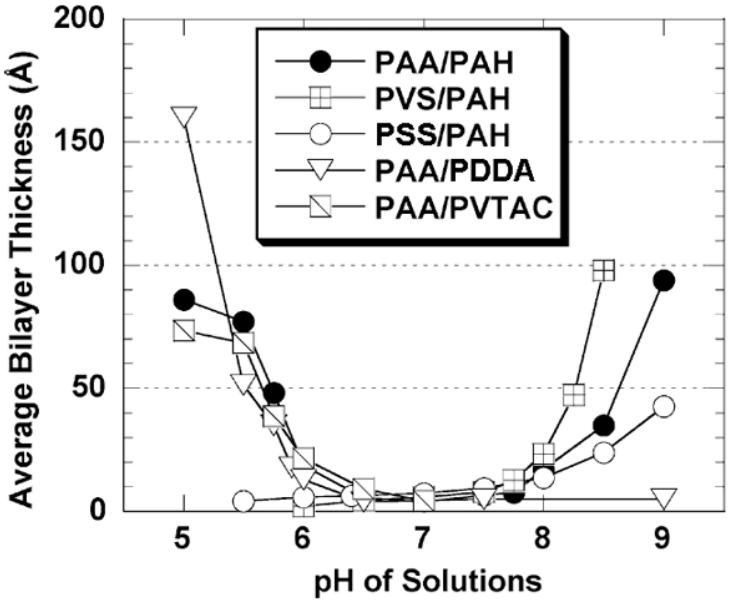

Figure 1.18 The average bilayer thickness as a function of the pH of the polyelectrolyte solutions of thin films $[PAA/PAH]_n$, $[PVS/PAH]_n$, $[PSS/PAH]_n$, $[PAA/PDDA]_n$, and $[PAA/PVTAC]_n$.(The figure has been modified from the reference.)[57]

1.3.3. LbL assembly of Polyelectrolyte and Inorganic Nanoparticles

1.3.3.1. Fundamentals of LbL assembly of polyelectrolytes and inorganic nanoparticles

The mechanism for the LbL assembly of polyelectrolytes and inorganic nanoparticles can be divided into two steps: the assembly of polyelectrolytes and the

assembly of inorganic nanoparticles. The assembly of polyelectrolytes follows a similar mechanism as discussed in the previous sections. Therefore, the main focus of this section will be on the mechanism of the assembly of inorganic nanoparticles under various conditions. As shown in Figure 1.19, the assembly of inorganic nanoparticles is controlled by two forces: the interparticle forces and the particle-surface forces.[21, 56] Generally, the interparticle forces are dominated by repulsive forces that control the stability of the colloidal suspensions. A strong repulsive interparticle force will render a patchy thin film growth, and the particles will tend to form isolated islands during the assembly.[83-85] Therefore, a weak repulsive interparticle force is favored for the assembly of inorganic particles to form a fully covered substrate surface during one step of particle assembly. On the other hand, the particle-surface interaction forces are mainly attractive forces during the LbL assembly.[21, 56] Therefore, it is easy to understand that strong particle-surface attractive forces are favorable for the LbL assembly process.

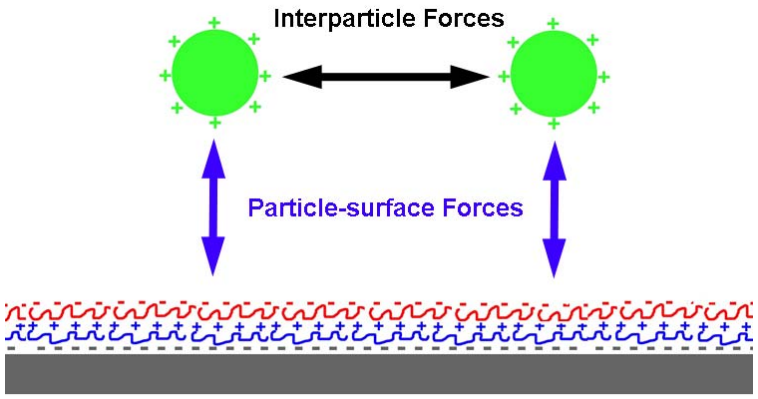

Figure 1.19 Schematics of two forces that mediate the assembly of inorganic nanoparticles: the interparticle forces and the particle-surface forces.

For a conventional electrostatic LbL assembly process, both the interparticle forces and the particle-surface forces are dominated by the electrostatic forces. As shown in Figure 1.19, for the positively charged particles, the interparticle forces are the repulsive electrostatic forces, whereas the particle-surface forces are the attractive

electrostatic forces. Both of these two types of forces are dependent on the surface charge of the nanoparticles, which can be characterized by the ζ-potential. A high ζ-potential means a strong repulsive force between particles, which is unfavorable for dense packing during the assembly of particles. At the same time, a high ζ-potential also indicates a strong attractive force between the particles and the surface, which is favorable for the adsorption of the particles. Due to this opposite dependence on the ζ-potential, the literature reports on the effect of ζ-potential on the assembly of nanoparticles has been controversial.[46, 86, 87] For example, Wang et al. found that an increase of the absolute value of the ζ-potential of a SiO_2 suspension by varying the pH and the dielectric constant of solvent will raise the average bilayer thickness.[86] However, during the assembly of bare and amine-functionalized SiO_2, Lee et al. found that the optimized assembly condition is observed at a relatively low absolute ζ-potential value (-14 to -28 mV) of bare SiO_2.[46] In addition, it has also been found that a higher assembly rate can be obtained from acid-treated carbon nanotubes at a relatively lower absolute ζ-potential value.[87]

1.3.3.2. Surface Modification of Nanoparticles

Nanoparticles used for LbL assembly are often modified by an organic layer on the surface.[83, 88-93] The function of this organic layer is considered to be two-fold: (1) to protect the nanoparticles from agglomeration and aggregation due to the steric stabilization, and (2) to mediate the interparticle and the particle-surface interaction forces.[21, 56]

As shown in Figure 1.20, the LbL assembly of PDDA and bare yttrium iron garnet (YIG) nanoparticles exhibited a patchy growth process.[83] The YIG nanoparticles formed isolated islands on the substrate, and these islands were seen to grow at later stages of the LbL assembly process. One bilayer of $[PDDA/YIG]_n$ cannot fully cover the substrate surface. On the other hand, when the YIG nanoparticles were modified with a positively

charged organic layer of 3-aminopropyl trimethoxysilane, the modified YIG particles formed a dense layer in one assembly bilayer (Figure 1.20(c)). This sharp transition was attributed to the introduction of the secondary hydrophobic attractive forces to the primary electrostatic interparticle and particle-surface forces.[83]

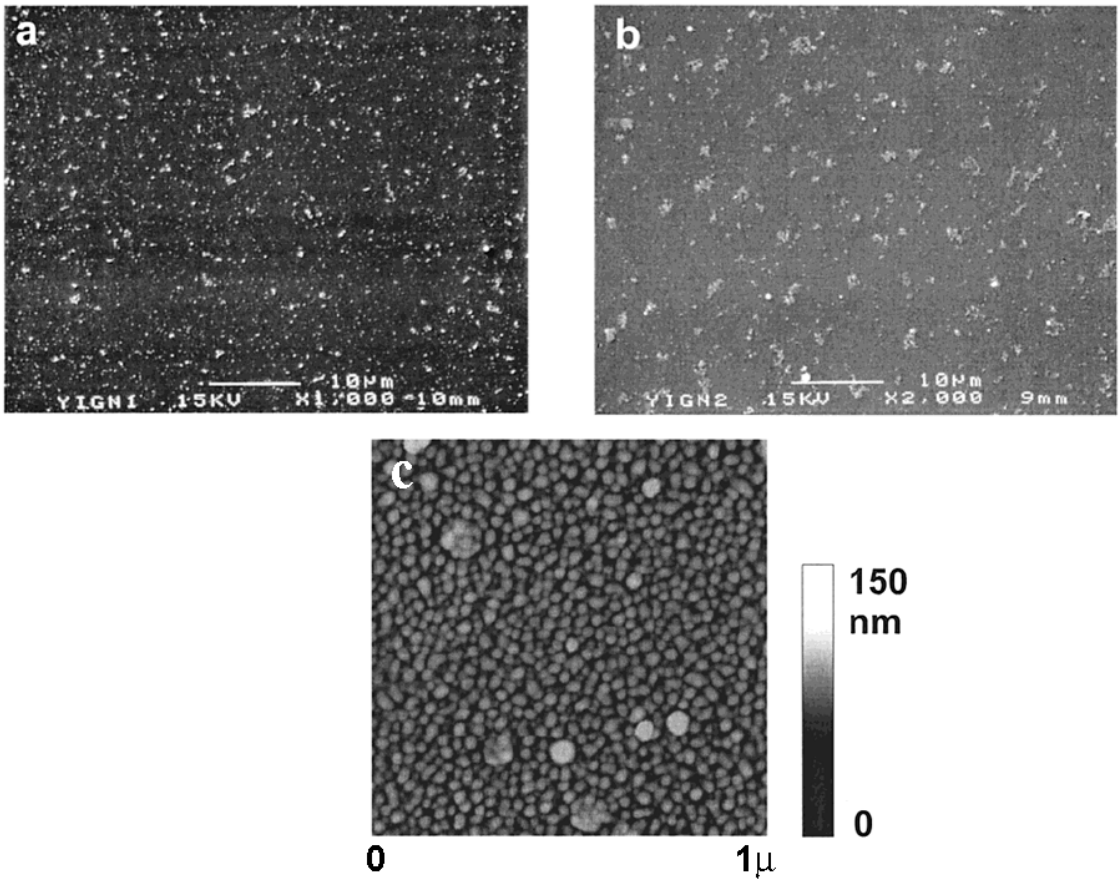

Figure 1.20 SEM images of $[PDDA/YIG]_n$ films with (a) $n = 1$, and (b) $n = 2$, and AFM images of $[PAA/modified\ YIG]_1$ film on a PDDA/PAA/PDDA precursor layer. (The figures have been modified from the reference.)[83]

The interparticle and the particle-surface interaction forces were also mediated by introducing two different surface modifying agents. Kotov et al. have shown that by introducing a mixture of ethyl mercaptan, EtSH, and thiolactic acid, $CH_3CH(SH)COOH$, on the CdS nanoparticles, they were able to manipulate the two kinds of interaction forces. The ethyl mercaptan modified surface exhibited a hydrophobic nature, while the thiolactic acid modified surface exhibited a hydrophilic surface. Therefore, by varying

their ratio on the nanoparticle surface, they could modify the balance of hydrophobic interactions and the electrostatic interaction forces. As shown in Figure 1.21, the film thickness of $[PDDA/SAM\text{-}CdS]_5$ is dependent on the ratio of surface modifying agent thiolactic acid and ethyl mercaptan. At a ratio of thiolactic acid/ethyl mercaptan of around 0.3, the thickness of the thin film reached the optimal thickness.

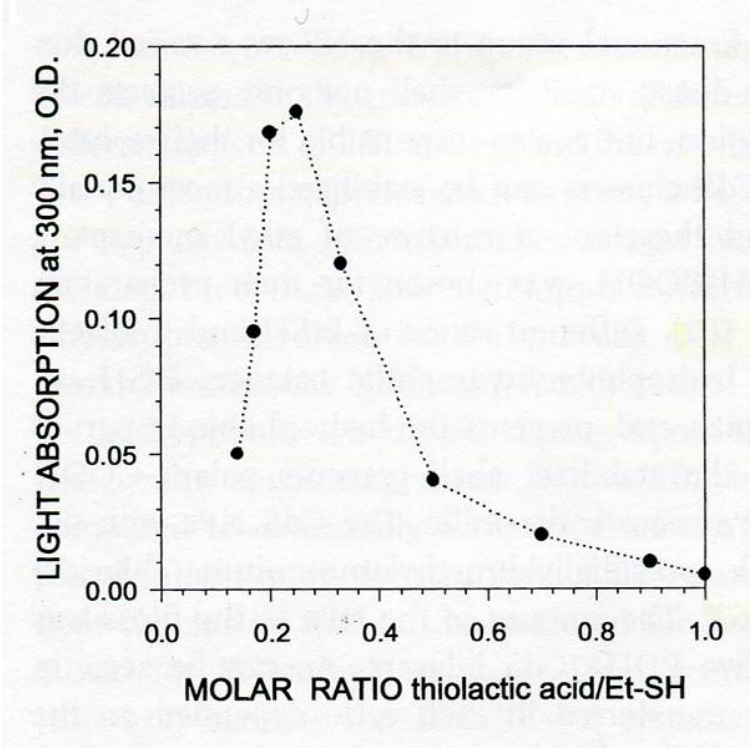

Figure 1.21 The dependence of thickness of $[PDDA/CdS]_5$ film on the ratio of thiolactic acid / ethyl mercaptan on the CdS surface.[21]

1.3.3.3. Effect of Ionic Strength and pH in the Polyelectrolyte Solutions

The ionic strength and the pH effect on the LbL assembly of polyelectrolytes and nanoparticles can be divided into two parts: the effect of the ionic strength and the pH in the polyelectrolyte solutions and the effect of the ionic strength and the pH in the nanoparticle suspensions. As discussed in the previous sections, the ionic strength and pH can affect the conformation of the adsorbed polyelectrolyte chains. A high ionic strength can render a loopy structure for the polyelectrolyte layer, and the pH can also affect the

conformation of adsorbed weak polyelectrolytes. The polyelectrolyte structure can thus affect the assembly of the subsequently deposited nanoparticles.

The effect of the ionic strength in the polyelectrolyte solutions on the LbL assembly process of polyelectrolyte/inorganic nanoparticle multilayers has been observed in several systems.[92, 94] Song et al. have observed that the LbL assembly of PAH and self-assembled monolayer (SAM)-modified gold nanoparticles was significantly affected by the ionic strength in the PAH solutions.[92] The gold nanoparticles were modified with a mixture of three SAM materials: one is hexanethiol (C_6SH), one is ferrocenylhexanethiol (FcC_6SH), and the other one is the mercaptoundecanoic acid (MUA). The buildup of thin film $[PAH/SAM\text{-}Au]_n$ can thus be followed by the electrochemical response of the ferrocene moiety attached to the Au particles. As shown in Figure 1.22(a), the total charge of the thin films, which is linearly proportional to the film thickness, is significantly affected by the ionic strength in the PAH solutions. According to these results, a high ionic strength would render a thick film.

Similar to the ionic strength, the pH of a weak polyelectrolyte solution could also affect the LbL assembly of polyelectrolytes and inorganic nanoparticles.[92, 95, 96] As shown in the Figure 1.22(b), the buildup rate of the thin film $[PAH/SAM\text{-}Au]_n$ increases with the pH of the PAH solution. In other words, when the thin film was assembled in a PAH solution at a high pH, the film buildup rate is higher. This phenomenon was attributed to the ionization of the carboxylic groups on the gold particle surface at high pH, which favors the assembly of Au nanoparticles on the PAH surface.[92]

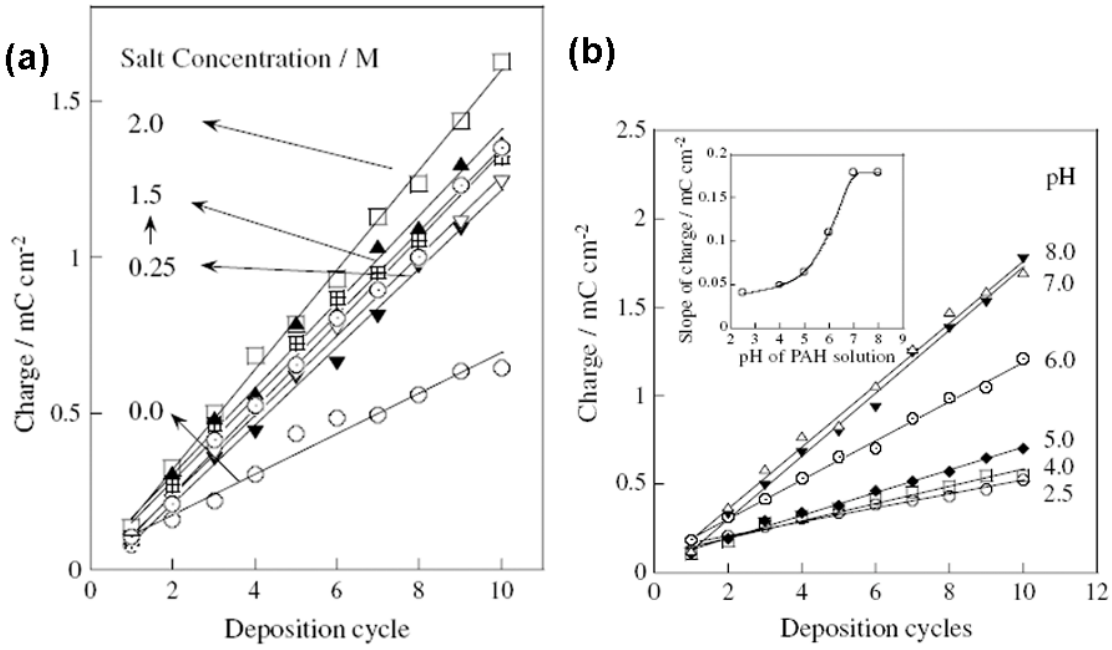

Figure 1.22 The effect of (a) the salt concentration in the PAH solution and (b) the pH of the PAH solution on the LbL assembly of $[PAH/SAM\text{-}Au]_n$ films. (The figure has been modified from the reference).[92]

1.3.3.4. Effect of Ionic Strength and pH in Nanoparticle Suspensions

The ionic strength and the pH of the nanoparticle suspensions can also significantly affect the assembly of nanoparticles by manipulating the interparticle and the particle-surface interaction forces. Generally, increasing the ionic strength of nanoparticle suspensions decreases the interparticle repulsive forces due to salt screening, and thus increases the adsorption rate of nanoparticles during LbL assembly.[21, 97-101] As shown in Figure 1.23, the buildup of $[PDDA/SiO_2]_n$ was significantly improved by increasing the concentration of NaCl in the SiO_2 suspensions.[98]

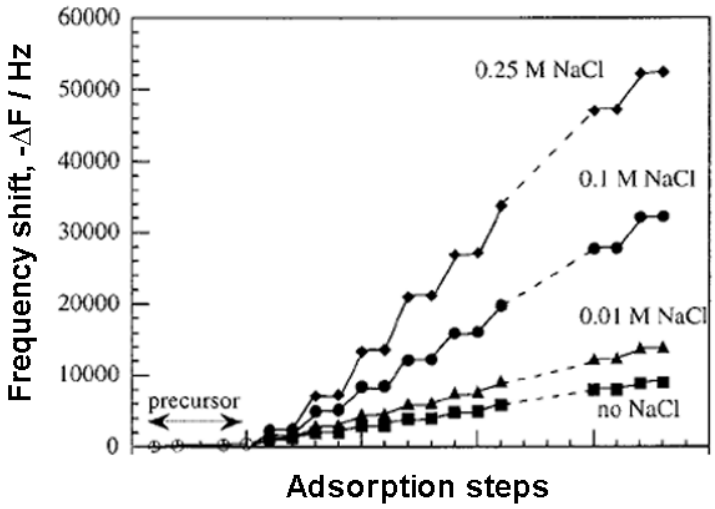

Figure 1.23 The effect of NaCl concentration in the SiO_2 suspensions on the LbL assembly of $[PDDA/SiO_2]_n$ films. (The figure has been modified from the reference.)[98]

Unlike the ionic strength, the pH of the nanoparticle suspensions has a multifaceted effect on the assembly of the nanoparticles.[21, 46, 68, 85-87, 102-104] The surface charge of nanoparticles will change with the pH of the nanoparticle suspensions. As discussed in the previous sections, the assembly of nanoparticles has been shown to provide conflicting responses to the ζ-potential, due to the different balance between the interparticle repulsive forces and the particle-surface attractive forces. As shown in Figure 1.24, both the ζ-potential of the TiO_2 and SiO_2 are dependent on the pH of the colloidal suspensions, and the average bilayer thickness of thin film $[TiO_2/SiO_2]_n$ is also significantly affected by the pH of these two suspensions.[68]

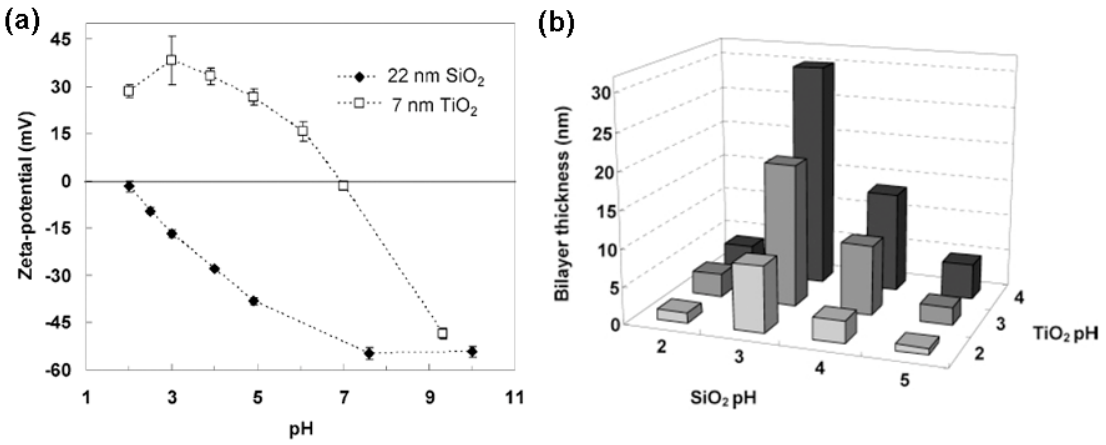

Figure 1.24 (a) The ζ-potential of TiO_2 and SiO_2 nanoparticle suspensions as a function of the suspension pH, and (b) the effect of the pH of the TiO_2 and the SiO_2 suspensions on the average bilayer thickness of thin film $[TiO_2/SiO_2]_n$. (The figure has been modified from the reference.)[68]

1.3.4. Exponentially Grown LbL Film

Up to date, two types of LbL thin films have been reported in the literature: linearly grown LbL (*l*-LbL) films and exponentially grown LbL (*e*-LbL) films. The first type of thin film, for which the thin film mass and thickness grow linearly with the number of deposition steps, is known as *l*-LbL growth. This type of thin film has been widely observed and studied, and its growth mechanism is well understood. Most of the thin films mentioned in the previous sections belong to the *l*-LbL growth category. Usually, the film buildup rate of *l*-LbL thin films is generally slow due to having the same assembly rate at every assembly step.

It was recently discovered that the thin film mass and thickness can also grow exponentially with the number of deposition steps, and this type of LbL thin film has been called "*e*-LbL film".[105, 106] Due to its exponentially growing nature, the thin film growth rate is enhanced significantly compared to *l*-LbL films. The *e*-LbL film was first reported for the polyelectrolyte multilayers (PEMs) containing biological organic materials.[105] Since then, the research on *e*-LbL thin films has experienced rapid growth. Not only have polyelectrolyte components with biological nature[105-107] been shown to

exponentially grow, but also other polyelectrolytes that have traditionally exhibited linear growth have been observed to undergo exponential growth under certain promoting conditions.[108-111] For example, as shown in Figure 1.25(a) and (b), the traditional linearly grown $[PDDA/PSS]_n$ multilayers can be transferred to *e*-LbL grown film by increasing the NaCl concentration[110] or increasing the temperature.[108] In addition, the *l*-LbL growth of $[PEI/PAA]_n$ films can also be transferred to *e*-LbL growth by assembling the PEI at high pH and the PAA at low pH.[109]

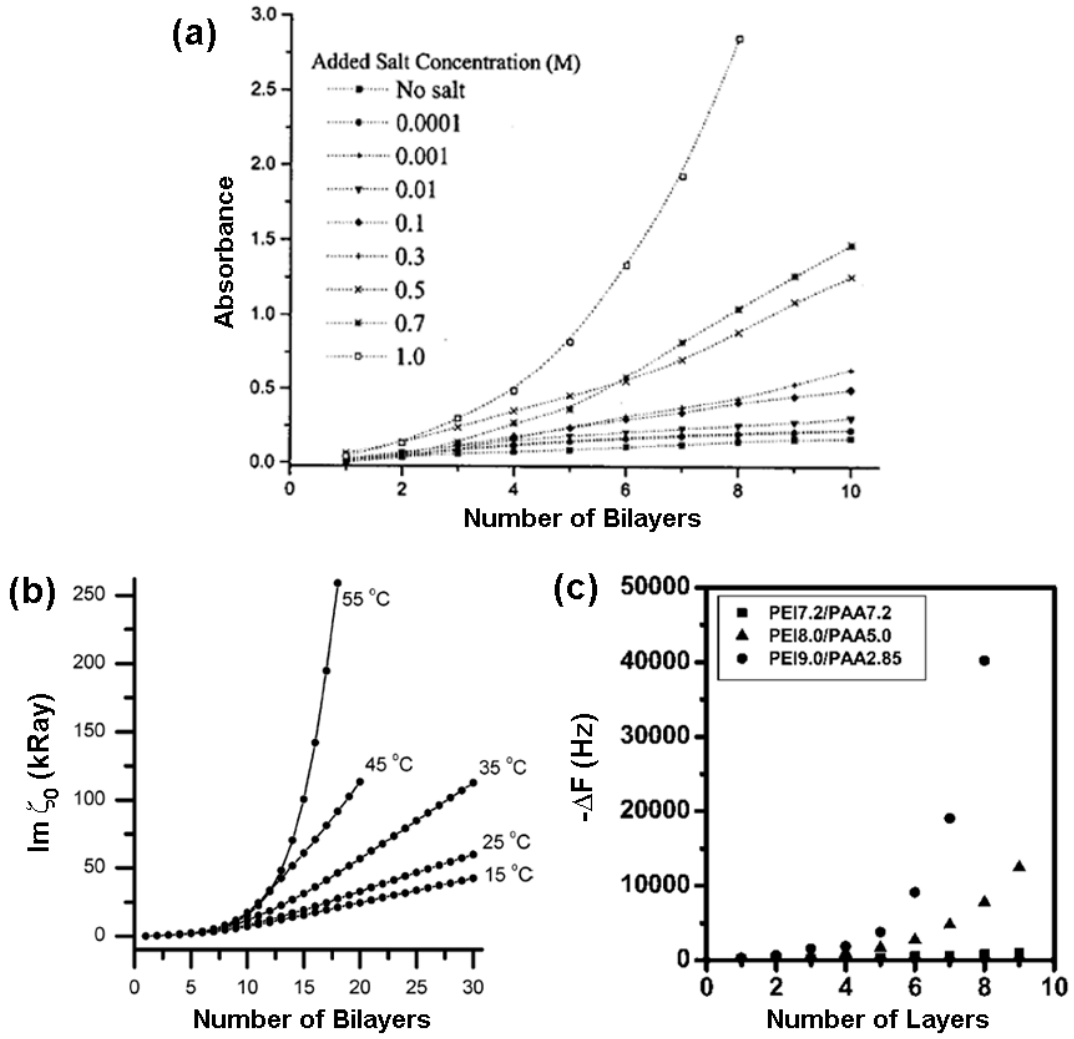

Figure 1.25 (a) Ionic-strength-amplified *e*-LbL growth of $[PDDA/PSS]_n$ films,[110] (b) temperature-amplified *e*-LbL growth of $[PDDA/PSS]_n$ films,[108] and (c) pH-amplified *e*-LbL growth of $[PEI/PAA]_n$ films. (The figure has been modified from the reference.)[109]

The mechanism of the *e*-LbL growth has been attributed to the excess number of counter-ions available on the thin film surface due to the "in-and-out" diffusion of at least one of the polyelectrolyte components.[11, 112-117] For example, as shown in Figure 1.26, during the *e*-LbL assembly of poly(l-Lysine) (PLL) and hyaluronan (HA), the polycation PLL could diffuse into the thin film during the PLL deposition step (Figure 1.26(b) and (c)) and diffuse out to the thin film surface to absorb the excess amount of HA during the HA deposition step (Figure 1.26(e) and (f)).[112]

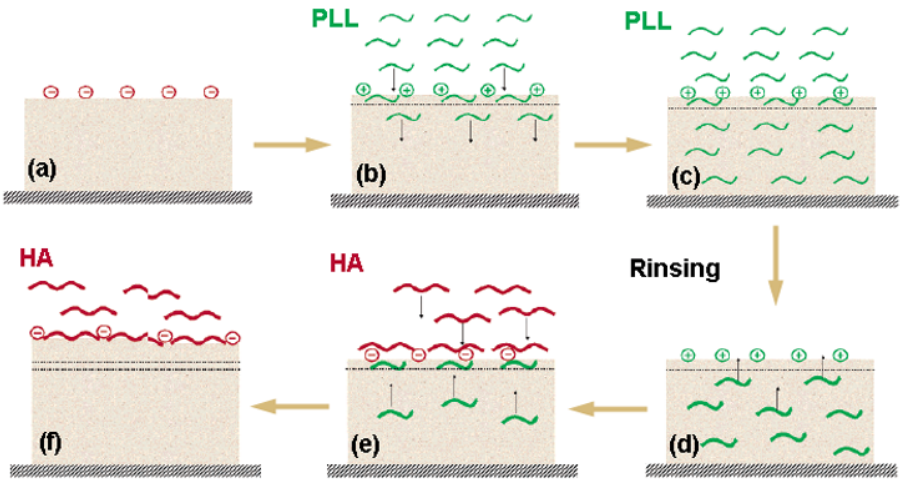

Figure 1.26 Illustration of the diffusion of PLL during the *e*-LbL assembly of the $[PLL/HA]_n$ films. (The figure has been modified from the reference.)[112]

The diffusion of polymer was demonstrated by observing the diffusion of fluorescent-labeled PLL during the *e*-LbL assembly of $[PLL/HA]_n$ using confocal laser scanning microscopy (CLSM). The PLL was labeled with fluorescein isothiocyanate (FITC), and the HA labeled with Texas red (TR). diffused through the whole film during the assembly, whereas did not diffuse. For example, during the LbL assembly of $[PLL/HA]_{19}$-PLL_{20} thin film, the 19th layer of PLL and HA was labeled with fluorescent dyes, and they were denoted with PLL_{19}-FITC and HA_{19}-TR, respectively. As shown in Figure 1.27(a), the PLL labeled with FITC was observed through the whole film after the assembly, whereas the HA labeled with TR was only observed on top of the thin films. In

other words, the PLL_{19}-FITC diffused through the whole film, but the HA_{19}-TR did not diffuse. Similarly, as shown in Figure 1.27(b), the diffusion of PLL was also observed during the LbL assembly of $[PLL/HA]_{25}$ containing PLL_{19}-FITC and HA_{19}-TR.

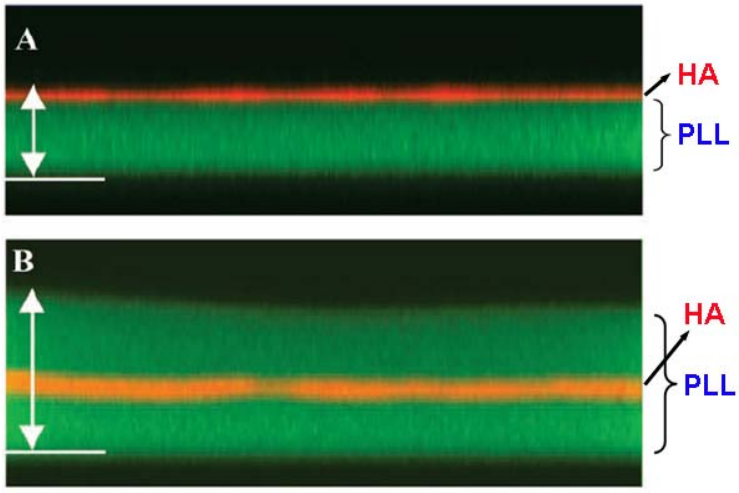

Figure 1.27 Confocal laser scanning microscopy (CLSM) image of $[PLL/HA]_n$ thin films with labeled PLL and HA layers: (a) $[PLL/HA]_{19}$-PLL_{20} containing PLL_{19}-FITC (green color) and HA_{19}-TR (red color), and (b) $[PLL/HA]_{25}$ containing PLL_{19}-FITC and HA_{19}-TR. (The figure has been modified from the reference.)[112]

Up to now, most of the *e*-LbL growth has been observed in polymeric or organic systems. It would be very promising to expand the *e*-LbL method to inorganic materials, since films grown by the LbL assembly of polyelectrolyte/inorganic nanomaterials have shown exceptional mechanical properties,[12, 116, 117] electrical properties,[63, 118] optical properties,[87, 119] as well as biological properties.[11, 105, 120] So far, there have been very few studies in the literature focusing on the *e*-LbL growth of polyelectrolyte/inorganic nanoparticle thin films. As shown in Figure 1.28(a) and (b), the *e*-LbL growth of hybrid thin films has been demonstrated by substituting every other PAA layer in $[PEI/PAA]_n$ *e*-LbL system with Na^+-montmorillonite (MTM) nanosheets to prepare the $[PEI/PAA/PEI/MTM]_n$ tricomponent composite film,[116, 121] or by assembly of PAA-$CaCO_3$ complex and PAH.[117] In both cases, the thin films were primarily composed of organic materials, instead of the inorganic materials.

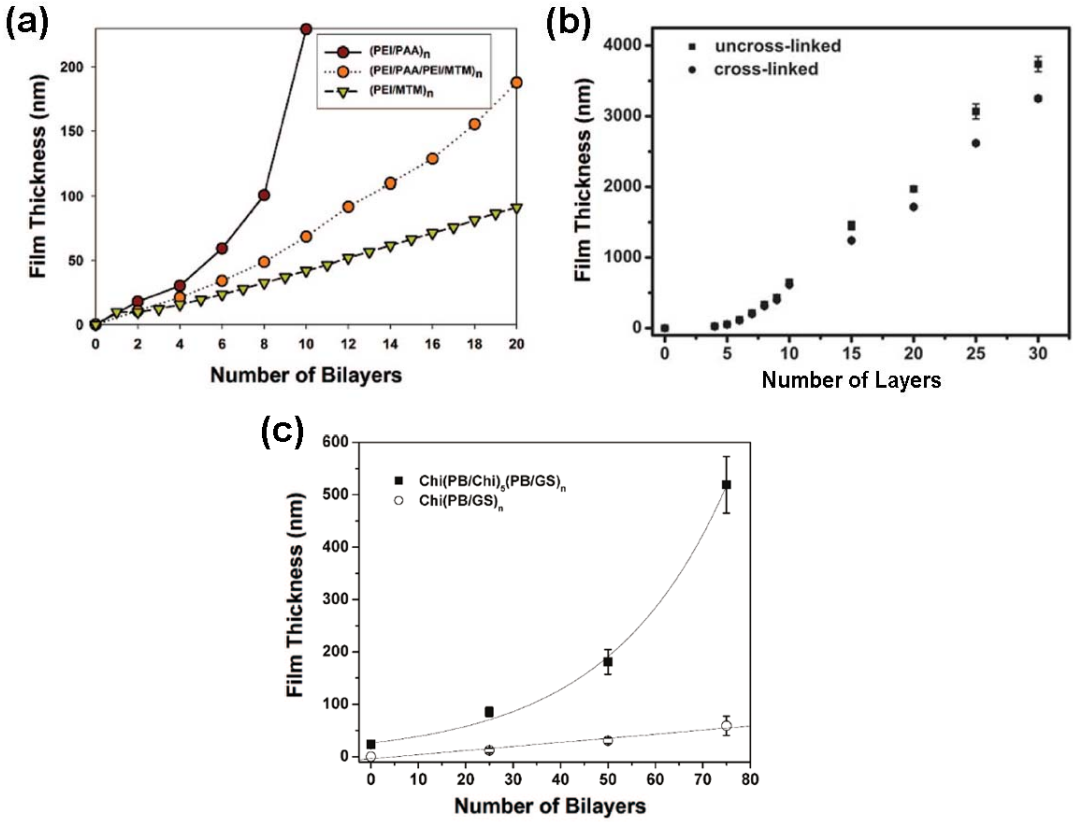

Figure 1.28 *e*-LbL growth of thin films: (a) $[PEI/PAA/PEI/MTM]_n$,[116] (b) $[PAH/PAA\text{-}CaCO_3]_n$,[117] and (c) $CHI[PB/CHI]_5[PB/GS]_n$.[11]

1.4. Motivations and Scopes of Research

It is believed that directly depositing ITO nanoparticles on substrates would increase the efficiency of ITO utilization and allow ITO coatings onto complex-shaped surfaces. LbL assembly provides an easy, versatile, and robust method for preparing hybrid thin films composed of polyelectrolytes and ITO nanoparticles. Despite the wide application of the LbL assembly method, the fundamental understanding of LbL assembly of hybrid thin films composed of polyelectrolytes and inorganic nanoparticle lags behind.[17, 21] Therefore, the main focus of this thesis is on the fundamental understanding of the LbL assembly process of polyelectrolytes and nanoparticles. The effect of pH, ionic strength, and the ζ-potential on the assembly of ITO nanoparticles will

be studied in Chapter 3 and 4. In addition, the unstable ITO colloidal suspensions was modified using PEI, and the effect of modification on the LbL assembly process will be discussed in Chapter 4. During the LbL assembly, a polyelectrolyte precursor layer was often assembled prior to the assembly of nanoparticles. In Chapter 4, the effect of precursor layer charges on the following nanoparticle assembly will be studied in details.

Compared to other techniques, one of the drawbacks of LbL assembly method is that the buildup of thin film is rather slow due to its linear growth process. There is a need to develop *e*-LbL hybrid films composed of polyelectrolyte and nanoparticles. So far, there has not been a study on the *e*-LbL growth of thin film consisting of primarily inorganic nanoparticles. This kind of thin film is of the primary interest of this thesis because the interparticle connection is critical for achieving a desired functionality, such as obtaining optimal electrical conductivity.[63, 87] The *e*-LbL growth of bicomponent hybrid thin film $[PEI/SiO_2]_n$ and $[PAA/PEI\text{-}ITO]_n$ will be discussed in Chapter 5.

Preparation of functional materials and functional thin films are also of the interest of this thesis. In Chapter 6 and Chapter 7, conductive paper and transparent conductive thin films will be prepared by LbL assembly of $[PSS/ITO]_n$ thin films onto cellulose fibers and write-on transparency.

CHAPTER 2

EXPERIMENTAL PROCEDURES

This chapter gives the general details about the raw materials that were used for the LbL assembly, the sample preparation steps, and the characterization techniques. It does not include all of the experimental procedures. Some of the experimental procedures that are only applicable to one specific chapter will be described in that chapter.

2.1. Materials

Branched PEI (M_w ~ 750 000 g/mol), PSS (M_w ~ 70 000 g/mol, pK_a ~ –6.5 [122]), PAA (M_w ~ 100 000 g/mol), 11-mercaptoundecanoic acid (MUA), ITO nanoparticles (particle size = 10~100 nm, surface area ~ 27 m^2/g), and LUDOX® AS-40 SiO_2 colloidal suspensions (particle size ~ 30 nm, 40 wt%) were obtained from Sigma Aldrich. All of the materials were used as received without further purification. As shown in the transmission electron image (TEM) of the ITO nanoparticles (Figure 2.1), the size of ITO nanoparticles ranges from as small as 10 nm to as big as 100 nm. In other words, these ITO nanoparticles are polydispersed.

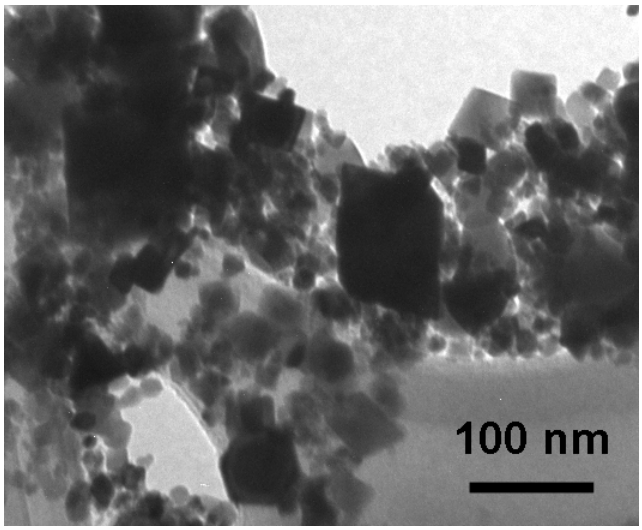

Figure 2.1 TEM image of ITO nanoparticles obtained from Sigma Aldrich.

2.2. LbL Assembly Procedure

2.2.1. Preparation of Polyelectrolyte Solutions

All aqueous polyelectrolyte solutions, including PEI, PSS, and PAA solutions, were prepared using a similar method. They were prepared at a concentration of 0.02 wt%, and the pH was adjusted to the desired value by using hydrochloric acid or sodium hydroxide. Unless specifically mentioned, 0.1 M NaCl was added into most of the polyelectrolyte solutions to maintain their ionic strength. All of the solutions were prepared using pure water (Millipore, resistivity ~18 MΩ·cm).

2.2.2. Preparation of ITO Colloidal Suspensions

Two types of ITO colloidal suspensions were prepared: unmodified ITO suspensions and PEI-modified ITO suspensions. The NaCl concentration for both kinds of suspensions was kept at 0.1 mM, and they were all prepared using pure water. The unmodified ITO suspensions were prepared by dispersing a certain amount of ITO nanoparticles into pure water, adding the NaCl, adjusting the pH of the suspensions to the desired value, and sonicating the suspensions for 10 min.

The PEI-modified ITO suspensions were prepared in exactly the same way except PEI stock solution is used instead of pure water.. The PEI stock solution was prepared first to a concentration of 0.1 wt% and a pH of 8. This PEI stock solution was then diluted to prepare PEI-modified ITO suspensions with PEI:ITO weight ratios of 1:200, 1:100, and 1:50. The NaCl concentration of the PEI-modified ITO suspension was also kept at 0.1 mM.

For easier description, unmodified ITO suspensions and PEI-modified ITO suspensions will be simply denoted as ITO suspension and PEI-ITO suspension in the following chapters.

2.2.3. LbL Assembly Procedure

All of the LbL assembly experiments were conducted in a similar manner, regardless of the substrate. LbL thin films were prepared on different substrates, including QCM crystals, silicon wafers, cellulose fibers, and PET transparent slides. The LbL assembly process was thus composed of three main stages: 1) substrate surface treatment to activate the substrate surface, 2) LbL assembly of the polyelectrolyte precursor layer to reduce the substrate surface effect or to render a uniformly charged surface, [20, 46, 90, 98, 123] 3) LbL assembly of the hybrid polyelectrolyte/inorganic nanoparticle films. The process of substrate surface treatment will be described in the corresponding experimental sections or chapters. In addition, the details of the precursor layer deposition are similar to the LbL assembly process of the polyelectrolyte/inorganic nanoparticle hybrid films. Therefore, the LbL assembly process of the PSS and the ITO inorganic nanoparticle will be described here as an example of the LbL assembly procedure used.

The LbL assembly process was conducted in a cyclic manner, during which the same assembly cycle was repeated for *n* times to assemble a thin film composed of *n* bilayers. For example, as shown in Figure 2.2, to assemble one bilayer of PSS/ITO, the substrate was first immersed in the PSS solution for 10 min, washed with pure water, blow dried with pure nitrogen gas, and then immersed in the ITO suspensions for 20 min, washed with pure water, blow dried with pure nitrogen gas. At this point, the process is counted as one assembly cycle, and one bilayer of PSS/ITO is thus prepared. By repeating this cycle for 10 times, a thin film composed of 10 bilayers of PSS/ITO can thus be prepared. For easier description, such a thin film is denoted as $[PSS/ITO]_{10}$. The thin film growth on a substrate during the LbL assembly of hybrid thin film $[PSS/ITO]_{10}$ is shown in Figure 2.3.

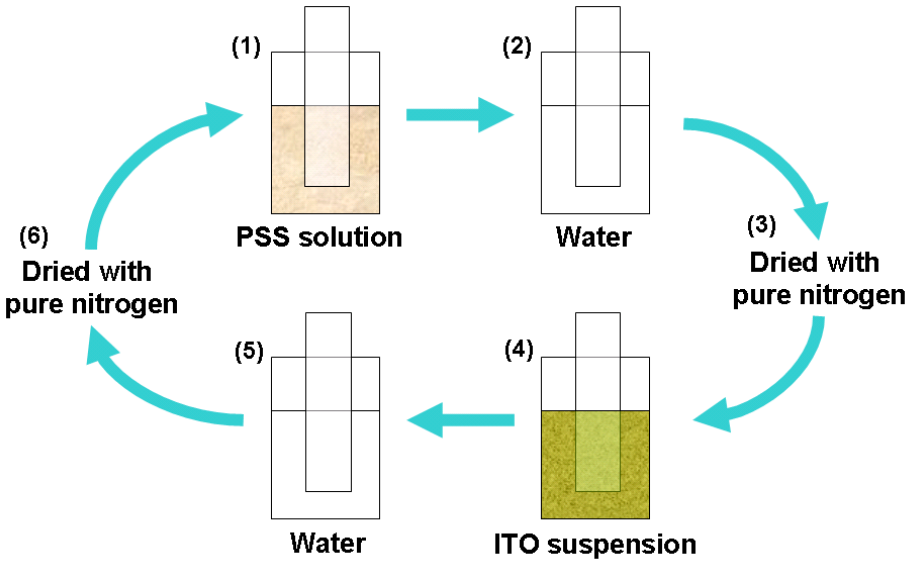

Figure 2.2 Schematic of one cycle of the LbL assembly of PSS and ITO nanoparticle: (1) immersing the substrate in PSS solution, (2) cleaning the substrate with pure water, (3) drying the substrate with nitrogen, (4) immersing the substrate in ITO suspension, (5) cleaning the substrate with pure water, and (6) drying the substrate with nitrogen.

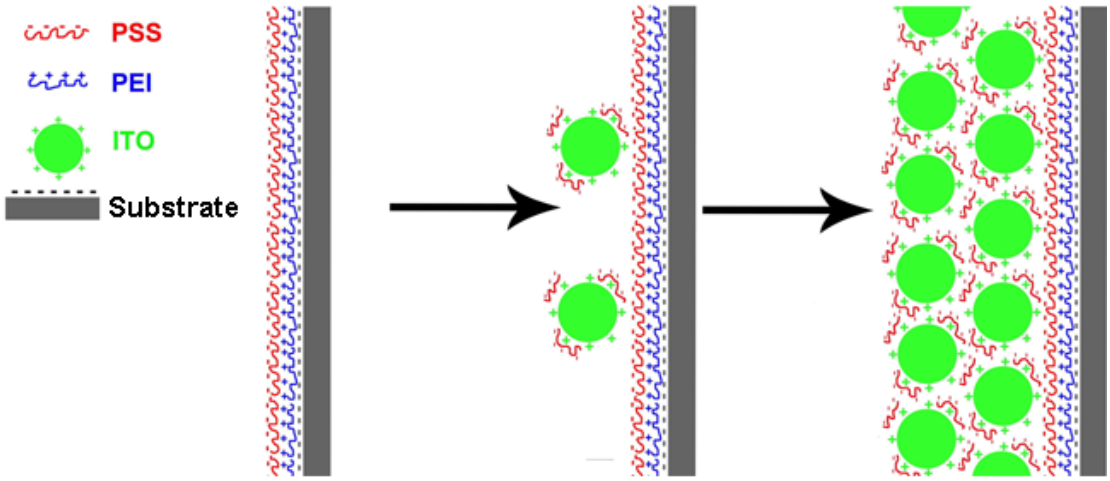

Figure 2.3 Schematic of an LbL assembled $[PSS/ITO]_n$ thin film on a substrate. The thin film is composed of the polyelectrolyte precursor layer $[PEI/PSS]_n$ and the hybrid thin film $[PSS/ITO]_n$. (The figure has been modified from the reference.)[63]

2.3. Characterization Techniques

2.3.1. ζ-potential and Particle Size Analysis

In order to evaluate the stability of the colloidal suspensions and the surface charge of the inorganic nanoparticles, the ζ-potential and the particle size of the suspensions were investigated by using Zetasizer (Malvern Instruments, Nano-ZS) at a pH ranging from 2 to 12. The setup for the measurement of the ζ-potential and the particle size is illustrated in Figure 2.4. As shown in Figure 2.4(a), the ζ-potential was measured using the electrophoretic light scattering (ELS) technique. Using this technique, an external electric field is applied onto the colloidal suspension, and the electrophoretic mobility of the charged colloids can be evaluated by the frequency shift of an incident laser beam.[43] This electrophoretic mobility of the colloidal particles can be used to calculate the ζ-potential using an approximation model. Here, the Smoluchowski approximation was used because of the large particle size as compared to the Debye length.[45] In this thesis, the NaCl concentration used in all of the ITO colloidal suspensions was around 0.1 mM. At this ionic strength, the Debye length is around ~30 nm,[47, 124] sufficiently smaller than the radius of ITO colloidal agglomerates (~200 nm in average according to size analysis). Therefore, this approximation is considered viable here, because when the pH of the colloidal suspensions was adjusted by adding hydrochloric acid or sodium hydroxide, the Debye length will be further reduced.

Similarly, in the colloids particle size can also be evaluated using the dynamic light scattering (DLS) technique (Figure 2.4(b)). According to this technique, the intensity fluctuation of the scattered light is related to the velocity of the Brownian motion of colloidal particles, which is related to the colloidal particle size. The measurement was done using a He-Ne laser (633 nm) at a measurement angle of 173°. The ITO suspensions at concentration of 0.01 wt% and 0.1 wt% has both been analyzed

for the particle size, and no apparent difference has been observed between these two solutions.

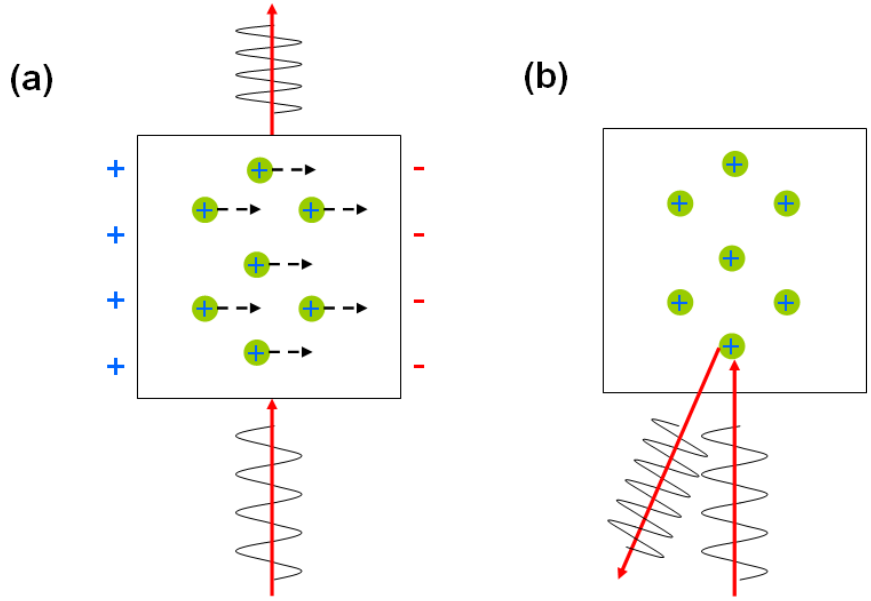

Figure 2.4 Schematic of (a) the setup for the ζ-potential measurement and (b) the setup for the particle size measurement.

2.3.2. Quartz Crystal Microbalance

The thin film buildup process was investigated using quartz crystal microbalance (QCM, Stanford Research System, Inc., QCM 200). QCM can be used to evaluate the mass of the LbL assembled thin film by measuring the change in the resonant frequency of the quartz crystal after each LbL assembly step. The frequency change of the crystal ($-\Delta f$) is linearly proportional to the mass change per area on the crystal surface ($\Delta m/A$), and their relationship is described by the Sauerbrey equation:[125]

$$\frac{\Delta m}{A} = \frac{\sqrt{\rho_q \mu_q}}{2 f_0^{\,2}} (-\Delta f) \qquad (2.1)$$

In this equation, ρ_q and μ_q represent the density and shear modulus of the crystal, and f_0 is the initial resonance frequency and A is the electrode area.

The quartz crystals used were AT cut crystals, coated with chrome/gold electrodes and resonating at 5 MHz at room temperature. In brief, the crystals were first cleaned with piranha solution (2:1 H_2SO_4:H_2O_2) (Caution! Piranha solution is extremely reactive and exothermic, and it should be handled with extreme care.) for 1 hour. The cleaned crystals were then immersed into 1 mM of MUA ethanol solution for over 24 hours to construct a self-assembled monolayer (SAM) of MUA on the gold electrode of the crystals. The SAM-modified crystals were then treated with 1 mM NaOH solution for 3 minutes to render a negative surface charge on the crystal. The treated crystals were then used as the substrates for the LbL assembly. These crystals were cleaned with pure water and blow-dried with pure nitrogen prior to the QCM measurement after every assembly step.

The evolution of resonant frequency of QCM crystals during the LbL assembly process can be presented in two different types of graphs. The LbL assembly process can be followed either by the accumulated frequency change, $-\Delta f$, or the frequency change of every step, $\Delta(-\Delta f)$. As shown in the schematics of these two types of graphs in Figure 2.5, during the assembly of an ideal *l*-LbL film, the plot for the $-\Delta f$ vs. LbL assembly steps is a straight line with a positive slope, whereas the plot for the $\Delta(-\Delta f)$ vs. LbL assembly steps is a flat line with a slope of zero. Each method has its own advantages. For example, the first method is suitable for characterizing an LbL process with a single growth regime, either linear growth or exponential growth. However, the second method is more suitable for characterizing an LbL deposition with multiple growth regimes, so that the two growth regimes can be distinguished more easily. This will be discussed more in the following chapters.

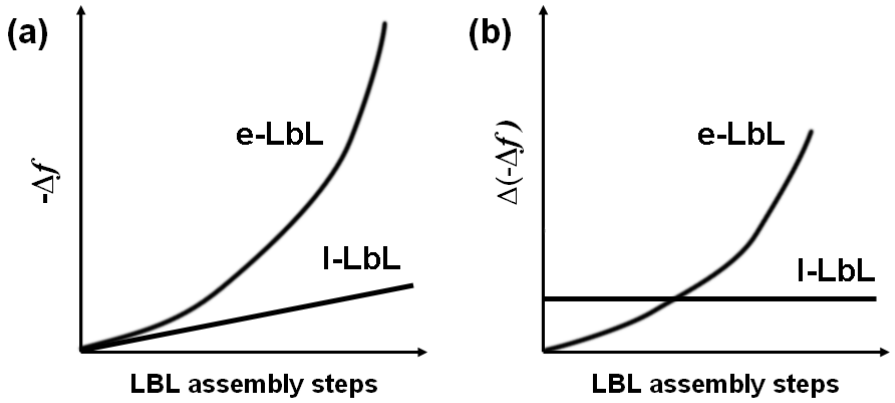

Figure 2.5 Schematic of two kinds of QCM result presentation for a linearly grown LbL film: (a) -Δ*f* versus LbL assembly steps, and (b) Δ(-Δ*f*) versus LbL assembly steps.

2.3.3. Atomic Force Microscopy

Atomic force microscopy (AFM, Park Systems, XE-100E) was used for the surface topography characterization and the electrical property characterization of thin films. The non-contact AFM was used for the surface topography characterization, whereas the conductive-AFM was used for the electrical property characterization.

2.3.3.1. Non-contact AFM

The surface topography was investigated using non-contact AFM of the samples in air. The AFM tips (Nanosensors^{TM}, NCHR) exhibit a nominal tip radius smaller than 10 nm, resonate approximately at 300 kHz, and have a spring constant around 40 N/m. The surface roughness was obtained from the AFM topography images. Because the surface roughness is scale-dependent, the scanning scale of the AFM images that were used for obtaining the roughness will also be presented.

2.3.3.2. Conductive AFM

Conductive AFM can be used to investigate the electrical percolated network in the materials.[126, 127] As shown in Figure 2.6, a bias voltage was applied to the bottom of the sample, and both the topography and the current were detected on the top of the sample.

The detected current is the current that percolated through the thickness of the sample and represents the end of the percolation paths. By comparing the topography image and the current image, one can identify the component that formed the percolated network. The AFM tips (Nanosensors^{TM}, NSC18/Cr-Au) used for conductive AFM were coated with Cr and Au, with a bulk resistivity of 0.01-0.05 Ω·cm, exhibiting a nominal tip radius around 50 nm, resonating approximately at 75 kHz, and exhibiting a spring constant around 3.5 N/m.

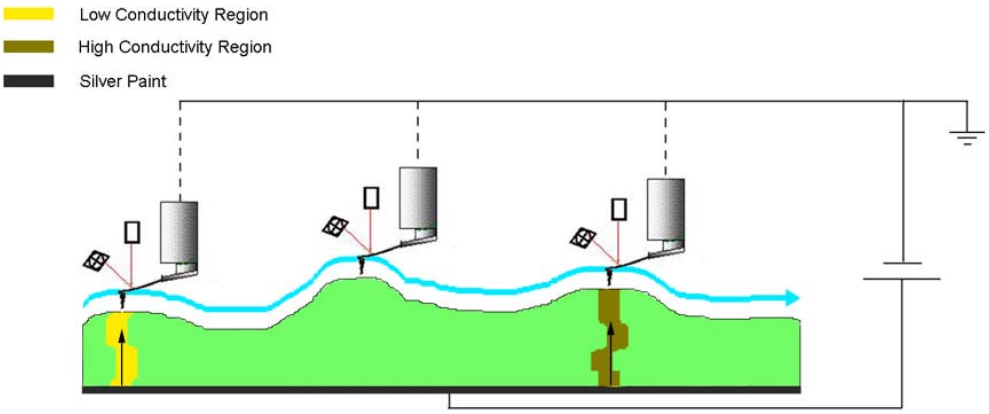

Figure 2.6 Schematic of the setup for the conductive AFM experiment.[63]

2.3.4. Scanning Electron Microscopy

The surface morphology of the samples was also investigated by scanning electron microscopy (SEM, LEO 1530 or Hitachi S800) at an accelerating voltage of 15 kV(LEO SEM) or 6 kV (Hitachi SEM). The elemental analysis was performed with energy dispersive spectroscopy (EDS).

2.3.5. AC Impedance Spectroscopy

The electrical property of some samples was evaluated by impedance spectroscopy. Using this technique, an AC electrical field (V) was applied through the

sample, and the AC current (I) was measured. The AC impedance (Z) of the sample can thus be calculated using the equation (2.2):[128]

$$Z(\omega) = \frac{V(\omega)}{I(\omega)} = \frac{V_{\max}\sin(\omega)}{I_{\max}\sin(\omega+\theta)} = Z' + jZ'' \qquad (2.2)$$

Both the voltage and current are sinusoidal signals, and for most of the materials, a phase shift (θ) can be observed between the voltage and the current, which is why the impedance is typically given as a complex number. The real impedance (Z′) and imaginary impedance (Z″) can either be plotted in the complex plane (Nyquist plot) or be plotted separately versus the frequency (Bode plot).

Prior to the measurement, the dimensions of samples were determined. Conductive silver paint (SPI supplies) was then applied to each end of the sample to form the contact electrode. The applied silver paint was then dried in an oven at 80 °C for 10 min to evaporate the non-conductive organic solvent. The impedance spectra were then collected between 10 mHz and 1 MHz using the frequency response analyzer (Solartron Instruments, SI 1260) combined with dielectric interface (Solartron Instrument, SI 1296). All of the spectra were collected using an AC voltage of 0.1 V without DC bias. Reproducibility was ensured by measuring at least three samples for each of the different conditions.

The AC conductivity of samples, σ_{AC}, for the whole frequency range, can be calculated using equation (3.3) and the DC conductivity σ_{dc} can be derived from the low frequency end. In equation (3.3), L and A are respectively the path length and the electrode cross-sectional area of sample.

$$\sigma_{ac} = \frac{1}{\sqrt{Z'^2 + Z''^2}} \times \frac{L}{A} \qquad (2.3)$$

CHAPTER 3

ENHANCING THE LBL ASSEMBLY OF PSS/ITO FILMS BY MODIFYING THE ITO PARTICLES USING PEI

3.1. Introduction

During the LbL assembly process, a colloidal suspension with high stability and high assembly rate is highly desirable.[102] The stability and the assembly rate of some colloidal suspensions can be significantly improved by modifying the nanoparticle surface with organic molecules through chemical adsorption.[129, 130] For example, Au or HgTe colloidal suspensions can be stabilized by mercapto-ligands, and the assembly rate of particles can be significantly enhanced.[19, 131, 132] Normally, this surface chemical modification process was done during the colloidal particle synthesis process, and ligands can chemically attach onto the particle surface once the particles are synthesized, serving as both the colloidal suspension stabilizer and the particle surface modifier.

During the LbL assembly of PSS and ITO, the ITO suspension was not very stable and that the small particles tended to agglomerate and precipitate after a short period of time. Therefore, one important objective is the stabilization of ITO colloidal suspension for the LbL assembly. The ITO suspension stability can be improved by modifying the ITO suspension with branched PEI. PEI can be used as a colloidal suspension stabilizer because it can physically adsorb onto the negatively-charged particle surfaces.[51-53, 55] For example, PEI has been used as a dispersion stabilizer for many colloidal suspensions of nanoparticles with a negative surface charge such as Si,[52] TiO_2,[51] Si_3N_4,[50] SiC,[133] and ZrO_2.[54] PEI has also been shown to affect the electrophoretic deposition behavior of TiO_2 nanoparticles.[51] The large number of positively-charged polymer chains attached on the particle surface can provide strong

electrostatic and steric repulsive forces between particles, and thus stabilize the colloidal suspension. Improving the stability of the ITO colloidal suspension provides the opportunity to simultaneously enhance the growth rate of LbL assembled ITO thin films.

This chapter demonstrates the stabilization of ITO suspension using PEI, and the enhancement of LbL assembly rate of $[PSS/ITO]_n$ films by using PEI-modified ITO suspensions at an appropriate PEI:ITO ratio.

3.2. Experimental Procedure

The stability of the ITO colloidal suspensions was evaluated by measuring the ζ-potential and analyzing the particle size of each suspension. The deposition rate of PEI-modified ITO during LbL assembly was compared with the unmodified ITO suspension, using QCM and AFM. The interaction between the PEI and the ITO surface was investigated using Fourier transform infrared spectroscopy (FTIR). The experimental procedures for ζ-potential measurement, particle size analysis, QCM, and AFM have been described in Chapter 2, and only the procedure for FTIR will be described here.

3.2.1. Fourier Transform Infrared Spectroscopy

The interaction between PEI and ITO was investigated using FTIR spectroscopy (Nicolet Instrument Corp., Nexus 870) at a resolution of 2 cm^{-1} with 300 scans. The FTIR sample of PEI-ITO was prepared by drying the PEI-ITO suspension on an IR-transparent CaF_2 crystal. In order to intensify the signal, the more concentrated PEI stock solution was used to prepare the PEI-ITO suspension. In brief, 0.001g ITO nanoparticles were directly dispersed in 2 ml PEI 0.1wt% stock solution; a thin film was then made by drying a few drops of the prepared dispersion onto the CaF_2 crystal, which is transparent to infrared light for wavenumbers between 4000 and 1000 cm^{-1}. The transmission IR spectra of PEI-ITO and pure PEI were obtained for the range of 4000 to 400 cm^{-1}. During

the sample preparation, the pH of the samples was neither maintained nor varied by purposely adding acid or base.

3.3. Results and Discussion

3.3.1. ITO Suspension Stabilization

The ζ-potential and the particle size analysis of both the unmodified and PEI-modified ITO suspensions, at different PEI:ITO ratios obtained for pH values from 2 to 12, are presented in Figure 3.1 and Figure 3.2, respectively. As shown in Figure 3.1, ITO nanoparticles in the ITO suspension were positively charged at a pH below 5. The positive ζ-potential value decreased with increasing pH and finally reversed to a negative value at a pH above 6. Therefore, the isoelectric point (IEP) of the ITO suspension, which is the pH value where the ζ-potential reverses sign, was around 5.5. On the other hand, when small amounts of PEI were added into the ITO suspension, the normally negatively charged ITO particle changed to positive surface charge, and the IEP of all of the PEI-ITO suspensions shifted to pH around 11, at which point the PEI is neutralized.[134] In other words, the pH range in which the ITO nanoparticles exhibited a positive surface charge was broadened by the PEI modification. Since PEI can present a positive charge even in acidic and mild basic environments,[134] the modified ITO suspension can thus be positively charged at a relatively high pH value. In addition, when the ratio of PEI:ITO was increased from 1:200 to 1:40, the ζ-potential of the suspensions also increased. For example, at pH around 6.5, the ζ-potential of PEI-modified ITO suspensions at PEI:ITO ratios of 1:200, 1:100, and 1:40 were 14.1, 19.1, and 26.2 mV respectively.

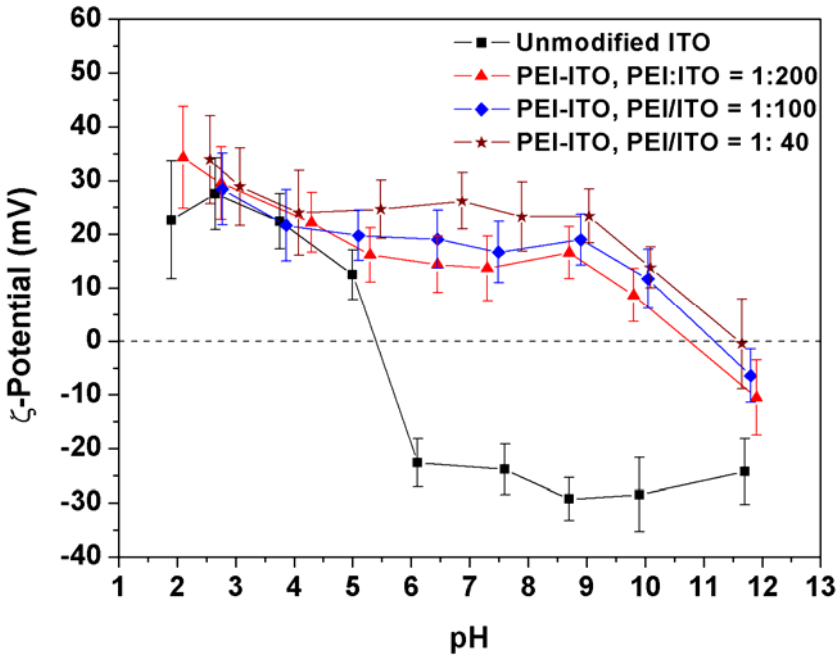

Figure 3.1 ζ-potential of the ITO and PEI-ITO suspensions at a pH range from 2 to 12.[118]

The particle size distribution of agglomerates in the nanoparticle suspensions can be used to evaluate the stability of the suspensions. Large agglomerates indicate an unstable nanoparticle suspension. As shown in Figure 3.2, in the ITO suspension, the majority of the particles at a pH below 4 were approximately 250 nm. These particles were small agglomerates composed of even smaller individual ITO nanoparticles (according to Figure 2.1, the particles are generally between 10 and 100 nm) and they were relatively stable in the suspension. At a pH above 4, the particles started to create larger agglomerates, and the particle size drastically increased to over 1000 nm. Therefore, the ITO suspension at the pH of 6.5 cannot be used for LbL assembly since this suspension is not stable. In contrast, in all the three PEI-ITO suspensions, the particle size drastically decreased at moderate pH range compared to the unmodified ITO suspension. It was found that the higher the PEI:ITO ratio in the PEI-ITO suspension, the

more stable the suspension became in the higher pH value. For example, at a pH around 9, the particle sizes of the unmodified suspension, and the PEI-ITO suspensions at PEI:ITO ratios of 1:200, 1:100 and 1:40 were 755, 378, 236, and 205 nm respectively. The suspensions became more and more stabilized as the PEI content was increased. In other words, the pH range in which a stable ITO colloidal suspension can be obtained was broadened due to the PEI modification. The stabilization of the ITO suspension due to the PEI modification is due to both electrostatic and steric repulsive forces between the PEI polymer chains on the ITO surface. PEI-ITO suspensions at different PEI:ITO ratios at a pH of 6.5 were then used to study the assembly rate. It is worth mentioning that the size values above 1000 nm were actually erroneous simulating results due to the extremely big agglomerate size. However, these values are still used here to compare with values from the stable suspensions.

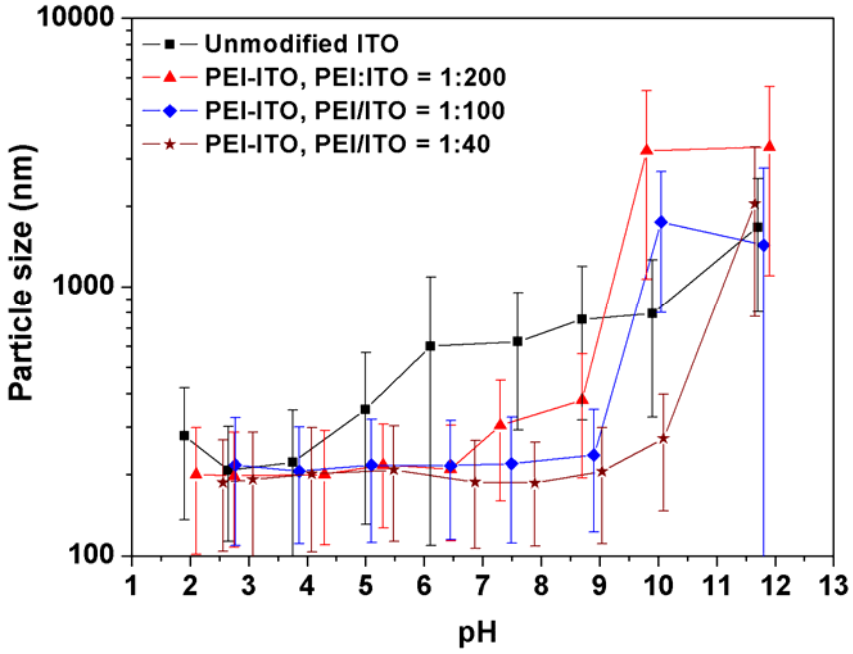

Figure 3.2 The particle size analysis of the ITO and the PEI-ITO suspensions at pH values ranging from 2 to 12.[118]

3.3.2. Interaction between PEI and ITO

The particle-polymer interaction on the ITO particle surface will induce electron redistribution between the functional groups of PEI and the ITO surface. This electron redistribution could be detected using FTIR by examining the change of the functional group vibration peaks between pure PEI and the PEI that is attached onto the ITO surfaces. In the following sections, the PEI that is attached on the ITO surface is designated as PEI(ITO) for easier description. The IR spectra of both PEI and PEI(ITO) are shown in Figure 3.3 and Table 3.1, respectively, and the IR peaks were assigned according to referenced values.[135] As shown in Figure 3.3, the IR peaks related to the amine functional groups of PEI(ITO) showed a clear change in terms of both peak frequency and relative peak intensity, compared to the IR peaks of pure PEI. For example, the NH_2 asymmetric and symmetric stretching peaks could be observed at 3357 and 3279 cm^{-1} in the PEI spectrum, but only one broad peak was observed at 3257 cm^{-1} in the IR spectrum of PEI(ITO). Furthermore, only one broad NH_2 scissoring peak could be observed at 1579 cm^{-1} in the PEI spectrum, but two adjacent peaks were observed at 1654 and 1606 cm^{-1} in the PEI(ITO) spectrum. The new emerging peak at 1654 cm^{-1} is assigned to NH_3^+ scissoring bending.[136, 137] This peak is probably embedded in the broad peak of NH_2 scissoring in the PEI spectrum, and it is intensified due to the adsorption onto the ITO surface. In addition, the peak intensity of the NH_2 scissoring peak relative to CH_2 scissoring peak drastically increased in the PEI(ITO) case, indicating the significant electron redistribution through the amine group.

In contrast, most of the IR peaks related to the CH_2 group in the two spectra did not show any obvious differences. As can be seen in Figure 3.3, the CH_2 asymmetric stretching and CH_2 symmetric stretching peaks slightly shifted to higher frequency in PEI(ITO) but maintained the same relative peak intensity. However, CH_2 scissoring, CH_2 wagging, and CH_2 twisting peaks remained at the same frequency in both spectra. The relative peak intensity between CH_2 wagging and CH_2 twisting increased for PEI(ITO),

which can be attributed to the conformational change of PEI chains on the ITO surface.[55]

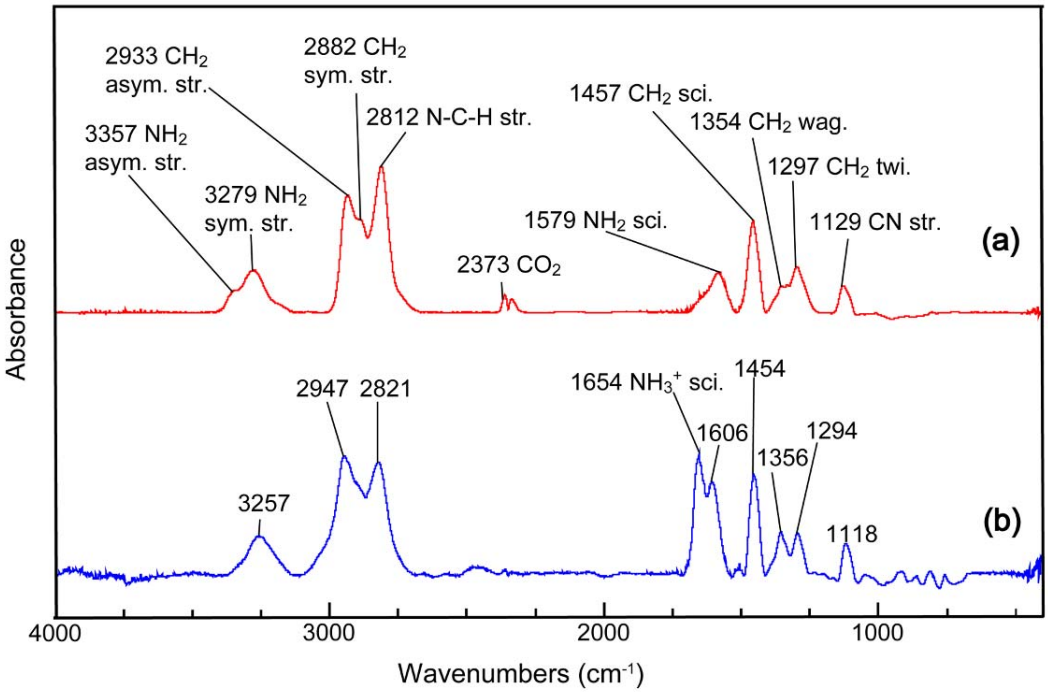

Figure 3.3 The FTIR spectra of (a) PEI, and (b) PEI(ITO). In the spectra, the meaning of the labels is as follows: asym. = asymmetric, sym. = symmetric, str. = stretching, sci. = scissoring, wag. = wagging, and twi. = twisting.[118]

The peaks related to NH_2 changed much more significantly than those related to CH_2, suggesting that the interaction between PEI and ITO is dominated by the interaction between the amine groups of PEI and the ITO particle surface. Previously, it has been found that the interaction between amine groups and oxide surface can be contributed by many types of forces, including electrostatic force between protonated amine group and the negative surface charge,[138, 139] hydrogen bonding between amine groups and surface hydroxyl groups,[140] and correlation bonding between Lewis base of N atoms in PEI and Lewis acid of metal ions on particle surface.[54, 140] It is out of the scope of this thesis to exactly identify which type of interaction force is dominant during the PEI adsorption on

the ITO surface. However, the intensification of NH_3^+ scissoring peak at 1654 cm^{-1} indicates that the electrostatic force might contribute significantly to the interaction between PEI and negatively charged ITO surface.

Table 3.1 IR vibration peaks of PEI with and without ITO nanoparticles.[118]

Peaks	PEI (cm^{-1})	PEI with ITO (cm^{-1})
NH_2 asymmetric stretching	3357	--
NH_2 symmetric stretching	3279	3257
NH_2 scissoring	1579	1606
NH_3^+ scissoring	--	1654
C-N stretching	1129	1118
CH_2 asymmetric stretching	2933	2947
CH_2 symmetric stretching	2882	--
N-C-H stretching	2812	2821
CH_2 scissoring	1457	1454
CH_2 wagging	1354	1354
CH_2 twisting	1297	1294

3.3.3. Enhanced Assembly Rate of ITO

The assembly rate of ITO nanoparticles during the LbL process was investigated using QCM. The frequency change (i.e., $-\Delta f$) of QCM crystals, which was measured after each step of LbL assembly, is linearly proportional to the change of mass on the crystals due to a rigid-film deposition.[125] The accumulated frequency changes of all LbL assembly layers from all suspensions are shown in Figure 3.4. In this figure, all of the odd-numbered assembly layers are PSS assembly layers, and all of the even-numbered assembly layers are ITO assembly layers. As shown in the figure, the $-\Delta f$ increased linearly during the LbL assembly. In addition, the increase of $-\Delta f$ during the PSS

assembly steps was almost negligible compared to that during the ITO assembly steps, which means that a relatively small amount of PSS was assembled compared to the ITO nanoparticles. This phenomenon has also been observed in other studies, such as the LbL assembly of PEI and proteins,[120] PSS and TiO_2 nanoparticles,[141] and polydimethyldiallyl ammonium chloride (PDDA) and SiO_2.[141] This result is not unexpected since the ITO-coated surface is less positive than the PEI-coated surface,[63] and the available number of positive sites on the ITO nanoparticles will be fewer than that for the hyperbranched PEI chains.

The ITO assembly rate from PEI-ITO suspensions was significantly affected by the PEI content. According to Figure 3.4 and Table 3.2, the $\Delta(-\Delta f)$ of ITO assembly from the PEI-ITO suspensions at the PEI:ITO ratio of 1:200 was 135±28 Hz, exhibiting more than twice the frequency change, as compared to the assembly from the unmodified ITO suspension. In addition, the increase of PEI:ITO ratio to 1:100 slightly decreased the average $\Delta(-\Delta f)$ of ITO assembly steps, while further increase in the PEI concentration significantly decreased the ITO assembly rate. One of the reasons for this phenomenon is probably related to the presence of extraneous PEI chains in the colloidal suspension during the PEI modification.[142] In this case, due to the higher diffusivity of polymer chains, the surface assembly will be dominated by the PEI adsorption, and thus fewer nanoparticles can be adsorbed during one step. In contrast, at the PEI:ITO ratio of 1:200, there were more ITO nanoparticles than the PEI chains could completely cover and few if any PEI chains were left in the suspension. Therefore, only the PEI-ITO nanoparticles could diffuse to the substrate surface. Another possible reason is the modest interparticle repulsive force between the PEI-ITO nanoparticles when the PEI:ITO ratio is at 1:200. Higher PEI:ITO ratio will increase the particle surface charge, which will introduce stronger interparticle repulsive force and thus decrease the assembly rate. This will be discussed further in the following section.

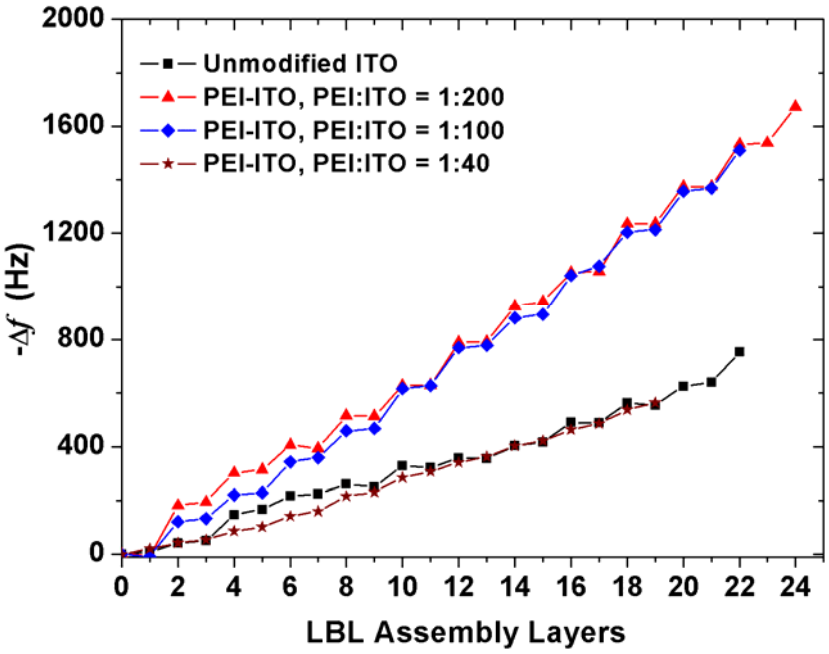

Figure 3.4 The -Δ*f* of QCM crystals during LbL assembly of PSS and either ITO or PEI-ITO.[118]

Table 3.2 The QCM and AFM results for ITO assembly of ITO, and PEI-ITO at PEI:ITO ratios of 1:200, 1:100, and 1:40.[118]

Sample	Average Δ(-Δ*f*) of ITO steps (Hz)	Surface coverage (%)	RMS roughness [a] (nm)
Unmodified ITO	64±26	2.4 ±0.6	6.8±1.6
PEI:ITO = 1:200	135±28	8.3±0.4	21.4±3.2
PEI:ITO = 1:100	120±20	7.2±0.5	16.3±4.8
PEI:ITO = 1:50	41±8	4.0±0.3	13.9±2.5

[a] The roughness is obtained from the AFM (10 μm ×10 μm) images.

3.3.4. Enhanced Substrate Surface Coverage

The assembly rate of ITO nanoparticles during the LbL process was further examined by coating silicon wafers with one layer of ITO from the same ITO

suspensions used for the QCM experiments, and observing the wafer surface coverage by ITO nanoparticles using AFM. The AFM topography images of silicon wafers that were coated from either the ITO or PEI-ITO suspensions at different PEI:ITO ratios for one bilayer are shown in Figure 3.5. As shown in Figure 3.5(a), only a few nanoparticles can be observed on the wafer that was coated using the unmodified ITO suspension. When the PEI:ITO ratio was 1:200 or 1:100, many more nanoparticles can be adsorbed onto the wafer during one step from the PEI-ITO suspensions (Figure 3.5(b) and (c)). However, when the PEI:ITO ratio reached to 1:40, the ITO nanoparticles that were adsorbed during one step significantly decreased (Figure 3.5(d)). According to Table 3.2, the surface coverage of silicon wafers that were coated from the PEI-ITO suspension at the PEI:ITO ratio of 1:200 exhibited the highest surface coverage ratio of 8.3% and the highest surface root-mean-square (RMS) roughness of 21.4 nm due to the assembled nanoparticles. Therefore, the PEI-ITO suspension at the PEI:ITO ratio of 1:200 exhibited the highest assembly rate.

The QCM result suggests that about twice the amount of ITO nanoparticles were deposited onto the substrate surface during each LbL step from the PEI-ITO suspension, compared to that from the unmodified ITO suspension. This technique measures the mass of nanoparticles that were deposited on the crystal surface during multiple LbL bilayers. However, after the first step of assembly, the surface coverage on the silicon wafers was found to be more than three times the number of nanoparticles for the PEI-ITO suspension at PEI:ITO ratio of 1:200 than that for the ITO suspension. This discrepancy can be attributed to the fact that the QCM results were obtained after multiple bilayers of deposition, whereas the AFM result was obtained from the first bilayer only. In addition, the AFM image analysis only takes into account the 2-D surface area that is covered by nanoparticles, whereas the QCM analysis evaluates the 3-D volume of all nanoparticles.

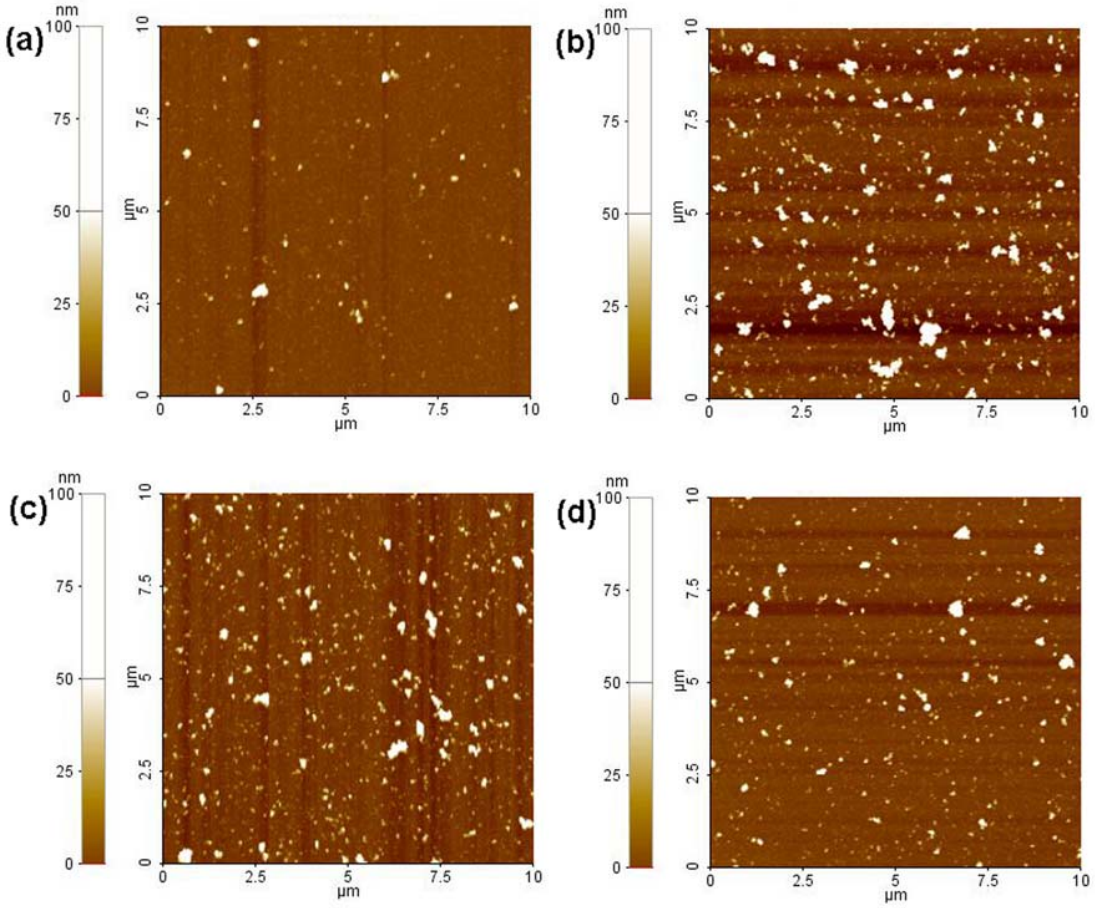

Figure 3.5 AFM images of silicon wafers coated with one bilayer of PSS and (a) unmodified ITO and PEI-ITO at PEI:ITO ratios of (b) 1:200, (c) 1:100, and (d) 1:40. The brightness and the contrast of all four images were adjusted to the same value for better comparison.[118]

3.3.5. Mechanisms for Enhanced ITO Assembly Rate

One of the reasons for the enhanced assembly rate is due to using the same pH condition between PSS solution, PEI-ITO suspension and the washing water. During the LbL assembly of PSS and ITO, ITO was assembled at a pH of 2.7. However, the subsequent washing and PSS assembly steps were both performed at higher pH value (pH~5.6 for the washing water, and pH~6.5 for the PSS assembly). This pH discrepancy between assembly steps will lessen the layer-to-layer interaction forces due to the decrease of the ITO surface charge when pH increases.[63, 104] The interaction between the ITO and the PSS layers is then less electrostatically attractive or even repulsive, due

to the lower and finally reversed surface charge of ITO at a higher pH. Researchers have tried to resolve this issue by adjusting the pH of the washing water to fit with the assembly steps so that the substrate could be washed under the same pH as the assembly solution.[143, 144] However, this method will only keep the surface charge of the substrate the same during the assembly and washing step. Once the substrate has been dipped into the new solution at a different pH value, the surface charge of the substrates will immediately change so that the interaction forces between different layers will change. In addition, it is not very convenient to frequently adjust the pH of washing water during the assembly process. One of the advantages of this method is that both the PSS and the PEI-ITO can be assembled at similar pH around neutral value. Therefore, no pH adjustment is necessary during the entire assembly process, and the interaction between two adjacent layers will not change as the LbL assembly proceeds.

Another reason for an enhanced assembly rate of PEI-ITO is due to the enlarged interaction site between the PEI-ITO nanoparticle and the PSS polymer chains. In Figure 3.6, the interaction between the PSS layer and either the unmodified ITO or the PEI-ITO layer are illustrated. When the ITO is used for the LbL assembly, the number of interaction sites between the ITO layer and the PSS layer are limited due to the small ITO surface area. In addition, the interaction force between PSS and ITO layers is mainly due to the electrostatic force from the oppositely charged PSS layers and ITO layers. This interaction force tends to decrease during the LbL process due to the pH value discrepancy between the ITO and PSS assembly steps. On the other hand, when the PEI-ITO is used for the LbL assembly, the number of interaction sites between the PSS layer and the PEI-ITO layer are significantly enlarged due to the presence of numerous dangling PEI polymer chains surrounding the ITO nanoparticles. In addition, the interaction force between the two adjacent layers is now not only contributed by the electrostatic attraction between the PEI and PSS, but also contributed by the polymer chain entanglement and interpenetration. The interaction force between PSS and PEI-ITO

is thus much stronger than that between PSS and unmodified ITO, and this force will not change during the assembly since both the PEI-ITO layer and the PSS layer are assembled at the same pH.

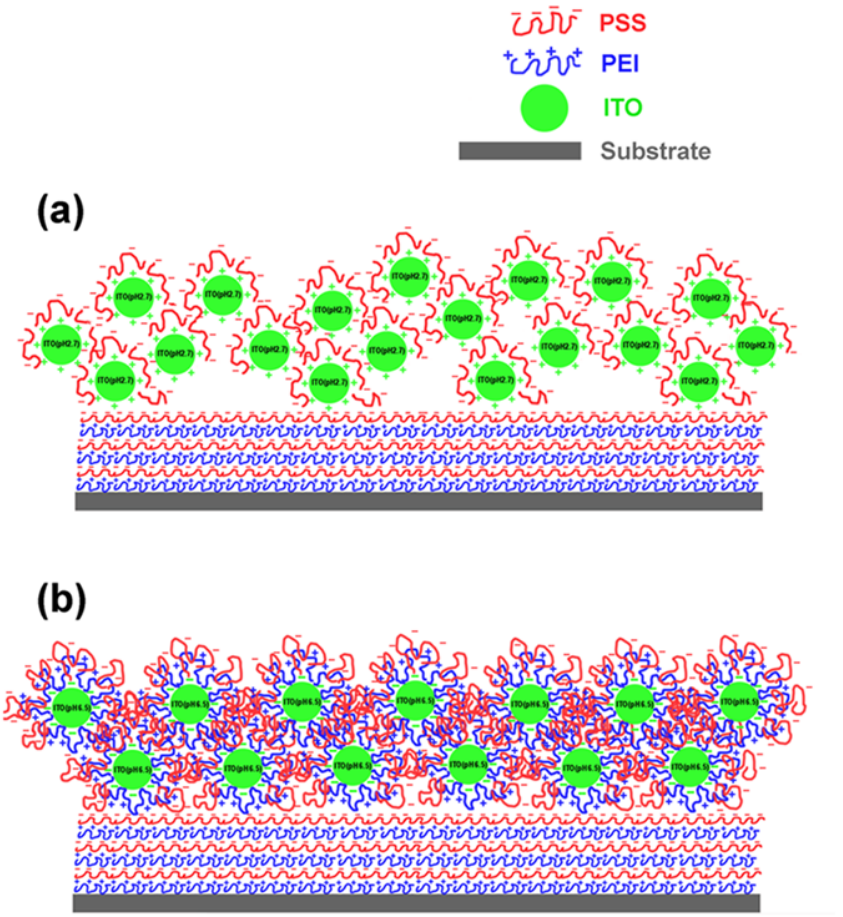

Figure 3.6 The interaction between the ITO layer and the PSS layer during two LbL experiments: (a) LbL assembly of ITO and PSS, and (b) LbL assembly of PEI-ITO and PSS.[118]

The third likely reason for the enhanced assembly rate of the PEI-ITO is the mild interparticle repulsive forces between PEI-ITO nanoparticles. As shown in Figure 3.1, the ζ-potentials of the ITO suspension at a pH of 2.7 and the PEI-ITO suspension at a pH of 6.5 at the PEI:ITO ratio of 1:200 are around 28 and 15 mV, respectively. The PEI-ITO surface at a pH of 6.5 is less charged than that of the unmodified ITO at a pH of 2.7. Therefore, the repulsive forces between nanoparticles in the modified suspension will be

less strong than those in the unmodified suspension. Previously, it has been found during simulation studies that the strong electrostatic repulsive forces make it impossible for the nanoparticles to fully cover the substrate surface during one assembly step.[145] In other words, a weaker repulsive force between nanoparticles will favor the nanoparticle adsorption during the LbL assembly. This phenomenon has also been found to occur when SiO_2 and TiO_2 nanoparticles were LbL assembled.[68] In addition, this phenomenon also explains why the assembly rate of PEI-ITO at PEI:ITO ratios of 1:100 and 1:40 is lower than that of PEI-ITO at PEI:ITO ratio of 1:200, since the ζ-potential of the modified suspension increases from 15 to 26 mV when the PEI:ITO ratio increased from 1:200 to 1:40.

3.4. Conclusions

PEI was used to modify the ITO colloidal suspensions to enhance the ITO assembly rate during the LbL assembly. Due to the PEI modification, the ITO suspension became stable over a wider pH range, keeping a positive surface charge and a relatively stable particle size. With higher PEI content, the pH range to obtain a stable suspension is wider. FTIR results suggest that the interaction between PEI and ITO is dominated by the interaction between amine groups of PEI and the ITO particle surface.

The ITO assembly rate from unmodified and PEI-modified ITO suspensions was compared by measuring the resonant frequency change of QCM crystals during the LbL assembly and by calculating the surface coverage of silicon wafers that are coated with one layer of ITO nanoparticles from AFM images. According to the QCM results, approximately twice the amount of ITO can be adsorbed during one single assembly step from the PEI-ITO suspension at the PEI:ITO ratio of 1:200 than that from the unmodified ITO suspension. The AFM results suggest that when the PEI:ITO ratio is 1:200, the surface coverage by one layer assembly of ITO nanoparticles is more than three times higher for the PEI-ITO suspension than for the unmodified suspension. However, when

the PEI:ITO ratio is increased beyond 1:200, the assembly rate of the PEI-ITO significantly decreased probably due to the excess amount of PEI polymer chains remaining in the colloidal suspensions that could interfere with the ITO nanoparticle deposition, as well as the increased interparticle repulsive force due to the increased surface charge intensity.

The enhanced assembly rate is attributed to three reasons. First, the enhanced ITO assembly rate is attributed to the non-decreasing electrostatic interaction force between the PSS and PEI-ITO during the LbL assembly process because the PSS assembly step, PEI-ITO assembly step, and the washing step are performed under similar pH conditions. Second, the improvement is also attributed to the larger number of interaction sites present between the PEI-ITO and the PSS, as well as the polymer chain entanglement and interpenetration between the PEI-ITO and PSS layers. Third, low repulsive forces between the mildly charged nanoparticles in the PEI-ITO suspension at the ideal PEI:ITO ratio also contributed to the high assembly rate.

This chapter addressed the weak interaction between the nanoparticles and the polyelectrolyte layer during LbL assembly by modifying the colloidal suspension with PEI, and thus the assembly rate was much enhanced by using a modified suspension containing an ideal PEI:ITO ratio.

CHAPTER 4

THE EFFECT OF PRECURSOR-LAYER SURFACE CHARGE ON THE LAYER-BY-LAYER ASSEMBLY OF POLYELECTROLYTE / NANOPARTICLE MULTILAYERS

4.1. Introduction

During the LbL assembly of hybrid thin films that are composed of polyelectrolytes and inorganic nanoparticles, one often assembles a precursor layer that is composed of several bilayers of polyelectrolytes before the beginning of inorganic nanoparticle deposition, to reduce the substrate surface effect or to render a more uniformly charged surface.[20, 46, 90, 98, 123] This precursor layer is believed to facilitate the subsequent nanoparticle adsorption,[20, 90] however, no detailed studies have been found to support this hypothesis.[46] To date, there has been no detailed study about the effect of the precursor polyelectrolyte layer on the subsequent nanoparticle assembly.

This chapter focuses on the effect of the polyelectrolyte precursor layer $[PEI/PSS]_4$ on the LbL assembly of $[ITO/PSS]_{9.5}$ films at various pH and ionic strength conditions. It is shown that the surface charge of the precursor layer could change from negative to positive if the ITO is deposited at a pH value lower than that of PSS deposition. The changed surface charge of the precursor layer results in a two-regime LbL assembly process, and thus the precursor layer surface charge significantly affects the first regime of “recovery regime”, whereas the second regime of “linear growth regime” is unaffected. The ionic strength in the PSS solution also only affects the length of the “recovery regime” when unmodified ITO is used, and the film buildup rate in the “linear growth regime” is unaffected.

4.2. Experimental Procedures

The surface charge of precursor layers was studied by using electrochemical impedance spectroscopy (EIS), and the LbL assembly process was studied by using QCM and AFM. The polyelectrolyte solution and the ITO colloidal suspensions were prepared by following the same procedures described in Chapter 2. The ζ-potential measurement, QCM, and AFM study were also conducted by following the same procedure described in Chapter 2. Therefore, only the EIS procedure will be described here.

4.2.1. Electrochemical Impedance Spectroscopy

The surface charge of precursor layers was investigated by using EIS. EIS was used to detect the surface charge of thin films on working electrodes of three-electrode EIS cells. Basically, the electron transfer resistance of the redox couple of ferricyanide/ferrocyanide, $[Fe(CN)_6]^{3-/4-}$, on the working electrode will be sensitive to the surface charge.[107, 146] Due to the repelling force between the negative surface charge and the negative redox ions, the electron transfer resistance of a negatively charged surface will be much higher than that of a positively charged surface.

A commercially available conductive ITO glass (surface area ~ 0.1 cm^2, surface resistance ~2 Ω/square) was used as the working electrode for the electrochemical measurements. The ITO electrode was cleaned with acetone, isopropanol, then sonicated in KOH/Alconox (1:1) mixing solution for over 2 h, flushed with pure water, and dried with pure nitrogen gas. The ITO glass electrode was then coated with a precursor layer of $[PEI/PSS]_4$ following the same procedure as described in the previous section. The precursor-layer modified ITO electrode was then used for the electrochemical measurements.

Here, a conventional three-electrode cell, consisting of the precursor-layer modified ITO working electrode, a platinum wire counter electrode, and a saturated calomel electrode (SCE) as the reference electrode, was used for the electrochemical

measurement. The SCE reference electrode was connected to the working volume with a Luggin capillary to avoid cross contamination. All potentials were reported with respect to the SCE. The EIS measurement was performed using an electrochemical impedance analyzer and potentiostat (EG&G, Model 6310). The EIS measurement was performed in 5mM $[Fe(CN)_6]^{3-/4-}$ (1:1) – 0.1 M KCl – 10 mM phosphate buffer (pH 7 or pH 5) solutions. The impedance spectra were recorded at the open potential of -140 mV, frequencies ranging from 100 kHz to 10 mHz. The experimental data were simulated using equivalent circuits with the Zview software.[147]

4.3. Results and Discussion

4.3.1. EIS Characterization of Surface Charge

EIS can be used to characterize the surface charge of organic layers on working electrodes.[107, 146] When the organic layer is negatively charged, the diffusion of $[Fe(CN)_6]^{3-}$ and $[Fe(CN)_6]^{4-}$ ions to the electrode will be hindered due to the repelling force between the negatively charged surface and the negatively charged redox ions. On the other hand, when the organic layer is positively charged, the diffusion process will be promoted due to the attractive force between the positively charged surface and the negatively charged redox ions. This prevention/promotion of redox ion diffusion towards the working electrode can be characterized by the charge transfer resistance, R_{ct}, of the redox reaction between $[Fe(CN)_6]^{3-}$ and $[Fe(CN)_6]^{4-}$. A larger R_{ct} indicates the prevention of the ion diffusion to the surface and thus the formation of a negatively charged surface, whereas a smaller R_{ct} indicates the promotion of ion diffusion and thus a positively charged surface. Usually, the difference in values for R_{ct} between the negatively and positively charged surfaces is several orders of magnitude. Figure 4.1 depicts the effect of the precursor layer $[PEI(8.5)/PSS(6.5)]_4$ on the diffusion of redox ions towards the electrode surface. When the precursor layer is immersed in a solution at a pH above the

pH of the PSS solution, which is 6.5, the precursor layer is negatively charged due to the outermost PSS layer. Under this condition, the redox ions will be repelled from the electrode surface, and the R_{ct} should be high. On the other hand, if the precursor layer is immersed in a solution at a pH below 6.5, the PEI chains will significantly gain positive charges, and the precursor layer surface will convert into a positively charged surface. This positively charged precursor layer will attract the redox ions to the electrode surface and thus significantly reduce the R_{ct}. In addition, the different interaction between the precursor layer surface and the redox ions will result in different thicknesses for the interaction layer, t_{dl}, that provides the double layer capacitance Q_{dl}, for the charge transfer resistance. As shown in Figure 4.1, the interaction layer thickness is larger when the precursor layer is negatively charged at a pH above 6.5, which will result in a smaller double layer capacitance than for when the interaction layer is thinner.

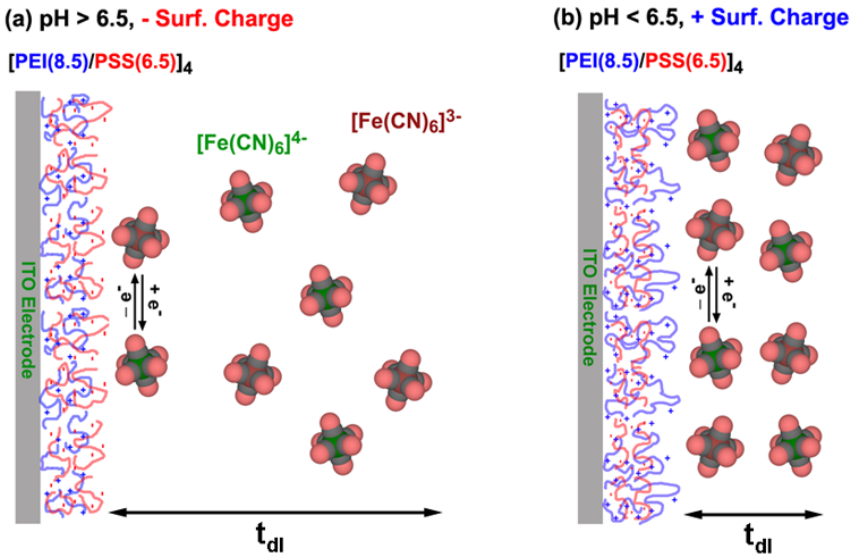

Figure 4.1 Schematics of the effect of the precursor layer $[PEI(8.5)/PSS(6.5)]_4$ on the $[Fe(CN)_6]^{3-/4-}$ redox reaction. The precursor layer (a) repels the redox ions at the pH above 6.5 due to the negatively charged surface or (b) attracts the redox ions at the pH below 6.5 due to the positively charged surface.[148]

The EIS spectra for the redox reaction in the presence of 5 mM $[Fe(CN)_6]^{3-/4-}$ at the pH of 5 and 7 are shown in Figure 4.2. In this figure, the Nyquist impedance plot and

the phase angle Bode plot are shown. The EIS spectra were simulated using the expected equivalent circuit for a charge transfer resistance process.[149] The equivalent circuit, shown as an inset in Figure 4.2(a), consists of a solution resistance R_s, a charge transfer resistance R_{ct}, a constant phase element Q_{dl} for the double layer capacitance, and a Warburg impedance element. Using this equivalent circuit, both the impedance and the phase angle data were simulated very well. The simulation results are summarized in Table 4.1. As shown in the table, the solution resistance R_s is very similar at the pH of 7 and 5. However, the R_{ct} of the redox reaction at the pH of 7 is almost 100 times larger than that at the pH of 5. This suggests that the precursor layer surface at the pH of 7 is negatively charged, whereas the surface at the pH of 5 is positively charged. In addition, the double-layer capacitance at the pH of 5 is 8.1 μF, two times larger than that at the pH of 7, which is around 3.8 μF. This indicates that the diffusion layer of the redox ions on the electrode surface at a pH of 7 is thicker than that at the pH of 5, as illustrated schematically in Figure 4.1.

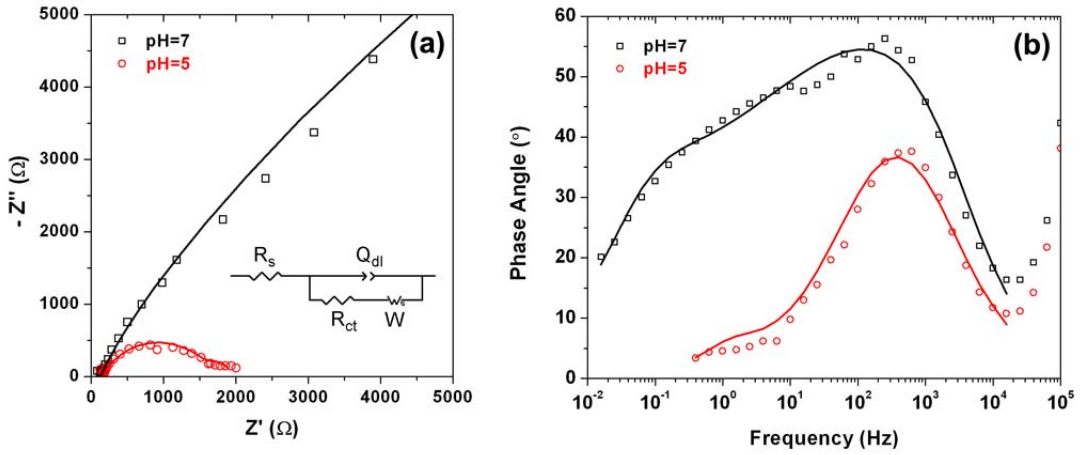

Figure 4.2 (a) The Nyquist impedance plot and (b) the Bode plot of phase angle for the EIS measurement in the presence of 5 mM $[Fe(CN)_6]^{3-/4-}$ at the pH of 5 and 7. The electrochemical results are simulated using the equivalent circuit shown in the inset of (a).[148]

Table 4.1 The simulation results of the EIS measurement on precursor layer at the pH of 5 and 7 .[148]

pH	R_s (Ω)	R_{ct} (kΩ)	Q_{dl} (CPE-T) [a] (μF)	Q_{dl} (CPE-P) [a]
7	130	~121	3.8	0.76
5	160	~1.5	8.1	0.72

[a] The double layer capacitance is simulated with a CPE element.[147] This element is essentially an imperfect capacitance, and it is composed of two components CPE-T and CPE-P. The CPE-T represents the capacitance value, and it is used to evaluate the redox ion diffusion. The CPE-P is a constant that ranges from 0 to 1, and a value close to 1 indicates the CPE element is close to an ideal capacitor.

4.3.2. Assembly of $[ITO/PSS(6.5)]_{9.5}$ on the Precursor Layer $[PEI(8.5)/PSS(6.5)]_4$

The assembly of the $[ITO/PSS(6.5)]_{9.5}$ thin films on the precursor layer of $[PEI(8.5)/PSS(6.5)]_4$ was studied using QCM. Three ITO suspensions at different pH, ITO(2.9), ITO(4), and PEI-ITO(7), were used for studying the precursor layer effect on the assembly of $[ITO/PSS(6.5)]_{9.5}$ films. As shown in Figure 4.3(a), the frequency change, $-\Delta f$, during the buildup of the precursor layer is quite similar for all three films. However, the assembly processes of $[ITO/PSS(6.5)]_{9.5}$ using the different ITO suspensions are vastly different. In order to reveal the assembly process in more detail, one needs to present the frequency change of each assembly step, the $\Delta(-\Delta f)$. According to Figure 4.3(a), the increase of $-\Delta f$ is mainly contributed by the ITO assembly step. Therefore, only the $\Delta(-\Delta f)$ of ITO assembly steps will be presented for the rest of the QCM results.

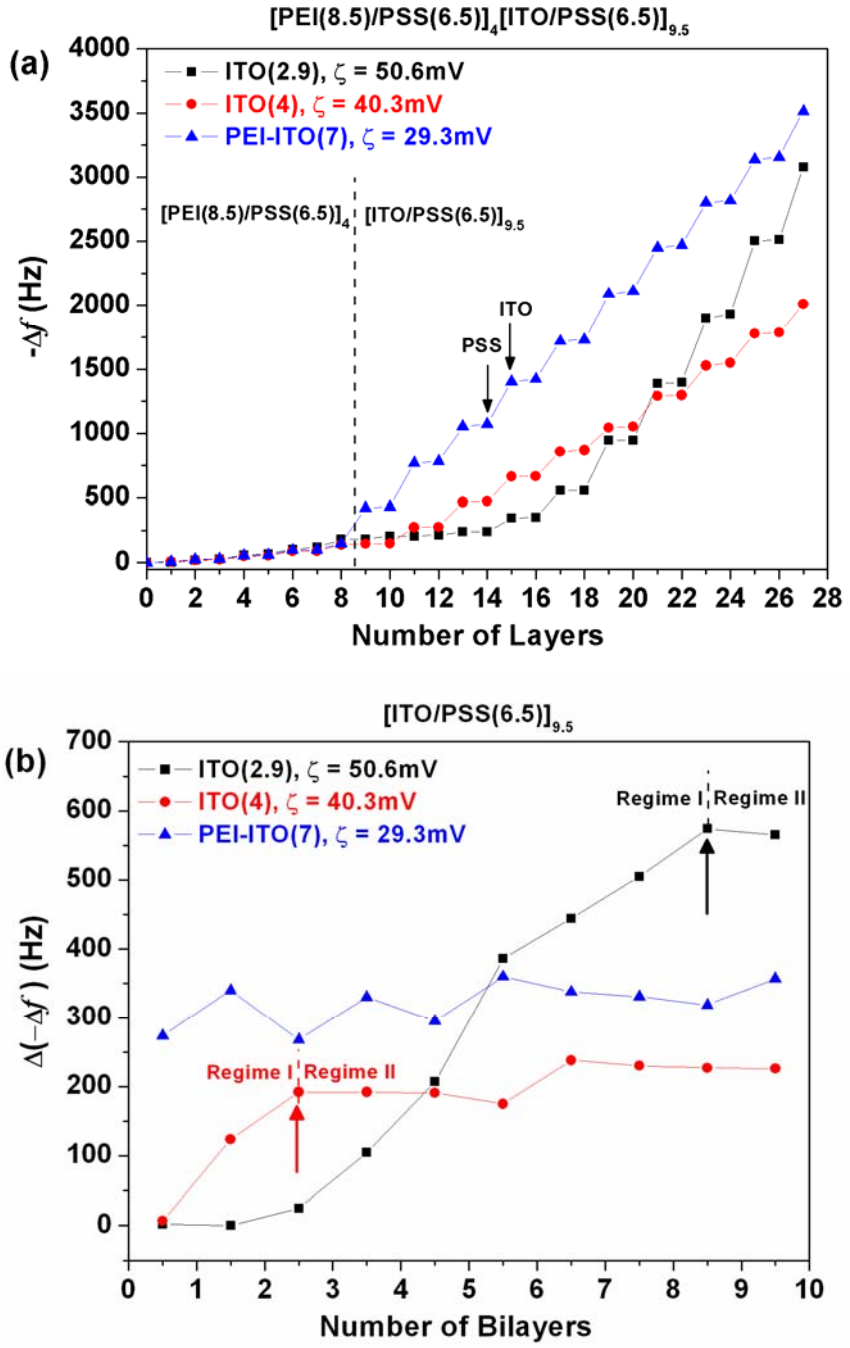

Figure 4.3 The QCM results during the assembly of $[ITO/PSS(6.5)]_{9.5}$ on the precursor layer $[PEI(8.5)/PSS(6.5)]_4$ using ITO(2.9), ITO(4), and PEI-ITO(7) suspensions: (a) the $-\Delta f$ of the whole LbL assembly process, and (b) the $\Delta(-\Delta f)$ of every ITO assembly steps. The transition points between the first regime and the second regime are indicated by the arrows in (b).[148]

As shown in Figure 4.3(b), the assembly process of ITO(2.9) and ITO(4) can be divided into two regimes. In the first regime, the $\Delta(-\Delta f)$ increases with an increasing number of assembly bilayers, and the $\Delta(-\Delta f)$ reaches a relatively constant value in the second regime. The first regime is called the "recovery regime", which will be explained later. The second regime is called the "linear growth regime", in which the thin film grows linearly. The assembly step at which the assembly process transfers from the first to the second regime is called the "transition point". As shown in Figure 4.3(b), this transition point occurs at the 9th ITO layer during the assembly of ITO(2.9) solutions, whereas this transition occurred at the 3rd ITO layer during the assembly of ITO(4) solutions. Interestingly, the buildup of $[PEI\text{-}ITO(7)/PSS(6.5)]_{9.5}$ only exhibits one regime, the "linear growth regime". The LbL assembly conditions and the LbL assembly process of all of the films are summarized in Table 4.2.

Table 4.2 Summary of the composition, the assembly conditions, and the thin film growth process of the LbL assembled ITO-PSS thin films.[148]

Precursor layer	Hybrid films $[ITO/PSS]_n$	NaCl concentration during the Assembly of $[ITO/PSS]_{9.5}$	The number of assembly steps for "recovery regime"/"linear growth regime"	Average $\Delta(-\Delta f)$ during the "linear growth regime"
$[PEI(8.5)/PSS(6.5)]_4$	$[ITO(2.9)/PSS(6.5)]_{9.5}$	0.1 M	9 / 1	570 Hz
$[PEI(8.5)/PSS(6.5)]_4$	$[ITO(2.9)/PSS(6.5)]_{9.5}$	0	10 / 0	–
$[PEI(8.5)/PSS(6.5)]_4$	$[ITO(4)/PSS(6.5)]_{9.5}$	0.1 M	3 / 7	209 Hz
$[PEI(8.5)/PSS(6.5)]_4$	$[PEI\text{-}ITO(7)/PSS(6.5)]_{9.5}$	0.1 M	10 / 0	321 Hz
$[PEI(8.5)/PSS(6.5)]_4$	$[PEI\text{-}ITO(7)/PSS(6.5)]_{9.5}$	0	10 / 0	157 Hz [a]
$[PEI(2.9)/PSS(2.9)]_4$	$[ITO(2.9)/PSS(2.9)]_{9.5}$	0.1 M	10 / 0	582 Hz
$[PEI(2.9)/PSS(2.9)]_4$	$[ITO(2.9)/PSS(2.9)]_{9.5}$	0	10 / 0	597 Hz

[a] The average $\Delta(-\Delta f)$ during the "linear growth regime" for film $[PEI\text{-}ITO(7)/PSS(6.5)]_{9.5}$ when PSS was assembled in a solution without NaCl was taken from the last 9 PEI-ITO layers.

The LbL assembly process was also observed by AFM imaging. As shown in Figure 4.4, the film buildup process for $[ITO/PSS(6.5)]_{9.5}$ on the precursor layer $[PEI(8.5)/PSS(6.5)]_4$ using the different ITO suspensions is vastly different. Prior to the 5^{th} ITO layer, the buildup rate of the thin film is obviously much faster for the ITO suspension at the higher pH. As shown in Figure 4.4(a), during the assembly of ITO(2.9), only a few relatively large agglomerates were deposited onto the surface after the first ITO layer, and the deposited particles could not cover the whole surface even after the fifth ITO layer. On the other hand, during the assembly of ITO(4), no large agglomerates were observed on the surface after the first ITO layer, but many more small ITO particles were observed. The film coverage of the substrate surface, prior to the fifth ITO layer during the assembly of ITO(4), is much higher than that during the assembly of ITO(2.9). Furthermore, during the assembly of PEI-ITO(7), the film buildup rate prior to the fifth ITO layer is even faster, and five ITO layers are sufficient to fully cover the substrate surface. The buildup of the film $[PEI\text{-}ITO(7)/PSS(6.5)]_{4.5}$ started with an island-like structure after the first ITO layer, and it finally developed to a uniform film after the fifth ITO layer.

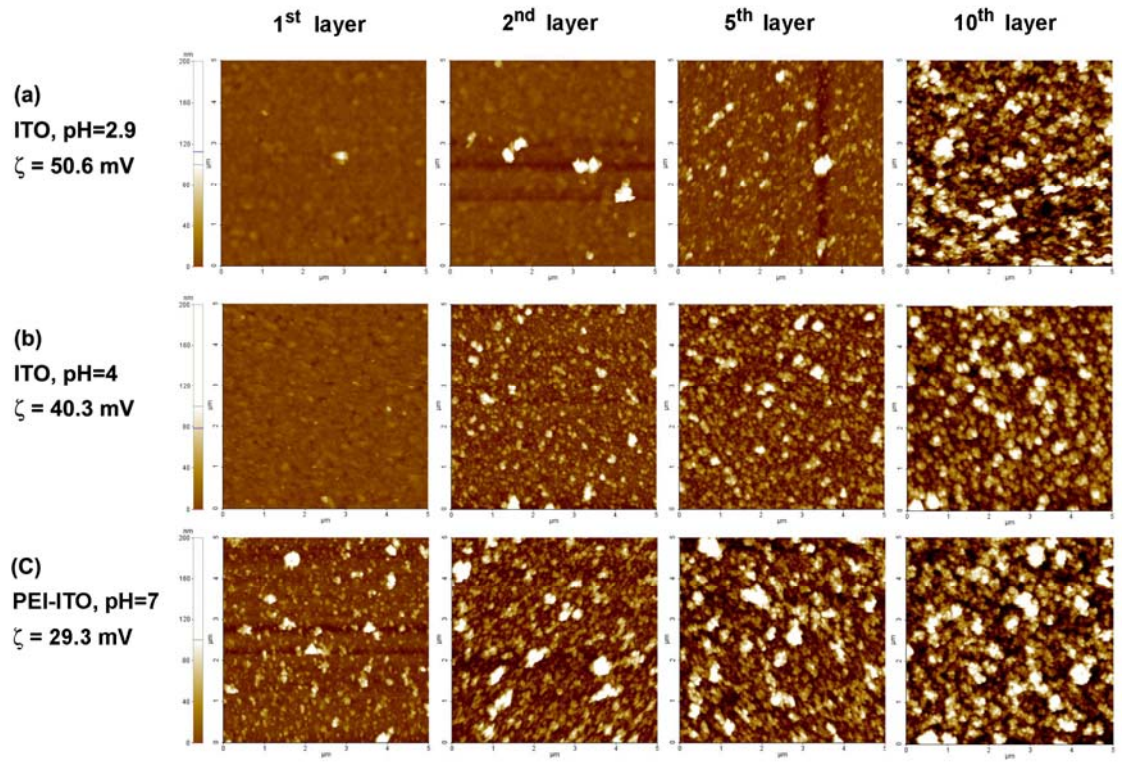

Figure 4.4 The AFM images of LbL films after the 1st, 3rd, 5th, and 10th layers of ITO when the (a) ITO(2.9), (b) ITO(4), or (c) PEI-ITO(7) solutions were used for the LbL assembly. All of the AFM images were acquired using the same scanning scale of 5×5 μm and the same height scale.[148]

4.3.3. Explanation of the Precursor-layer Controlled Nanoparticle Assembly

The effect of the precursor layer $[PEI(8.5)/PSS(6.5)]_4$ on the assembly of $[ITO/PSS]_{9.5}$ can be explained by the different surface charge of the precursor layer. As suggested by the electrochemical results, the precursor layer surface is negatively charged when the pH of ITO suspensions is above 6.5, whereas this surface is positively charged when the pH of ITO suspensions is below 6.5. Furthermore, this positive surface charge density is dependent on the pH of ITO suspensions. The lower the pH of the ITO suspensions, the higher the positive surface charge due to the increased charged density of every PEI chain. Therefore, the film buildup process is significantly dependent on the pH of the ITO suspensions. As illustrated in Figure 4.5(a), during the assembly of

ITO(2.9) and ITO(4), the positively charged ITO nanoparticles cannot easily deposit onto the positively charged precursor layer due to the repelling electrostatic forces. This is why only few agglomerate particles were observed on the substrate after the first ITO(2.9) layer (Figure 4.4(a)). On the other hand, during the assembly of ITO(4), the surface positive charge is not as high as that at the pH of 2.9, so the amount of ITO nanoparticles deposited on the substrate after the first ITO layer was increased (Figure 4.4(b)).

Because all of the PSS layers during the assembly of $[PEI/PSS]_4[ITO/PSS]_{9.5}$ were deposited at the pH of 6.5, a few more PSS layers were needed after the first ITO layer to compensate for the positive surface charges that were developed when the ITO was first deposited using either the ITO(4) or the ITO(2.9) solution. This is why the first regime of the assembly process, where the $\Delta(-\Delta f)$ increases with the number of assembly bilayers, is named the "recovery regime". Depending on the pH of the ITO suspension, the number of PSS layers needed to compensate for the positive surface charge and to recover the negative surface charge is different. If the ITO is assembled in the ITO(2.9) solution, more PSS assembly steps will be needed to recover the highly positively charged precursor layer surface. This is why the "recovery regime" during the assembly of ITO(2.9) required more assembly steps than that during the assembly of ITO(4) (Figure 4.3 and Table 4.2). Furthermore, during the assembly of PEI-ITO(7), the precursor layer is negatively charged due to the unchanged positive charge of PEI chains. As a result, almost no extra positive charges in the precursor layer need to be compensated, and only the "linear growth regime" was observed (Figure 4.3 and Table 4.2).

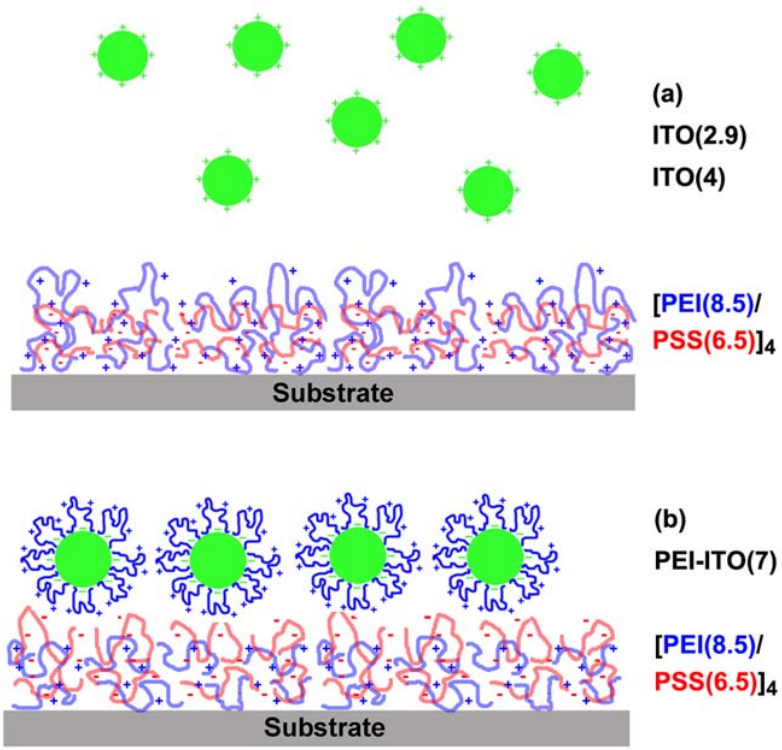

Figure 4.5 Schematics of the assembly process of the first ITO layer on the precursor layer $[PEI(8.5)/PSS(6.5)]_4$ using different ITO suspensions. (a) During the assembly of ITO(2.9) and ITO(4), the precursor layer is positively charged, and the positively charged ITO cannot easily deposit onto the surface due to the repelling electrostatic forces; (b) during the assembly of PEI-ITO(7), the precursor layer is negatively charged, and the positively charged PEI-ITO can easily deposit onto the surface due to the attractive forces.[148]

Unlike the thin film growth in the "recovery regime," the film buildup rate in the "linear growth regime" is not related to the surface charge of the precursor layer. Instead, it is related to the particle-surface interaction forces.[91, 118, 150] When the unmodified ITO is used for the nanoparticle assembly, the particle-surface interaction force is mainly contributed by the electrostatic forces between the particles and the substrate surface. This electrostatic force is directly proportional to the ITO particle surface charge, which can be characterized by the ζ-potential of the ITO suspensions. As mentioned in the legend of Figure 4.3, the ζ-potentials of the ITO(2.9) and ITO(4) suspensions are 50.6 and 40.3 mV, respectively. Due to the stronger particle-surface

electrostatic interaction force at the pH of 2.9, the $\Delta(-\Delta f)$ in the "linear growth regime" during the assembly of ITO(2.9), which is around 570 Hz/step, is almost three times that during the assembly of ITO(4), which is around 209 Hz/step (Table 4.2). Interestingly, even though the ζ-potential of PEI-ITO(7) is 29.3 mV, lower than that of ITO(4), the $\Delta(-\Delta f)$ in the "linear growth regime" of PEI-ITO(7), which is around 321 Hz/step, is significantly higher than that during the assembly of ITO(4). This unusual phenomenon can be attributed to the stronger particle-surface interaction forces between the PEI-ITO(7) and the negatively charged surface than that between the ITO(4) and the negatively charged surface, due to the larger number of interaction sites and the stronger polymer chain entanglement between the PEI-ITO and the PSS layers.[118]

4.3.4. The Effect of Ionic Strength in the PSS Solution

During the LbL assembly of polyelectrolytes and inorganic nanoparticles, the ionic strength in the polyelectrolyte solution usually plays a very significant role on the assembly process.[92, 94] A high ionic strength in the polyelectrolyte solution is usually preferred in order to increase the assembly rate of nanoparticles. Therefore, the effect of the ionic strength in the PSS solution on the ITO nanoparticles assembly was studied in this work. In order to evaluate the effect of the ionic strength in the PSS solution on the assembly of $[ITO/PSS]_{9.5}$, only the ionic strength in the PSS solution for the assembly of $[ITO/PSS]_{9.5}$ was changed whereas that in the assembly of $[PEI/PSS]_4$ was unchanged as 0.1 M.

As shown in Figure 4.6, during the assembly of $[PEI(8.5)/PSS(6.5)]_4[ITO(2.9)/PSS(6.5)]_{9.5}$, the ionic strength in the PSS solution significantly affected the assembly rate of the $[ITO(2.9)/PSS(6.5)]_{9.5}$ thin film. When 0.1M NaCl was added into the PSS solution, the two-regime assembly process was observed, and the $\Delta(-\Delta f)$ reached 570 Hz/step in the "linear growth regime". However, when no NaCl was added into the PSS solution, the assembly process did not reach the

"linear growth regime" within the 10 ITO layers examined, and the $\Delta(-\Delta f)$ of every ITO step was well below 100 Hz/step. The significant difference between these two assembled films can be attributed to the difference in the rate of compensation of the positive surface charges by PSS. At a higher ionic strength, the amount of PSS deposited during each step is increased due to the salt screening on the polymer charges.[75] Therefore, fewer PSS assembly steps were needed to recover the negative surface charge at a high ionic strength, and the assembly of $[ITO/PSS]_{9.5}$ can more easily reach the "linear growth regime".

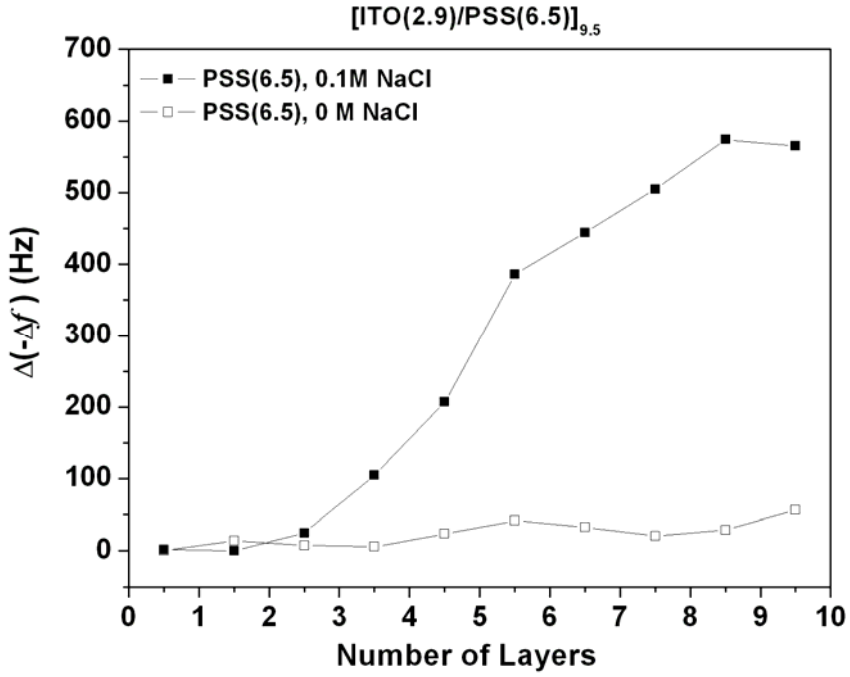

Figure 4.6 The $\Delta(-\Delta f)$ of ITO assembly steps during the assembly of $[ITO(2.9)/PSS(6.5)]_{9.5}$ on the precursor layer $[PEI(8.5)/PSS(6.5)]_4$, when 0.1 M NaCl or no NaCl was added into the PSS solutions.[148]

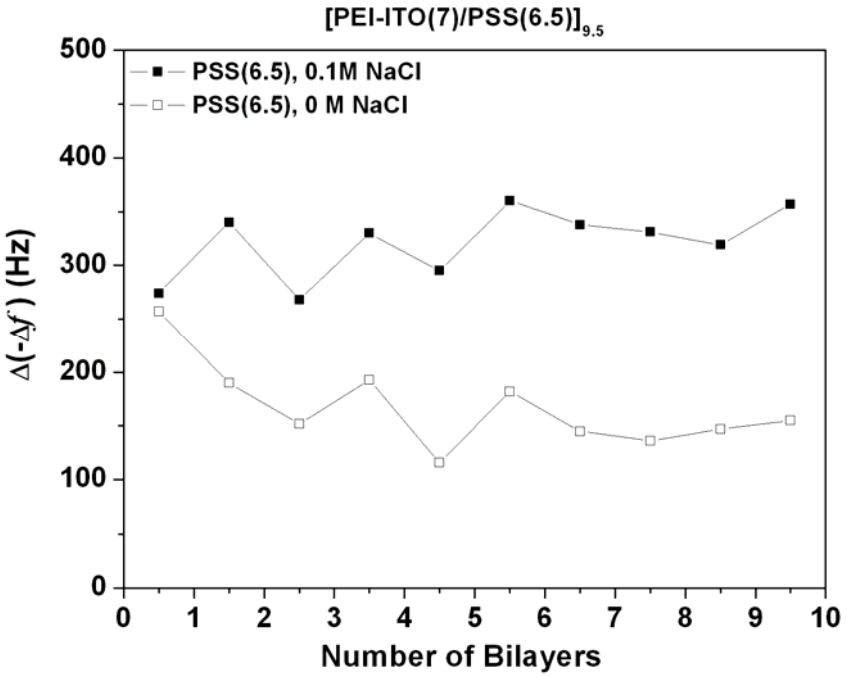

Figure 4.7 The Δ(−Δ*f*) of ITO assembly steps during the assembly of [PEI-ITO(7.2)/PSS(6.5)]$_{9.5}$ on the precursor layer [PEI(8.5)/PSS(6.5)]$_4$, when 0.1 M NaCl or no NaCl was added into the PSS solutions.[148]

The ionic strength in the PSS solution also played a significant role during the assembly of [PEI(8.5)/PSS(6.5)]$_4$[PEI-ITO(7)/PSS(6.5)]$_{9.5}$. As shown in Figure 4.7 and Table 4.2, the Δ(−Δ*f*) of the ITO assembly steps remained around 320 Hz/step when the NaCl concentration in the PSS solution was 0.1M. However, when no NaCl was added into the PSS solution, the Δ(−Δ*f*) of the ITO assembly steps dropped to ~160 Hz/step after the first ITO layer. This drastic change by as much as half of the Δ(−Δ*f*) during the assembly of PEI-ITO(7) can be attributed to the degree of overcompensation of the surface charge by PSS at the different ionic strength. The excess amount of negative surface charge due to the overcompensation of surface charge by PSS assembly at a high ionic strength is much higher than that at a low ionic strength.[75] Therefore, the amount of PEI-ITO(7) needed to overcompensate this excess negative surface charge is increased when the PSS is assembled at a high ionic strength. It is to be noted that the ionic strength

effect on the assembly of [PEI-ITO(7)/PSS(6.5)]$_{9.5}$ is similar to the ionic strength effect on the assembly of PEM.[75] This is reasonable, since the ITO nanoparticles in the PEI-ITO suspensions were modified by the PEI polyelectrolyte on the surface, and the interaction between the PSS and the PEI-ITO is somewhat like the interaction between two polyelectrolytes.

4.3.5. Assembly of [ITO(2.9)/PSS(2.9)]$_{9.5}$ on Precursor Layer [PEI(2.9)/PSS(2.9)]$_4$

In order to prove the hypothesis that the precursor layer controls the "recovery regime" of the LbL assembly process, another film [ITO(2.9)/PSS(2.9)]$_{9.5}$ on the precursor layer [PEI(2.9)/PSS(2.9)]$_4$ was assembled In this case, all of the materials, including the PEI, PSS, and ITO, were assembled at the exact same pH of 2.9. As a result, the surface charge of the precursor layer is not expected to change during the LbL assembly process. As shown in Figure 4.8, only a "linear growth regime" was observed for the assembly of [ITO(2.9)/PSS(2.9)]$_{9.5}$ onto [PEI(2.9)/PSS(2.9)]$_4$, regardless of the different ionic strength in the PSS solutions. In fact, as shown in Table 4.2, the average $\Delta(-\Delta f)$ of the ITO assembly step was around 582 and 597 Hz/step when the 0.1 M NaCl or no NaCl were added into the PSS solutions, respectively. This value is very close to that obtained in the "linear growth regime" during the assembly of [ITO(2.9)/PSS(6.5)]$_{9.5}$ on [PEI(8.5)/PSS(6.5)]$_4$. In other words, the precursor layer only affected the first regime of the surface charge recovery, but it does not affect the film buildup rate during the "linear growth regime".

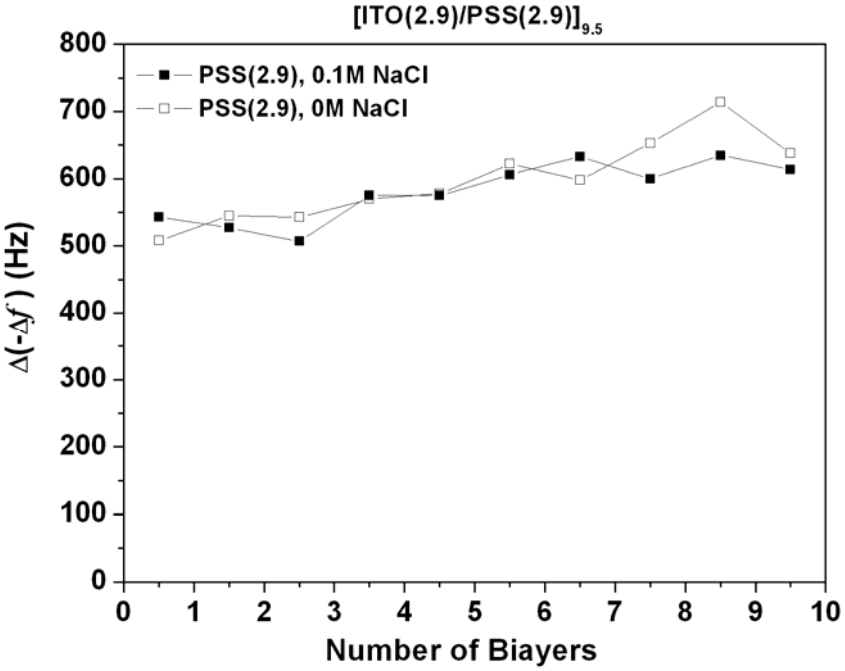

Figure 4.8 The $\Delta(-\Delta f)$ of ITO assembly steps during the assembly of $[ITO(2.9)/PSS(2.9)]_{9.5}$ on the precursor layer $[PEI(2.9)/PSS(2.9)]_4$, when 0.1 M NaCl or no NaCl was added into the PSS solutions.[148]

4.3.6. Explanation of the Different Ionic Strength Effect

The different effect of ionic strength in the PSS solutions during the assembly of $[PEI\text{-}ITO(7)/PSS(6.5)]_{9.5}$ on the precursor layer $[PEI(8.5)/PSS(6.5)]_4$ and the assembly of $[ITO(2.9)/PSS(2.9)]_{9.5}$ on the precursor layer $[PEI(2.9)/PSS(2.9)]_4$ can be attributed to the different interaction between the ITO layer and the PSS layer during these two assembly processes. As illustrated in Figure 4.9(a), when the PEI-ITO(7) was used for the assembly of ITO, the interaction forces between the PEI-ITO(7) and the PSS(6.5) is not only the electrostatic forces, but also the polymer-polymer interactions. Similar to the LbL assembly of PEMs,[73, 75, 78] the ionic strength in the polyelectrolyte solutions can significantly affect the film buildup rate. As illustrated in Figure 4.9(a), at high ionic strength, the adsorbed PSS layer forms a loopy structure, rendering a stronger particle-surface interaction force between the PEI-ITO(7) and PSS(6.5) layers. On the

other hand, as shown in Figure 4.9(b), the interaction force between the ITO(2.9) and PSS(2.9) layer is primarily electrostatic forces, and thus the conformation of adsorbed PSS chains did not affect significantly the assembly rate of ITO(2.9).

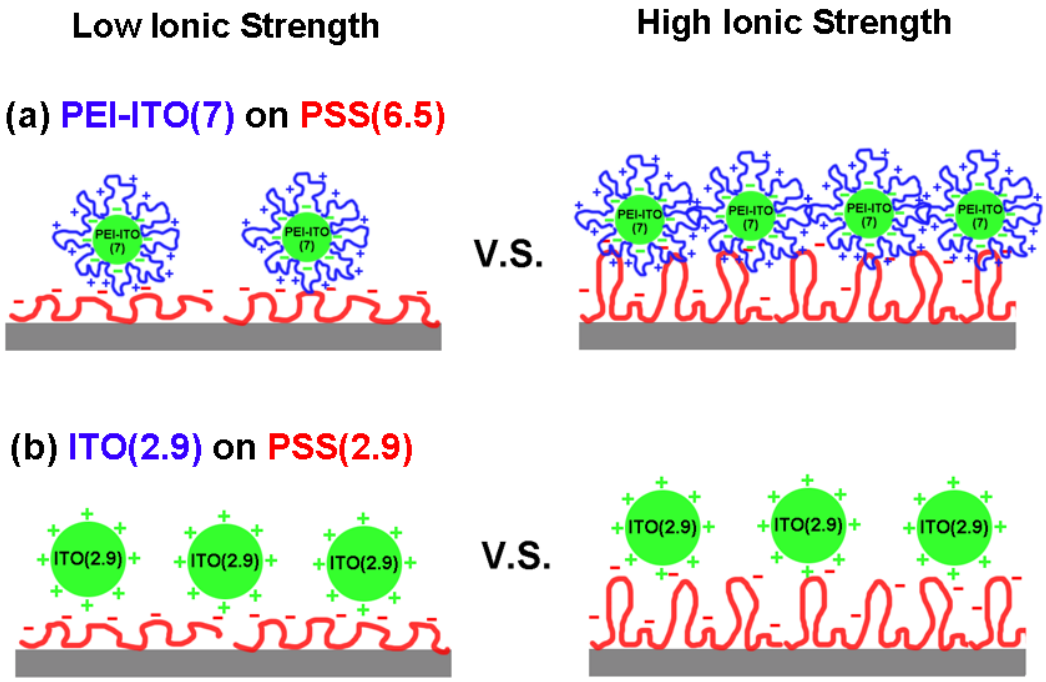

Figure 4.9 Schematics of the effect of the ionic strength in the PSS solution on the assembly of ITO on PSS layer: (a) the assembly of PEI-ITO(7) on PSS(6.5), and (b) the assembly of ITO(2.9) on PSS(2.9).

4.4. Conclusions

This chapter presents results on a study on the effect of the precursor layer $[PEI/PSS]_4$ on the subsequent LbL assembly of $[ITO/PSS]_{9.5}$ hybrid films. It was found that the surface charge of the precursor layer is dependent on the pH value of the ITO suspension used. A higher pH value in the ITO suspension than that in the PSS solution will maintain the negative surface charge of the precursor layer. On the other hand, a lower pH value in the ITO suspension than that of the PSS solution will make the precursor layer have a positive surface charge due to the excessive positive charges that were gained by PEI chains at low pH.

The surface charge of the precursor layer significantly affected the assembly of $[ITO/PSS]_{9.5}$ films. When the precursor layer surface is positively charged during the assembly of ITO nanoparticles, which is also positively charged, the assembly process can be divided into two regimes: the “recovery regime” in which the positive surface charge will be compensated by PSS and recovered to a negative surface, followed by the “linear growth regime”. The length of the “recovery regime” is dependent on the amount of positive surface charges that need to be compensated for and the ionic strength in the PSS solution. When the precursor layer surface is negatively charged during the assembly of ITO nanoparticles, only the “linear growth regime” was observed.

When the unmodified ITO suspension was used for the LbL assembly, the ionic strength in the PSS solutions only affected the length of the “recovery regime”, but it did not affect the film buildup rate for the “linear growth regime”. However, when the PEI-modified ITO suspension was used, the film buildup rate in the “linear growth regime” was significantly affected by the ionic strength in the PSS solution. A high ionic strength in the PSS solution will promote faster deposition of PEI-modified ITO nanoparticles, due to the strong ionic strength effect on the interaction between the PEI-ITO and PSS layers.

CHAPTER 5

PH-CONTROLLED EXPONENTIAL LAYER-BY-LAYER ASSEMBLY OF BICOMPONENT POLYELECTROLYTE / NANOPARTICLE MULTILAYERS

5.1. Introduction

Up to now, most of the *e*-LbL growth has been observed in polymeric or organic systems. There have been a few studies that demonstrated the *e*-LbL growth of hybrid thin films.[11, 116, 117, 121, 151] However, these films were either primarily composed of organic materials, or they were composed of more than two components. There has yet been no report on achieving a bicomponent *e*-LbL films that consist mostly of inorganic nanoparticles. Such films would be highly desirable for applications that require excellent nanoparticle interconnections or where the functionality desired depends primarily on the inorganic nanoparticle properties. Examples of applications that would require these types of films include the optimization of the electrical conductivity of nanotube, graphene or ITO solution-based films for electromagnetic interference (EMI) shielding, ultracapacitor energy storage applications or as transparent electrodes. Other desired multifunctional films would be conformal protective coatings for applications that require high resistance to indentation loading or fracture resistance.

This chapter focuses on the assembly of organic/inorganic bicomponent composite films through the *e*-LbL method. In this chapter, the *e*-LbL growth of $[PEI/SiO_2]_n$ bicomponent thin films that consist mostly of SiO_2 nanoparticles (over 90 wt% obtained by TGA) is prepared by assembly the PEI at a high pH and the SiO_2 at a low pH. The $[PEI/SiO_2]_n$ films that prepared through *e*-LbL growth can grow to thicknesses over 2 μm within just 10 bilayers, whereas the films that prepared through the

l-LbL growth are less than 200 nm with 10 bilayers. Besides the $[PEI/SiO_2]_n$ films, the $[PAA/PEI\text{-}ITO]_n$ hybrid thin films also shows a weak *e*-LbL growth process when the thin films is prepared with less drying steps.

5.2. Experimental Procedure

This chapter reports results mainly about the *e*-LbL assembly of $[PEI/SiO_2]_n$ films and the LbL assembly of $[PAA/ITO]_n$ films. PEI was chosen as the polycation due to its proven diffusibility during the LbL assembly process[109, 116] and its charge density variability over the pH range from 2 to 10.[122, 134] Colloidal SiO_2 nanoparticles were chosen as the negatively charged inorganic material due to its low IEP point. In order to evaluate the possibility to prepare the conductive *e*-LbL thin film, the weak polyelectrolyte PAA was used as the polyanion to explore the possibility to prepare *e*-LbL $[PAA/ITO]_n$ films.

The colloidal SiO_2 suspension (LUDOX® AS-40) was obtained from Sigma Aldrich, and it was analyzed using zetasizer to obtain the ζ-potential and particle size distribution. The LbL assembly process of $[PEI/SiO_2]_n$ films was studied by using a QCM, AFM, and SEM. The experimental procedure of zetasizer, QCM, and AFM is very similar to the procedure that was described in Chapter 2, except that no precursor layer was assembled prior to the deposition of the $[PEI/SiO_2]_n$ films. SEM was used to evaluate the film thickness of $[PEI/SiO_2]_{50}$ grown on glass substrate.

5.2.1. Thin Film Growth on Different Substrates

In this Chapter, hybrid thin films were prepared onto various substrates, including QCM crystals, silicon wafers, and glass slides. The thin film deposition on QCM crystals are similar to the procedure described in Chapter 2. In brief, the QCM crystals were modified by a SAM layer of MUA, and the SAM-modified QCM crystals were then used for the LbL assembly. Unlike the LbL assembly on QCM crystals, no SAM modification

was applied on the silicon wafers prior to the LbL assembly. The silicon wafers were just cleaned by acetone and isopropanol, and the cleaned silicon wafers were used for the LbL assembly. Similar to the silicon wafer, the glass slides were also just cleaned by organic solvent prior to the LbL assembly without any SAM modification.

5.2.2. Neutron Reflectometry

The thickness and structure of the films that were deposited onto silicon wafers were evaluated using neutron reflectometry (Magnetism Reflectomer, Spallation Neutron Source at Oak Ridge National Labs). Neutron Reflectometry is an excellent method for determining the thickness, composition and arrangement of films, interfaces and multilayers. The Magnetism Reflectometer at the Spallation Neutron Source can be configured for unpolarized and polarized beams to measure non-magnetic and magnetic systems, respectively. This is a time-of-flight (TOF) instrument with wavelength band ranging from 2 Å to 4.75 Å centered at the highest intensity of the incident beam.[152] The essence of a neutron reflection experiment is that it measures the specular reflection as a function of momentum transfer perpendicular to the reflecting surface. To cover a wide range of momentum transfers using the restricted wavelength band, the reflected intensities are measured at several incident angles.

The experiment is performed in grazing incidence geometry. A highly collimated neutron beam impinges on the sample surface at an angle α_i , and the intensity of the neutrons, reflected and scattered under angles α_f, is registered using a position sensitive detector as the function of their time-of-flight from the source. For the specular reflection, $\alpha_i = \alpha_f$, the reflectivity is given as a function of the momentum transfer Q_z normal to the surface, $Q_z = 2\pi * \sin(\alpha_i)/\lambda$, where λ is the wavelength. The specular reflection of neutrons gives information on the scattering length density profile and hence provides important information about the depth composition of films, multilayers and interfaces. More detailed specifications of the instrument can be found in the instrument's web site.[153]

5.2.3. Thermogravimetric Analysis of Thin Films

The composition of thin film $[PEI(9.9)/SiO_2(4.7)]_{50}$ and the thin film [PEI(9.9, 3mM buffer)/SiO_2(4.7, 3mM buffer)]$_{50}$ were analyzed using TGA. The thin film samples were collected by scraping the thin film off from the glass substrates using blades, and the collected samples were heated to 800°C in air at a heating rate of 5°C/min. The remnant material was considered to be non-combustible inorganic SiO_2.

In order to evaluate the actual content that was contributed by the SiO_2 nanoparticles, which includes both the non-combustible SiO_2 and combustible stabilizing agents, a spin-coated film made from SiO_2 nanoparticles were analyzed by TGA using the same heating procedure. The colloidal SiO_2 particles were first spin-coated on a glass substrate, and the particles on the glass substrate were then collected by scraping off from the glass substrate for the TGA analysis.

5.3. Results and Discussion

5.3.1. ζ-potential and Particle Size of SiO_2 particles

The ζ-potential and the particle size of colloidal SiO_2 suspensions are shown in Figure 5.1. As shown in the figure, the SiO_2 particle size is essentially constant from the pH of 2 to 9.5. In addition, the ζ-Potential of the SiO_2 suspension is below -30mV at the pH from 4.5 to 9.5. Therefore, this SiO_2 suspension is very stable at the pH range from 4.5 to 9.5, and the surface charge is unchanged at this pH range. Therefore, the PEI and SiO_2 counter-ion pair provides a perfect opportunity to demonstrate the pH-promoted exponential growth of LbL thin films.

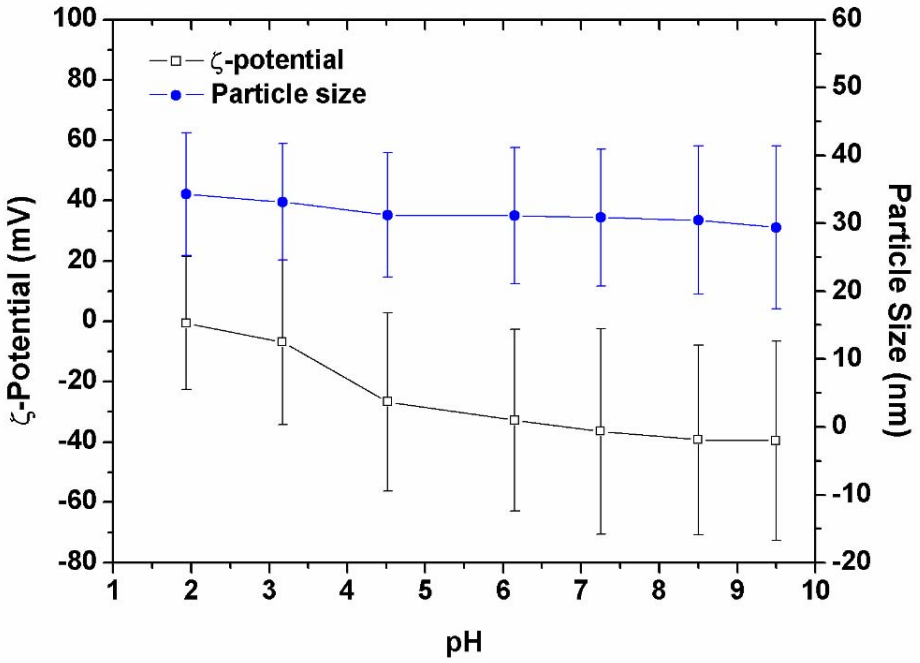

Figure 5.1 The ζ-Potential and particle size analysis of SiO_2 colloidal suspensions.[154]

5.3.2. pH Effect on the *e*-LbL Assembly

The LbL assembly of $[PEI/SiO_2]_n$ films was significantly affected by the pH difference between the PEI solutions and the SiO_2 suspensions. As shown in Figure 5.2, when PEI and SiO_2 were respectively assembled at the pH of 9.9 and 4.7 to prepare thin film $[PEI(9.9)/SiO_2(4.7)]_{10}$, the LbL assembly process exhibited extremely fast exponential growth in the first 3 bilayers, and then transferred to a linear growth with a fast growth rate. The growth rate in the exponential growth regime was so fast that more than 50 wt% of the 10-bilayer thin films is contributed by the first 3 assembly bilayers. However, when the thin film was deposited with PEI at a pH of 9.6 and SiO_2 at a pH of 6.5, the exponential growth rate of films was greatly diminished, although this process lasted until the 9th layer before the transition from exponential growth to linear growth occurred. Due to the depressed exponential growth, the thin film $[PEI(9.6)/SiO_2(6.5)]_{10}$ only exhibited less than half the thickness of film $[PEI(9.9)/SiO_2(4.7)]_{10}$ (Table 5.1). The

linear growth rate after the exponential-linear transition during the assembly of $[PEI(9.9)/SiO_2(4.7)]_{10}$ and $[PEI(9.6)/SiO_2(6.5)]_{10}$ was quite similar.

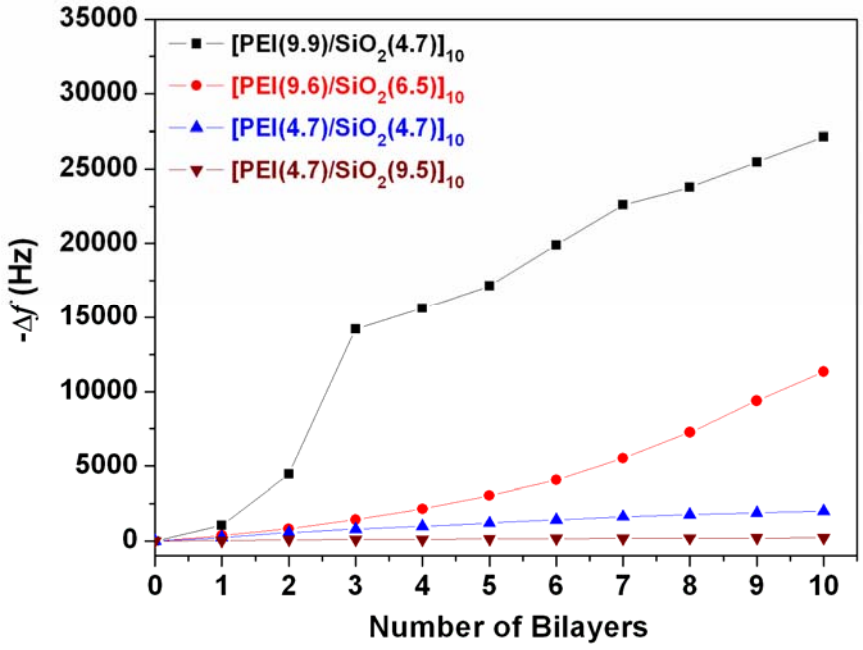

Figure 5.2 QCM crystal frequency change ($-\Delta f$) during LbL assembly of $[PEI(9.9)/SiO_2(4.7)]_{10}$, $[PEI(9.6)/SiO_2(6.5)]_{10}$, $[PEI(4.7)/SiO_2(4.7)]_{10}$, and $[PEI(4.7)/SiO_2(9.5)]_{10}$ thin films.[154]

When the thin film was assembled in PEI and SiO_2 solutions at the same pH of 4.7, the LbL assembly process exhibited a typical *l*-LbL growth with a much smaller growth rate. In fact, the linear growth rate of the $[PEI(4.7)/SiO_2(4.7)]_{10}$ film was 10 times slower than that of the linear growth regime during the *e*-LbL assembly processes (Table 5.1). When thin films were assembled in PEI at a pH of 4.7 and in SiO_2 at a pH of 9.5, only a minimal amount of material was deposited after 10 bilayers. Therefore, it can be concluded that the LbL assembly process will exhibit *e*-LbL growth when the thin film is assembled with PEI at a high pH and with SiO_2 at a low pH. When the pH difference between PEI and SiO_2 is small or when SiO_2 is at a high pH and PEI is at a low pH, the *e*-LbL growth will significantly diminish or disappear. The $[PEI(9.9)/SiO_2(4.7)]_{10}$ and

$[PEI(4.7)/SiO_2(4.7)]_{10}$ films showed 11 times difference in terms of the film mass and thickness.

5.3.3. Film Thickness Calculation

The thin film thickness can be evaluated by correlating the film thickness, *t*, with the resonance frequency change of QCM crystals, $-\Delta f$, through a constant C_f according to the Sauerbrey equation:[125]

$$t = C_f\left(-\Delta f\right) \tag{5.1}$$

in which C_f is related to the intrinsic resonance frequency, the density, and the shear modulus of quartz crystals as well as the density of films on the electrode surface (Chapter 2). For a quartz crystal with resonance frequency of 5 MHz and a fully dense SiO_2 thin film (density of bulk SiO_2 is 2.634 g/cm^3), the C_f should equal to 0.0335 nm/Hz if both sides of the crystal are coated with the film. However, the thickness of thin film $[PEI(9.6)/SiO_2(6.5)]_{10}$ was measured to be 896 nm by AFM (Figure 5.3). Therefore, the C_f should be 0.079 nm/Hz. This value was proven to be reasonable with other films, and it was used to calculate the film thickness from QCM results. This discrepancy of the calculated C_f value and the measured C_f value can be attributed to the porosity of the deposited thin film.

The thickness of the whole film, the thickness portion of the film that was exponentially grown, as well as the thickness portion of the thin film that was linearly grown, were all calculated using equation (5.1), and the results are listed in Table 5.1. As shown in the table, the film thickness of $[PEI(9.9)/SiO_2(4.7)]_{10}$ is 2143 nm, and the first 3 bilayers of exponential growth contributed 1123 nm, which is more than half the total thickness. In addition, the 3 bilayers of $[PEI(9.9)/SiO_2(4.7)]_{10}$ is almost 40 times that of the SiO_2 particle size (~30 nm). Based on the calculation, the film thickness of $[PEI(9.6)/SiO_2(6.5)]_{10}$, $[PEI(4.7)/SiO_2(4.7)]_{10}$, and $[PEI(4.7)/SiO_2(9.5)]_{10}$ are 896, 158 and 17 nm, respectively. The thickness of the $[PEI(4.7)/SiO_2(9.5)]_{10}$ thin film is even less

than one monolayer of SiO_2. This suggests that this thin film cannot fully cover the substrate surface even after 10 bilayers deposition.

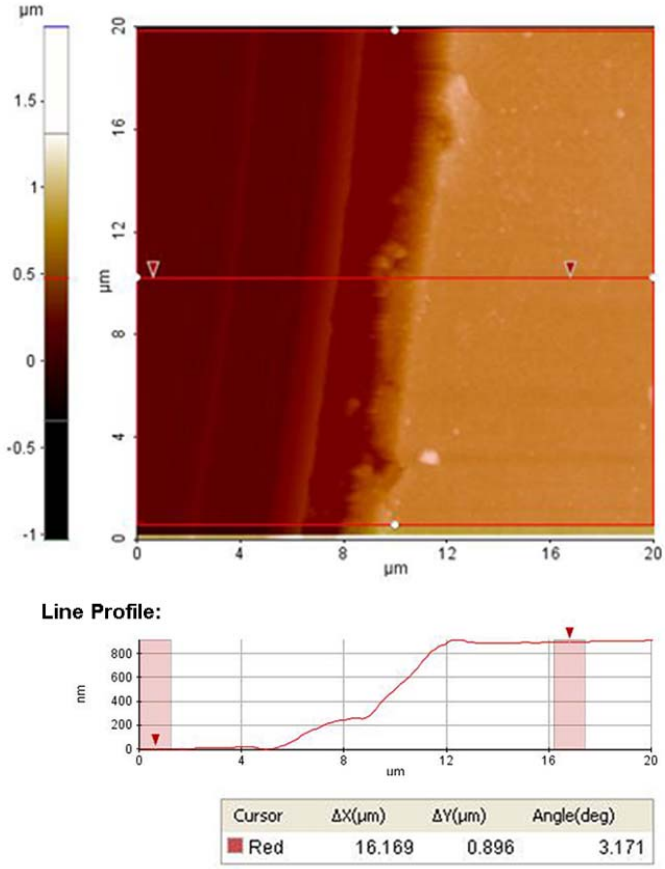

Figure 5.3 AFM film thickness measurement of the $[PEI(9.6)/SiO_2(6.5)]_{10}$ film. The thickness is evaluated by measuring the height from the top of the film to the substrate surface. The area within the red rectangular area is the area of interest, and multiple values are taken to get the average value. The average thickness was determined to be 896±8 nm.[154]

Table 5.1 Film thickness calculation from QCM results.[154]

Film [a]	$-\Delta f$ at the 10^{th} bilayer (Hz)	Total Thickness [b] (nm)	Thickness from *e*-LbL growth [b] (nm) / number of *e*-LbL growth steps [c]	Thickness from *l*-LbL growth [b] (nm) / number of *l*-LbL growth steps
$[PEI(9.9)/SiO_2(4.7)]_{10}$	27130	2143	1123 / 3	1020 / 7
$[PEI(9.6)/SiO_2(6.5)]_{10}$	11345	896	741 / 9	155 / 1
$[PEI(4.7)/SiO_2(4.7)]_{10}$	2000	158	0 / 0	158 / 10
$[PEI(4.7)/SiO_2(9.5)]_{10}$	212	17	0 / 0	17 / 10
[PEI(10.1, 0.1M NaCl)/SiO_2(4.7)]$_{10}$	8580	678	0 / 0	678 /10
[PEI(9.9, 3mM buffer)/ SiO_2(4.7, 3mM buffer)]$_{10}$	37972 [d]	3000	1344 / 5	1656 / 4

[a] In order to differentiate the films, the pH value, NaCl concentration, as well as the buffer concentration of PEI solutions and SiO_2 suspensions were chosen to be denoted in the parentheses. [b] The thickness values were all calculated from the $-\Delta f$ value using equation (5.1) with the C_f constant as 0.079 nm/Hz. [c] The number of *e*-LbL growth steps were determined by the $\Delta(-\Delta f)$ development through the LbL assembly process. An exponential-linear transition was determined when the $\Delta(-\Delta f)$ of one assembly step was equal or smaller than that of the previous step. [d] The $-\Delta f$ value of the thin film [PEI(9.9, 3mM buffer)/ SiO_2(4.7, 3mM buffer)]$_{10}$ was the value before the last SiO_2 layer. The $-\Delta f$ of the last SiO_2 layer cannot be measured because the film was insulating and it was too thick. As a result, the QCM measurement was not accurate.

5.3.4. Film Surface Structure

The surface structure of films was analyzed by AFM imaging. Regardless of the large film thickness difference between the *e*-LbL films and *l*-LbL films, the surface topography in 2 μm × 2 μm area for the *e*-LbL films, $[PEI(9.9)/SiO_2(4.7)]_{10}$ and $[PEI(9.6)/SiO_2(6.5)]_{10}$ in Figure 5.4(a) and (b), are very close in terms of the surface roughness. Therefore, the *e*-LbL growth is not due to the surface roughness. This phenomenon was also observed during the *e*-LbL growth of $[PEI(9.9)/SiO_2(4.7)]_n$ films, where *n* was varied from 1 to 4 while the surface roughness remained approximately the same (Figure 5.5). The $[PEI(4.7)/SiO_2(9.5)]_{10}$ thin film exhibited a very different film

structure, where the deposited nanoparticles formed cluster-like structures, and the thin film exhibited a patchy thin film growth behavior (Figure 5.4(d)).

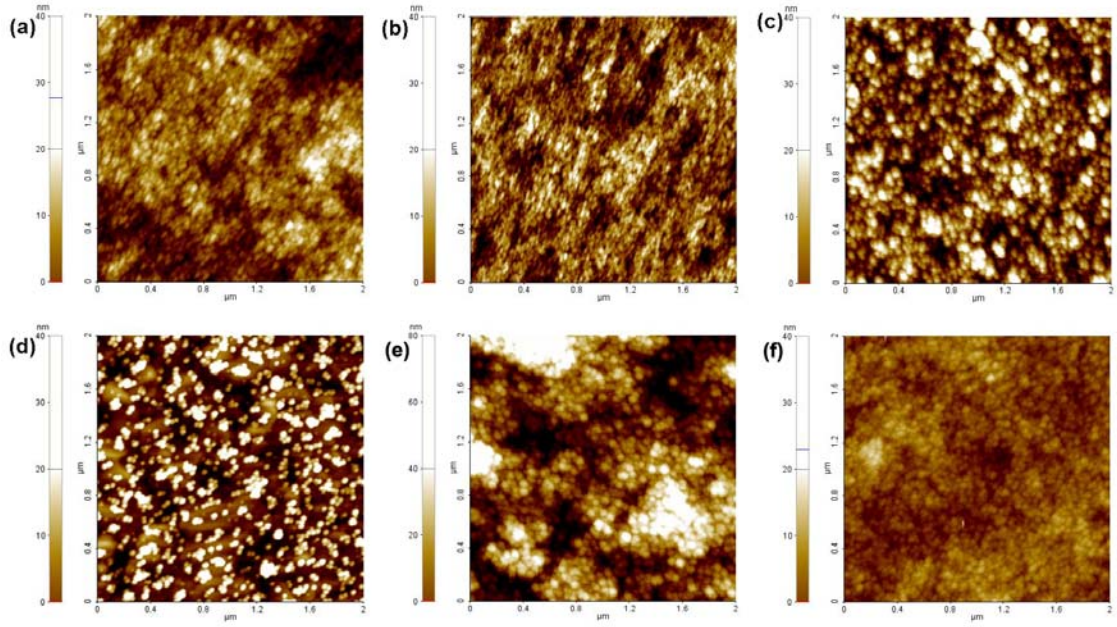

Figure 5.4 AFM images of films: (a) $[PEI(9.9)/SiO_2(4.7)]_{10}$, (b) $[PEI(9.6)/SiO_2(6.5)]_{10}$, (c) $[PEI(4.7)/SiO_2(4.7)]_{10}$, (d) $[PEI(4.7)/SiO_2(9.5)]_{10}$, (e) [PEI(10.1, 0.1M NaCl)/SiO_2(4.7)]$_{10}$, and (f) [PEI(9.9, 3mM buffer)/SiO_2(4.7, 3mM buffer)]$_{10}$. The RMS roughness of the 2 μm × 2 μm images is (a) 7.9, (b) 8.8, (c) 11.2, (d) 12.6, (e) 24.5, and (f) 4.2 nm, respectively. All of the figures are displayed with the same height scale, except for the figure (e) due to its high surface roughness.[154]

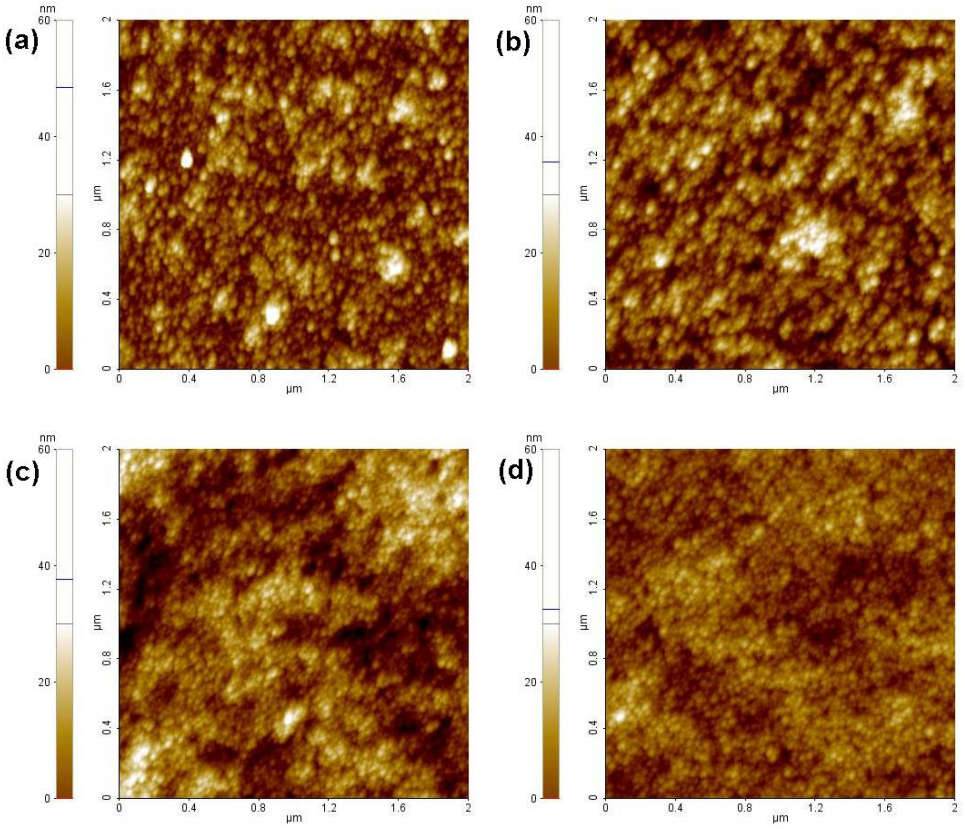

Figure 5.5 AFM images of $[PEI(9.9)/SiO_2(4.7)]_n$ when *n* equals to (a) 1, (b) 2, (c) 3, and (d) 4. The surface RMS roughness in the 2 μm × 2 μm area are (a) 8.7, (b) 9.4, (c) 10.2, and (d) 6.3 nm, respectively.[154]

The 3D profiles of the thin films were also analyzed by AFM. As shown in Figure 5.6(a) and (d), the *e*-LbL grown thin films $[PEI(9.9)/SiO_2(4.7)]_{10}$ and [PEI(9.9, 3mM buffer)/SiO_2(4.7, 3mM buffer)]$_{10}$ exhibited a wavy structure at the 30 μm × 30 μm scale, with a peak-to-valley height differences of around 100 and 200 nm, respectively. The surface RMS roughness of these two films at the 30 μm × 30 μm scale is 21 and 58 nm, respectively. However, as shown in Figure 5.4(a) and (f), these two films exhibited a rather smooth surface in the 2 μm × 2 μm scale, with a RMS roughness of 7.9 and 4.2 nm. It indicates that these two *e*-LbL films exhibited a two-scale structure. On the contrary, the $[PEI(9.6)/SiO_2(6.5)]_{10}$ and $[PEI(4.7)/SiO_2(4.7)]_{10}$ thin films did not show such a

two-scale structure (Figure 5.6(b) and (c)). The RMS surface roughness of these two films is all around 10 nm at both the 30 μm × 30 μm and the 2 μm × 2 μm scales. The unique two-scale structure of *e*-LbL thin films [PEI(9.9)/SiO_2(4.7)]$_{10}$ and [PEI(9.9, 3mM buffer)/SiO_2(4.7, 3mM buffer)]$_{10}$ is probably due to the PEI diffusion and the conformation change of PEI chains through the thin film. The diffusion "in-and-out" of the PEI chains and the conformation change of PEI chains from coiled to extended structure during every assembly step can introduce the non-uniform surface structure. The fact that the *e*-LbL film [PEI(9.6)/SiO_2(6.5)]$_{10}$ did not show such a structure is probably due to the relatively slow *e*-LbL growth, and thus the less diffusion and less conformation change of PEI chains for this film (Figure 5.2).

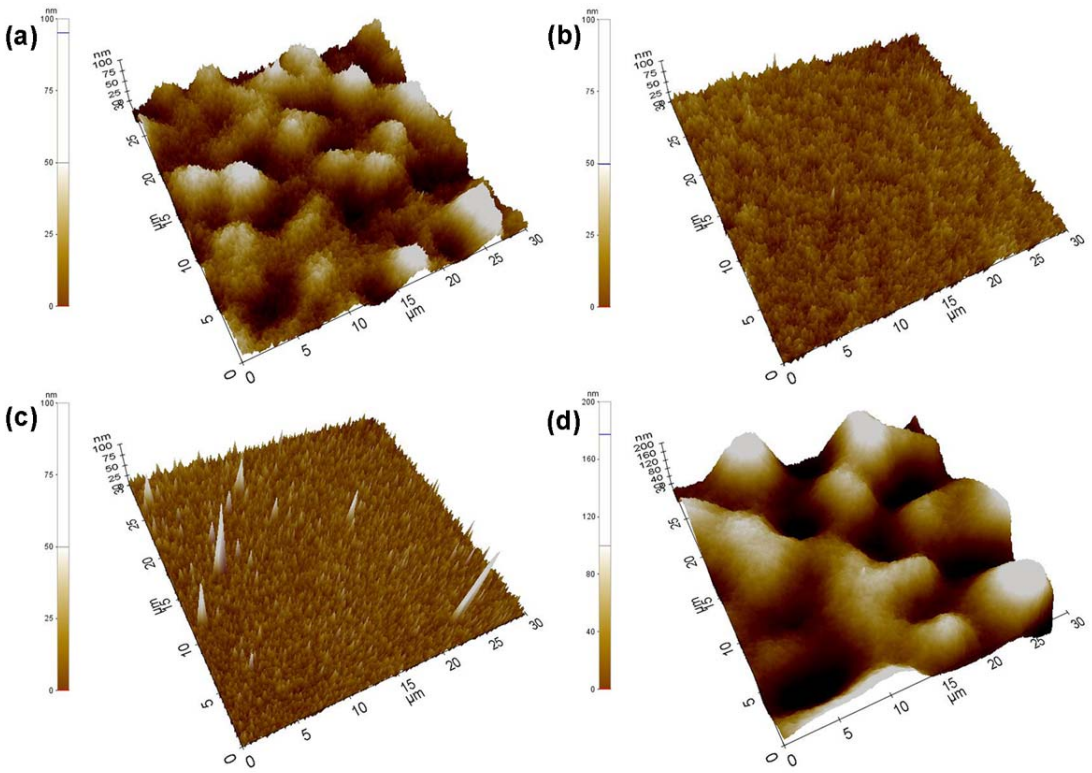

Figure 5.6 AFM 3D images of films: (a) [PEI(9.9)/SiO_2(4.7)]$_{10}$, (b) [PEI(9.6)/SiO_2(6.5)]$_{10}$, (c) [PEI(4.7)/SiO_2(4.7)]$_{10}$, and (d) [PEI(9.9, 3mM buffer)/SiO_2(4.7, 3mM buffer)]$_{10}$. All of the images represent 30 μm × 30 μm scans. The Z scale of the figures (a), (b), and (c) are 100 nm, and that of the figure (d) is 200 nm. The RMS roughness is (a) 21, (b) 8, (c) 9, and (d) 58 nm, respectively.[154]

A similar film structure has also been observed recently during the *e*-LbL growth of CHI(PB/CHI)$_5$(PB/GS)$_n$, and it was attributed to the nanoparticle clustering.[11] This unique structure is likely more than just the clustering of nanoparticles, because only the fast grown *e*-LbL films show the dual-scale structure, and all the *l*-LbL grown films do not show such a feature. In addition, if it were to be just the clustering of nanoparticles, the thin film would start as a cluster-like structure, which was not observed (Figure 5.5). In fact, quite the opposite, it was observed previously that the *e*-LbL film started with a smooth surface and it transferred to a dual-scale structure at the later stages of the film growth.[11]

5.3.5. Explanation of the pH-controlled *e*-LbL Growth

The vastly distinct assembly process and structure of the thin films when they were prepared at different pH values could be attributed to several reasons. One is the diffusion "in-and-out" of PEI chains towards the surface during the SiO_2 assembly step, another is the charge density variation of PEI chains at different pH, and the third is the conformation change of PEI chains at different pH. The film structures after the assembly of the first PEI and SiO_2 layer at different pH combinations are illustrated in Figure 5.7. As shown in Figure 5.7(a)(left), during the assembly of PEI at the pH of 9.9, a significant number of PEI chains are deposited onto the substrate to compensate for the surface charges due to the low PEI charge density. Due to the low charge density, the PEI chains form a collapsed structure on the substrate. During the following SiO_2 assembly step, the collapsed PEI chains will extend due to the increased charge density of each PEI chain, and the excess PEI chains will diffuse out to the outer surface to interact with more SiO_2 nanoparticles. As a result, more than one monolayer of SiO_2 can be deposited during one single exponential growth step. This exponential growth process will be significantly dependent on the charge density variation of every PEI chain. Therefore, when the pH

difference between the PEI and SiO_2 solutions decreases, the exponential growth process starts to diminish (Figure 5.2).

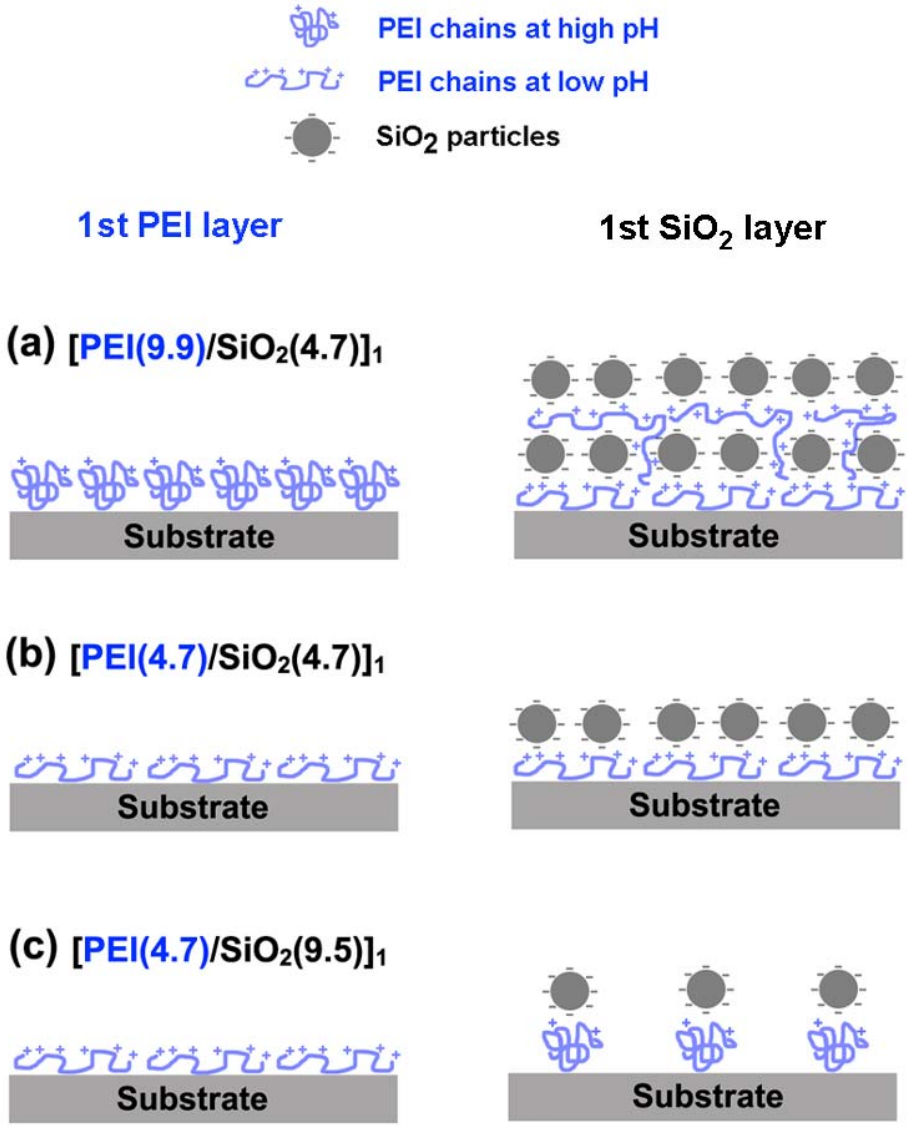

Figure 5.7 Schematic illustration of the first bilayer assembly process for films: (a) $[PEI(9.9)/SiO_2(4.7)]_1$, (b) $[PEI(4.7)/SiO_2(4.7)]_1$, and (c) $[PEI(4.7)/SiO_2(9.5)]_1$. In each thin film, both the assembly of the first PEI and the first SiO_2 layer are illustrated separately.[154]

In contrast, when both the PEI and SiO_2 were assembled at the same pH of 4.7, the charge density of PEI chains will not change between the PEI and SiO_2 deposition step (Figure 5.7(b)). As a result, the $[PEI(4.7)/SiO_2(4.7)]_{10}$ film grows linearly. Increasing

the SiO_2 pH such as was done for the $[PEI(4.7)/SiO_2(9.5)]_{10}$ film will further decrease the assembly rate due to the decreasing PEI charge from the PEI to SiO_2 deposition step. In addition, due to the decreasing PEI charge from low to high pH, the initially extended PEI chains will collapse at the pH of 9.5 during the SiO_2 assembly step (Figure 5.7(c) left), and thus the substrate surface cannot be fully covered by the PEI chains. As a consequence, the negatively charged SiO_2 particles can only be deposited onto the few available positively charged surface sites on the substrate, and the film eventually grows into a cluster-like structure, similar to what was observed in Figure 5.4(d) for the film $[PEI(4.7)/SiO_2(9.5)]_{10}$.

5.3.6. Effect of Ionic Strength in PEI Solution on the *e*-LbL Growth

In order to investigate the ionic strength effect on the exponential growth of $[PEI/SiO_2]_{10}$, 0.1M NaCl was added into the PEI solution to prepare the [PEI(10.1, 0.1M NaCl)/SiO_2(4.7)]$_{10}$ thin film. As shown in Figure 5.8, when NaCl was added into the PEI solution, the exponential growth process was completely diminished, and the thin film growth process converted into a typical linear growth. In addition, the growth rate in the linear growth regime of $[PEI(9.9)/SiO_2(4.7)]_{10}$ was almost twice as big as that of the [PEI(10.1, 0.1M NaCl)/SiO_2(4.7)]$_{10}$ film (Table 5.1). This phenomenon is quite different from the ionic strength effect on the LbL assembly of $[PDDA/PSS]_n$ multilayers, in which case the increased ionic strength amplified the exponential growth.[110] The different ionic strength effect in these films is probably due to the screening effect of NaCl on the positive charges of the PEI chains at high ionic strength. As mentioned earlier, the exponential growth of $[PEI/SiO_2]_n$ multilayers can be attributed not only to the excess number of PEI chains on the outermost surface due to the PEI diffusion, but also to the excess amount of positive charges on every PEI chain due to the pH difference between the PEI solution and the SiO_2 suspension. At low ionic strength, not only can the PEI chains on the surface, but also those PEI chains within a certain distance from the

substrate surface, interact with oppositely charged SiO_2 particles due to the large electrical double layer thickness at low ionic strength (~100 nm at 10^{-6} M NaCl [155]). However, at the NaCl concentration of 0.1 M, the electrical double layer thickness is much smaller (~0.3 nm [155]) due to the screening effect, and only those PEI chains on the surface can interact with SiO_2 to form the next SiO_2 layer. In addition, only a small number of SiO_2 particles that are within a short distance from the substrate surface can "feel" the opposite charge on the substrate. Therefore, the SiO_2 deposition rate was found to be much lower at high ionic strength. The ionic strength effect is different here compared to that on the LbL assembly of $[PDDA/PSS]_n$, in which case the increased ionic strength promoted the *e*-LbL growth.[110] This discrepancy of ionic strength effect is due to that the PDDA and PSS were assembled at the same pH, the *e*-LbL growth process was not relying on the charge increase of the charge of polyelectrolyte chains.

It is worth noting that the linear growth rate of the [PEI(10.1, 0.1M NaCl)/SiO_2(4.7)]$_{10}$ film is more than 4 times higher than that of the [PEI(4.7)/SiO_2(4.7)]$_{10}$ film (Table 5.1). This indicates that the increased positive surface charge due to the increased charge density of every PEI chain still played a significant role even at high ionic strength. Furthermore, according to the AFM image of this sample (Figure 5.4(e)), the surface RMS roughness of the [PEI(10.1, 0.1M NaCl)/SiO_2(4.7)]$_{10}$ film increased to 24.5 nm, which is almost 3 times that of the [PEI(9.9)/SiO_2(4.7)]$_{10}$ film. This increased surface roughness can be attributed to the rougher interface between the PEI and SiO_2 layers due to the extrinsic charge compensation of PEI chains at high ionic strength.[75]

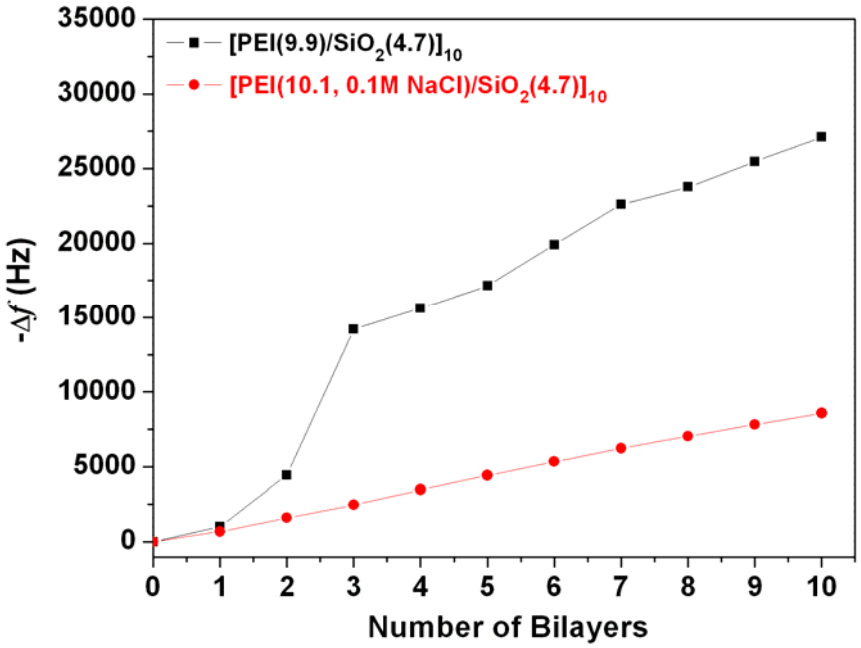

Figure 5.8 The -Δ*f* of QCM crystals during the assembly of $[PEI(9.9)/SiO_2(4.7)]_{10}$ and $[PEI(10.1, 0.1M\ NaCl)/SiO_2(4.7)]_{10}$ thin films.[154]

5.3.7. Effect of pH Buffer on the *e*-LbL growth

During the assembly of exponentially grown $[PEI/SiO_2]_n$ thin films, the pH of PEI and SiO_2 solutions will gradually change during the assembly process. In fact, the pH of the PEI and the SiO_2 solutions will respectively decrease and increase, and thus the pH difference between PEI and SiO_2 solutions will get smaller as the assembly proceeds. For example, after assembling 10 bilayers of the $[PEI(9.9)/SiO_2(4.7)]_{10}$ thin film, the pH of the PEI and the SiO_2 solutions changed to 8.2 and 7.0, respectively, bringing these values closer to each other.

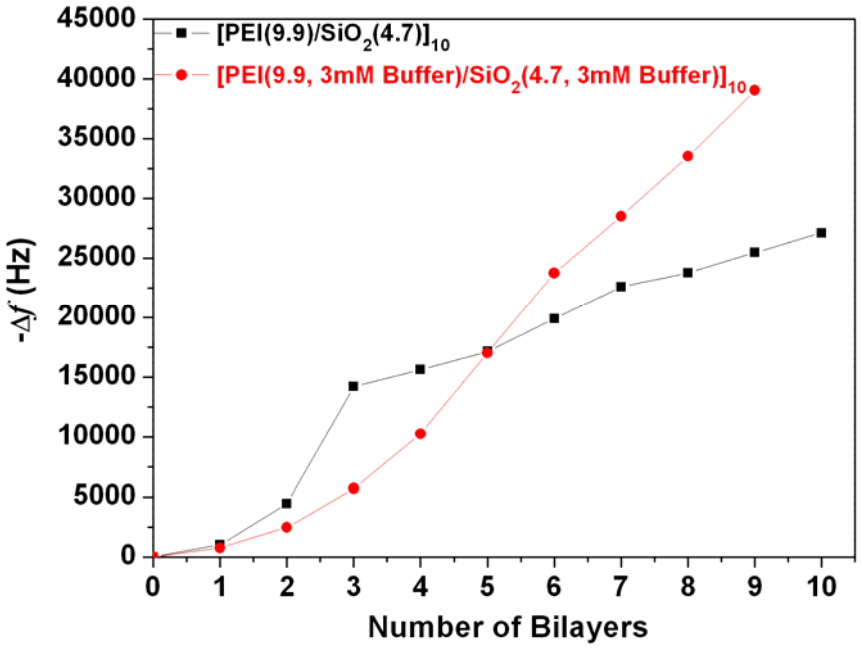

Figure 5.9 -Δf of QCM crystals during the assembly of $[PEI(9.9)/SiO_2(4.7)]_{10}$ and $[PEI(9.9, 3mM\ buffer)/SiO_2(4.7, 3mM\ buffer)]_{10}$ thin films.[154]

In order to evaluate the effect of the pH change of the two solutions on the growth rate, 3mM phosphate buffer was added into both the PEI and SiO_2 solutions. Only that amount was added in order to minimize the ionic strength influence. Due to the buffer effect, the pH of PEI and SiO_2 solutions remained very close to the original values (pH=9.5 in PEI and pH=5.4 in SiO_2 after the 10 bilayer assembly). The difference in thin film growth between $[PEI(9.9)/SiO_2(4.7)]_{10}$ and $[PEI(9.9, 3mM\ buffer)/SiO_2(4.7, 3mM\ buffer)]_{10}$ is shown in Figure 5.9. As shown in the figure, the exponential growth regime of the $[PEI(9.9, 3mM\ buffer)/SiO_2(4.7, 3mM\ buffer)]_{10}$ film lasted until the 5th layer, even though its exponential growth strength was smaller than that of the $[PEI(9.9)/SiO_2(4.7)]_{10}$ film (Figure 5.9 and Table 5.2). In addition, the growth rate in the linear growth regime of the $[PEI(9.9, 3mM\ buffer)/SiO_2(4.7, 3mM\ buffer)]_{10}$ film was significantly higher than that of the thin film deposited in the solution without buffer.

This suggests that the pH difference between the PEI and the SiO_2 solution is critical for both the exponential growth regime and the subsequent linear growth regime of $[PEI/SiO_2]_n$ *e*-LbL thin films. Furthermore, according to the AFM image in Figure 5.4(f), the addition of a small amount of buffer did not increase the film surface roughness.

5.3.8. *e*-LbL Growth Strength

The strength of the exponential growth can be evaluated by simulating the exponential growth curve from QCM results using the equation:[108, 156]

$$(-\Delta f) = f_1 \exp(\beta n) - f_2 \qquad (5.2).$$

Using this equation, the $-\Delta f$ of QCM crystals can be fitted to the buildup of n bilayers through fitting parameters f_1, f_2, and β. f_1 and f_2 are the kinetic scaling factors for the thin film growth process, and they are usually equal. The parameter, β, is the characteristic parameter for the exponential growth strength, and it has been named the exponential growth "strength factor".[108, 156] A value of β close to 0 corresponds to a linearly grown thin film, whereas a large value of β means the thin film grows exponentially. The larger the value of β, the stronger the exponential growth effect. The parameter β for the thin film $[PEI/SiO_2]_{10}$ grown at different conditions, as well as some other *e*-LbL thin films from the literature, is listed in Table 5.2. As shown in the table, the parameter β for all of the *e*-LbL polyelectrolyte multilayer thin films was around or below 0.4 when they were deposited at the same pH. However, when the $[PEI/PAA]_n$ multilayers were deposited in PEI at a high pH and PAA at a low pH, the exponential growth "strength factor" was as high as 0.79. If an *e*-LbL thin film could sustain the exponential growth process for 10 bilayers, with a β of 0.4, the final film thickness would be 110 times the thickness of the first bilayer; whereas with a β of 0.79, the final film thickness would be more than 2200 times the value of the first bilayer. The *e*-LbL generally does not last for the whole assembly process, and the *e*-LbL growth is always

followed with the *l*-LbL growth.[108, 157] Even so, the *e*-LbL growth with a big "strength factor" is still desired for obtaining fast film growth.

As shown in Table 5.2, during the assembly of $[PEI/SiO_2]_n$, the strength factor β is 1.09 when the pH of PEI and SiO_2 solutions are at 9.9 and 4.7, respectively. The strength factor β significantly decreases when the pH difference between PEI and SiO_2 solutions decreases. The strength factors β of PEI(4.7)/SiO_2(4.7) and PEI(4.7)/SiO_2(9.5) counter-ion pairs are around 9×10^{-7} and 9×10^{-7}, respectively, and they both exhibited a typical *l*-LbL growth. It is worth noting that even though the strength factor β for the PEI(9.9, 3mM buffer)/SiO_2(4.7, 3mM buffer) counter-ion pairs is lower than that of PEI(9.9)/SiO_2(4.7), its film thickness after 10 bilayers was larger than that of $[PEI(9.9)/SiO_2(4.7)]_{10}$ due to the longer exponential growth region and the faster linear growth rate.

Table 5.2 List of the exponential growth "strength factors" of various counter-ion pairs.

Counter-ion pairs [a]	Exponential growth "strength factor" β	Ref.
PEI(9.9)/SiO_2(4.7)	1.09	This work
PEI(9.6)/SiO_2(6.5)	0.22	This work
PEI(4.7)/SiO_2(4.7)	9×10^{-7}	This work
PEI(4.7)/SiO_2(9.5)	7×10^{-7}	This work
PEI(10.1, 0.1M NaCl)/ SiO_2(4.7)	1×10^{-6}	This work
PEI(9.9, 3mM buffer)/ SiO_2(4.7, 3mM buffer)	0.45	This work
PAA(2.2)/PEI-ITO(7)	0.067 (0.006) [f]	This work
PDDA(9.9)/SiO_2(4.7)	0.853	This work
PEI(9.0)/PAA(2.85)	0.79 [b]	Ref [109]
PLL(7.4)/PGA(7.4)	0.45 [b]	Ref [157]
PLL(7.4)/PGA(7.4)	0.31 [b]	Ref [114]
PLL(7.3)/HA(7.3)	0.24 [b]	Ref [106]
PLL(7.0)/PAA(7.0)	0.37 (0.81) [b,e]	Ref [107]
PDDA/PSS	0.38 [c]	Ref [108]
PDDA/PSS	0.38 [b,c]	Ref [110]
PAH(7.4)/PGA(7.4)	0.42 [c]	Ref [156, 158]
PB(4.0)/GS(4.0) [d]	0.043 [b]	Ref [11]

[a] The counter-ion pairs are listed as cation(pH)/anion(pH) unless specifically mentioned otherwise. [b] The "strength factor", β, was not stated in the reference paper. Instead, the "strength factor" was estimated based on the film growth curve in the reference paper. [c] The buildup of PDDA/PSS and PAH/PGA films changed from typical linear to exponential growth when the temperature and ionic strength of the polyelectrolyte solution increased, and only the highest growth strength factor is cited here. [d] The buildup of PB/GS only exhibited *e*-LbL growth when they had a precursor layer $[PB/CHI]_5$. [e] Two different values were obtained from ellipsometry (0.37) and QCM (0.81) measurements. The difference was attributed to the water absorbance and film swelling. [f] See details in section 6.3.14

5.3.9. Transition from *e*-LbL Growth to *l*-LbL Growth

The transition from the exponential growth to the linear growth has also been observed in other systems.[108, 157] The characteristics of this transition are: the transition tends to be quite abrupt without a progressive process, and the linear growth rate is

normally substantially smaller than that of the last exponential growth step. The decrease of film growth rate at the exponential-to-linear transition was observed during the assembly of the $[PEI(9.9)/SiO_2(4.7)]_{10}$ film. In fact, the film growth rate at the last exponential growth step was 7 times higher than that of the first linear growth step (Figure 5.10). However, this decrease was not as significant during the assembly of $[PEI(9.9, 3mM\ buffer)/SiO_2(4.7, 3mM\ buffer)]_{10}$ film (Figure 5.11). This again indicates that the pH difference between PEI and SiO_2 solutions is critical not only for the exponential growth regime but also for the subsequent linear growth regime.

The eventual exponential-to-linear transition observed in all cases reported in the literature was attributed to the limited diffusion range of polyelectrolytes during the later assembly steps once the whole film reaches a certain thickness.[157, 159, 160] The exponential-to-linear transition during the *e*-LbL growth of [PEI/SiO2]n thin films is dependent on the pH conditions. According to Table 5.1, the exponential-to-linear transition during assembly of $[PEI(9.9)/SiO_2(4.7)]_{10}$ and $[PEI(9.9, 3mM\ buffer)/SiO_2(4.7, 3mM\ buffer)]_{10}$ films occurred when the thin film reached around 1.12 and 1.34 μm, whereas that of $[PEI(9.6)/SiO_2(6.5)]_{10}$ occurs when the thin film reached 741 nm. Compared to the *e*-LbL growth of polyelectrolyte multilayers (PEMs),[157, 159, 160] the thickness that the e-LbL growth reached prior to the exponential-to-linear transition of this hybrid films are generally thicker, which is probably due to the nature of hybrid thin films and the pH-amplified polyelectrolyte diffusion in this case. The interaction between nanoparticles and the polyelectrolytes probably produce less anchor points, so that the diffusion of polyelectrolyte chains in the hybrid films are less hindered compared to that in the PEMs.

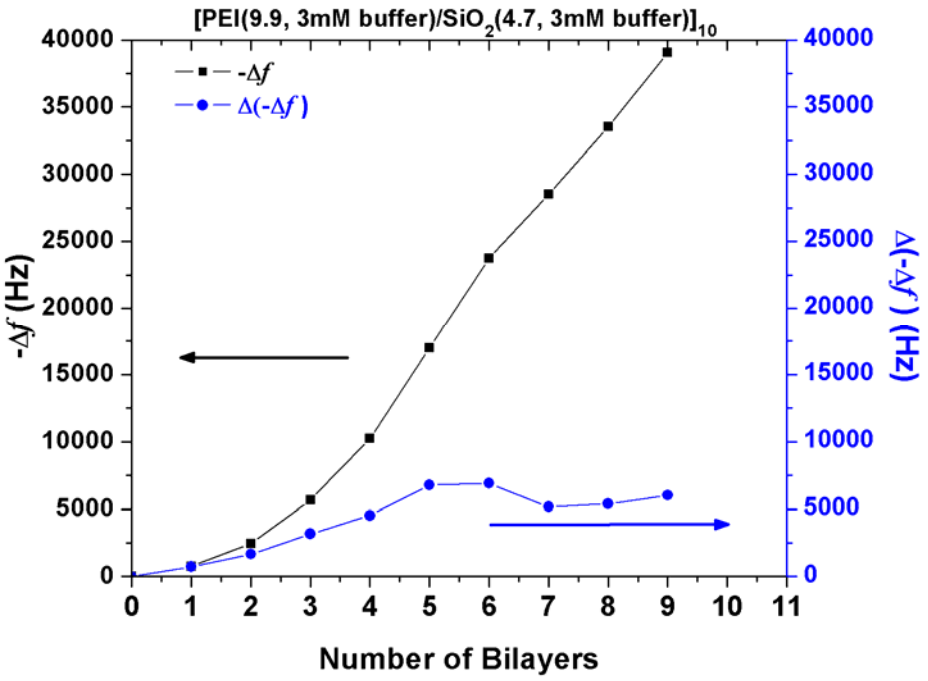

Figure 5.10 The -Δ*f* and Δ(-Δ*f*) during assembly of film [PEI(9.9)/SiO_2(4.7)]$_{10}$.[154]

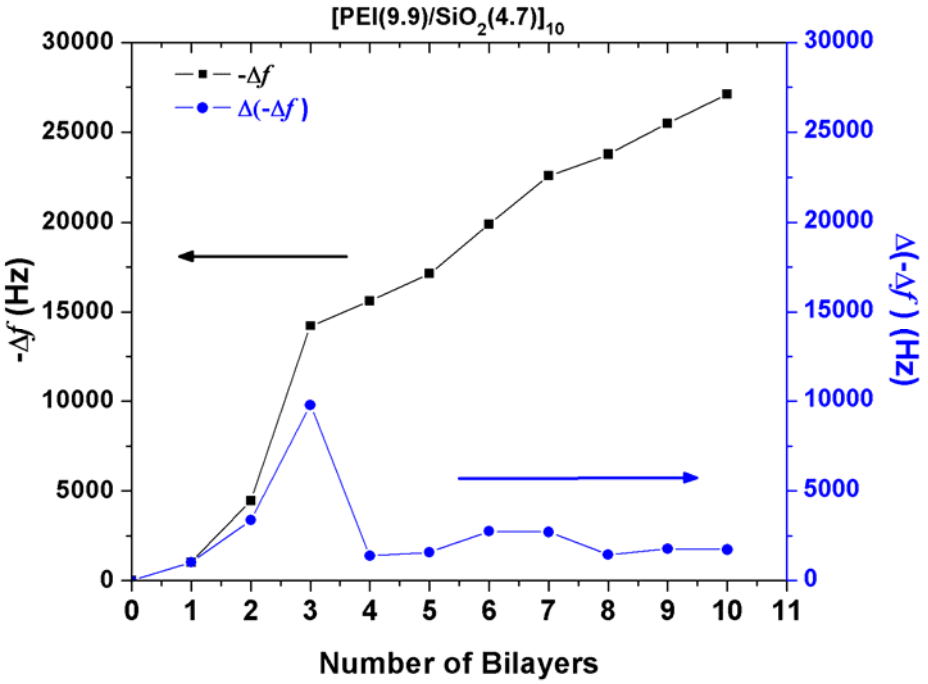

Figure 5.11 The -Δ*f* and Δ(-Δ*f*) during assembly of film [PEI(9.9, 3mM buffer)/SiO_2(4.7, 3mM buffer)]$_{10}$.[154]

5.3.10. Neutron Reflectometry Study of the Film Structure

In order to obtain confirmation of the *e*-LbL and *l*-LbL grown thin films, Neutron Reflectometry [152] (NR) was used to study the structure of films with *one* and *two* bilayers of $[PEI/SiO_2]_n$ that were deposited onto silicon wafers. Due to a scattering contrast between the polymers and the SiO_2 particles and the high thickness sensitivity, NR provides the unique possibility to probe the thickness, the details of the internal structure, the scattering length density (SLD) depth profile of the composite films and the position and distribution of the nanoparticles within the film.[161] The other advantage is that this method is not destructive and provides information averaged over the whole volume of the film. This section presents results obtained for selected films having only *one* and *two* bilayers of the *e*-LbL film $[PEI(9.9)/SiO_2(4.7)]_1$ and $[PEI(9.9)/SiO_2(4.7)]_2$. The NR results of these two films are compared to the *l*-LbL film $[PEI(4.7)/PSS(4.7)/PEI(4.7)/SiO_2(4.7)]_2$. In film $[PEI(4.7)/PSS(4.7)/PEI(4.7)/SiO_2(4.7)]_2$, one extra bilayer of PSS/PEI was assembled between the PEI and SiO_2 layers to bring up the scattering contrast between two SiO_2 layers. The experimental reflectivity results, the fitted results, as well as the SLD profiles for the three samples are shown in Figure 5.12. According to the SLD depth profiles of three samples in Figure 5.12(b), the total thicknesses of the $[PEI(4.7)/PSS(4.7)/PEI(4.7)/SiO_2(4.7)]_2$, $[PEI(9.9)/SiO_2(4.7)]_1$, and $[PEI(9.9)/SiO_2(4.7)]_2$ are 60, 53, and 170 nm respectively.

As shown in Figure 5.12(a), the reflectivity results were fitted well using the proposed SLD profiles. According to the SLD profile of $[PEI(4.7)/PSS(4.7)/PEI(4.7)/SiO_2(4.7)]_2$ (Figure 5.12(b)), this film exhibits a clear two layer structure with each layer thickness of ~30 nm, which is the size of the SiO_2 nanoparticles. It means that

the thin film [PEI(4.7)/PSS(4.7)/PEI(4.7)/SiO_2(4.7)]$_2$ developed a stratified structure due to the introduction of the extra PSS/PEI layer. According to the SLD profile of [PEI(9.9)/SiO_2(4.7)]$_1$ (Figure 5.12(b)), the total thickness of thin film [PEI(9.9)/SiO_2(4.7)]$_1$ is about 53 nm. The SLD profile of this film shows that it is not uniform through the film depth, and it comprises a top layer with a higher SLD and a bottom layer with a lower SLD. Since the SLD of SiO_2 is higher than that of PEI, it suggests that the film [PEI(9.9)/SiO_2(4.7)]$_1$ is comprised of a ~20 nm top layer enriched with SiO_2 and a ~30 nm bottom layer enriched with PEI. In other words, the PEI chain did not diffuse all the way out to the top surface, and the top layer is mostly composed of SiO_2 nanoparticles. The SLD depth profile of [PEI(9.9)/SiO_2(4.7)]$_2$ is more complicated than that of [PEI(9.9)/SiO_2(4.7)]$_1$. This is probably due to the multiple "in-and-out" diffusion of PEI chains through the films. Therefore, a region enriched with PEI and a region with less of PEI is formed at the interface between the first and the second PEI/SiO_2 bilayers.

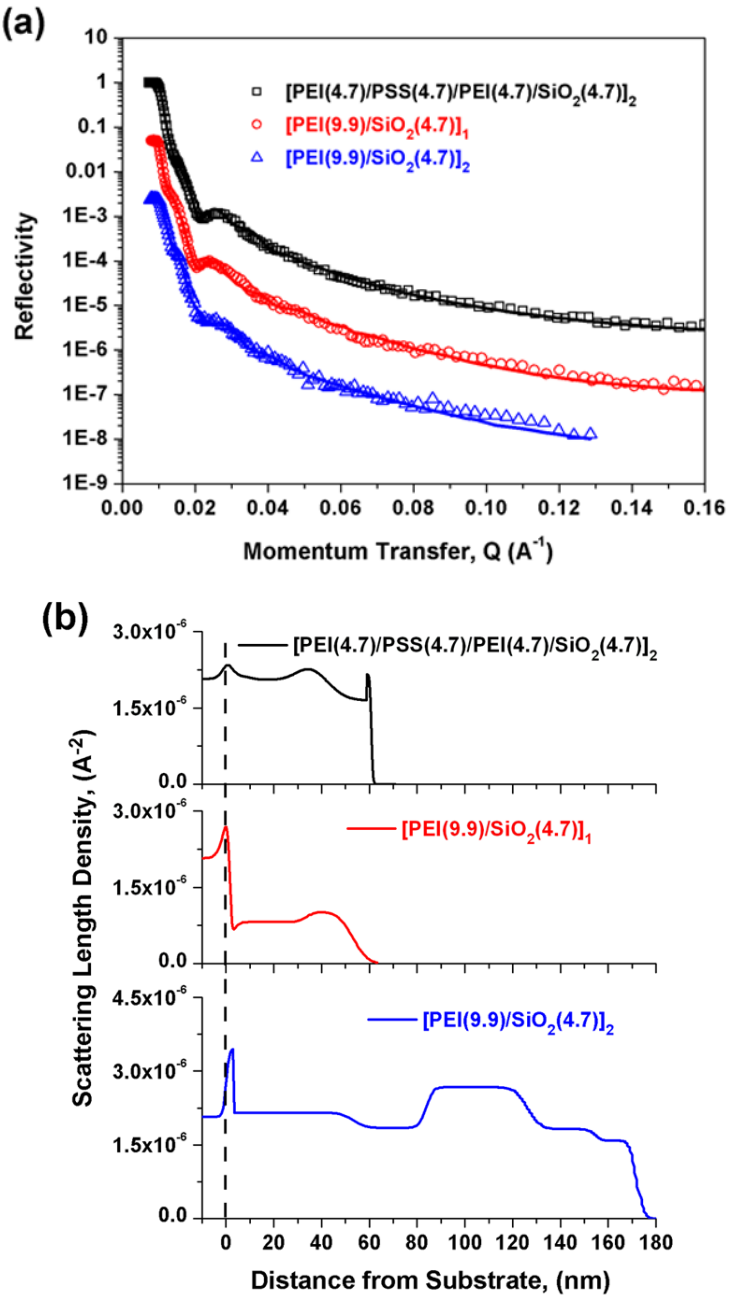

Figure 5.12. (a) Experimental (circles) and fitted (lines) reflectivity profiles for samples $[PEI(4.7)/PSS(4.7)/PEI(4.7)/SiO_2(4.7)]_2$, $[PEI(9.9)/SiO_2(4.7)]_1$, and $[PEI(9.9)/SiO_2(4.7)]_2$. Curves are offset by a factor of 0.1 for clarity. (b) Neutron scattering length density profiles (solid lines) obtained from the fit to the data are shown as functions of the distance from the substrate; the dashed line marks the surface of the Si substrate, the peaked intensity at the substrate corresponds to the naturally oxidized SiO_2 on the surface of the substrate, formed prior to the deposition.[154]

5.3.11. Effect of Substrate on the *e*-LbL growth

It should be noted that the *e*-LbL growth of thin films significantly depends on the substrates. The effect of substrate on the thin film growth was evaluated by comparing the thickness of thin film with the same or similar composition on silicon wafers or SAM-modified QCM crystals. The films deposited on silicon wafers used in the NR experiments are considerably thinner than the films that were deposited onto the QCM crystals under the same pH conditions. As shown in Table 5.3, according to the NR simulation, the thickness of *e*-LbL films $[PEI(9.9)/SiO_2(4.7)]_1$ and $[PEI(9.9)/SiO_2(4.7)]_2$ that were prepared on silicon wafers is 53 and 170 nm, respectively. However, the thickness of these two films prepared on the QCM crystals is 81 and 352 nm, respectively. The reason for this large difference can be attributed to the SAM of MUA on the QCM crystals deposited prior to the first PEI layer. As shown in Figure 5.13, the SAM-modified QCM crystals exhibited negative surface charge, and thus the first layer of PEI deposited onto the QCM crystals through the electrostatic forces. On the other hand, the silicon wafers were not modified by the SAM layers, and the first layer of PEI deposited onto the silicon wafers through the hydrophobic forces. Apparently, different amounts of PEI chains were deposited onto QCM crystals and silicon wafers during the first PEI layer, and this significantly affected the subsequent assembly steps. As opposed to the *e*-LbL films, the film thickness of *l*-LbL films did not show as much difference. As shown in Table 5.3, $[PEI(4.7)/PSS(4.7)/PEI(4.7)/SiO_2(4.7)]_2$ on silicon wafers is 60 nm based on the NR simulation, and that of *l*-LbL film $[PEI(4.7)/SiO_2(4.7)]_2$ on QCM crystals is 46 nm. This slight thickness difference is reasonable, since the film $[PEI(4.7)/PSS(4.7)/ PEI(4.7)/SiO_2(4.7)]_2$ on silicon wafers consists of two more bilayers of PSS and PEI than that of thin film $[PEI(4.7)/SiO_2(4.7)]_2$ deposited on QCM crystals. In other words, the substrate has a strong effect on the *e*-LbL growth, but it does not affect the growth of *l*-LbL films.

Table 5.3 Comparison of thickness of films prepared on silicon wafers and SAM-modified QCM crystals.[154]

Films	On silicon wafers (NR)[a]	On silicon wafers (AFM)[b]	On SAM-modified QCM crystals [c]
$[PEI(9.9)/SiO_2(4.7)]_1$	53	47	81
$[PEI(9.9)/SiO_2(4.7)]_2$	170	131	352
$[PEI(4.7)/PSS(4.7)/PEI(4.7)/SiO_2(4.7)]_2$	60	64	46 [d]

[a] The thickness was obtained by the NR simulation. [b] The thickness was obtained by the AFM. [c] The thickness was obtained by using the equation (5.1) with a C_f constant of 0.079 nm/Hz. [d] The thickness of the thin film $[PEI(4.7)/SiO_2(4.7)]_2$ on SAM-modified QCM crystals was used to compare to that of $[PEI(4.7)/PSS(4.7)/PEI(4.7)/SiO_2(4.7)]_2$ on silicon wafers.

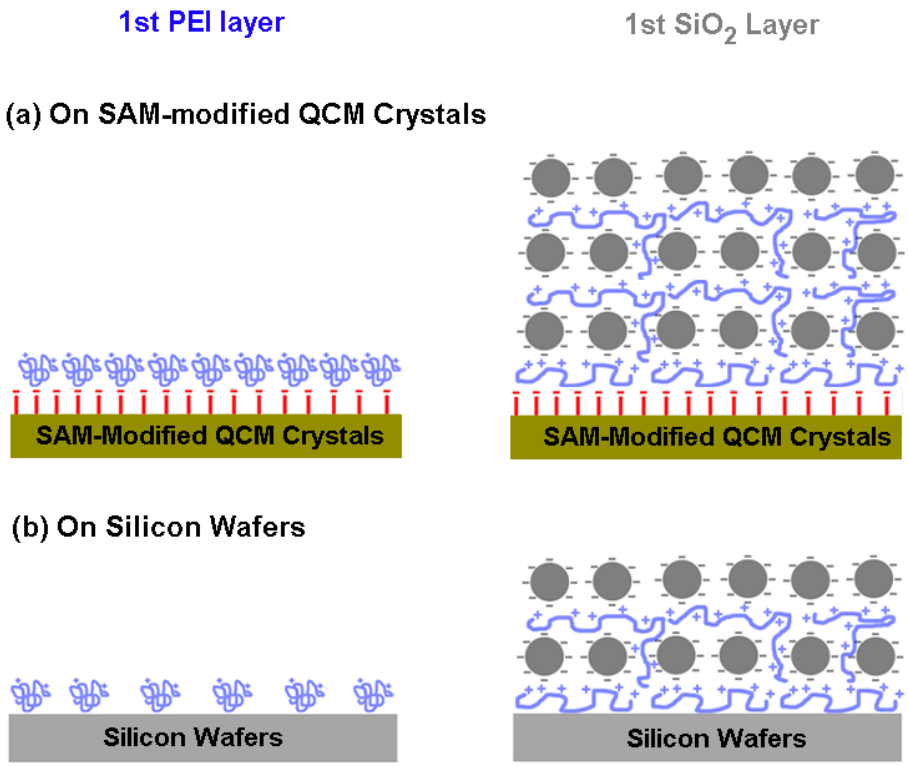

Figure 5.13 Illustration of the substrate effect on the first bilayer of the *e*-LbL growth of $[PEI/SiO_2]_n$ on the (a) SAM-modified QCM crystals or (b) the silicon wafers.

This observation of the significant substrate effect on the *e*-LbL film growth is quite different than the usual observation for the LbL film growth. During the *l*-LbL

growth of $[PSS/PAH]_n$ on silicon wafers, it was observed that only the deposition of the first layer of PSS was affected by different surface modification of the substrate. After the first PSS layer, the thin film growth was found to be independent on the substrate.[1]

5.3.12. LbL Growth Process for 50 Bilayers

In order to evaluate the thin film growth beyond 10 bilayers, two 50-bilayer thin films were prepared and studied their thickness using SEM. The two thin films were respectively assembled from solutions with and without phosphate buffer, and they are denoted as $[PEI(9.9)/SiO_2(4.7)]_{50}$ and [PEI(9.9, 3mM buffer)/SiO_2(4.7, 3mM buffer)]$_{50}$. If the thin film beyond the 10^{th} layer grew at the same speed as that of the linear growth regime indicated in QCM results, the film thickness of $[PEI(9.9)/SiO_2(4.7)]_{50}$ and [PEI(9.9, 3mM buffer)/SiO_2(4.7, 3mM buffer)]$_{50}$ should be around 8 and 20 μm, respectively. However, according to the SEM images in Figure 5.14, their thicknesses are only 3.3 and 4.7 μm, respectively.

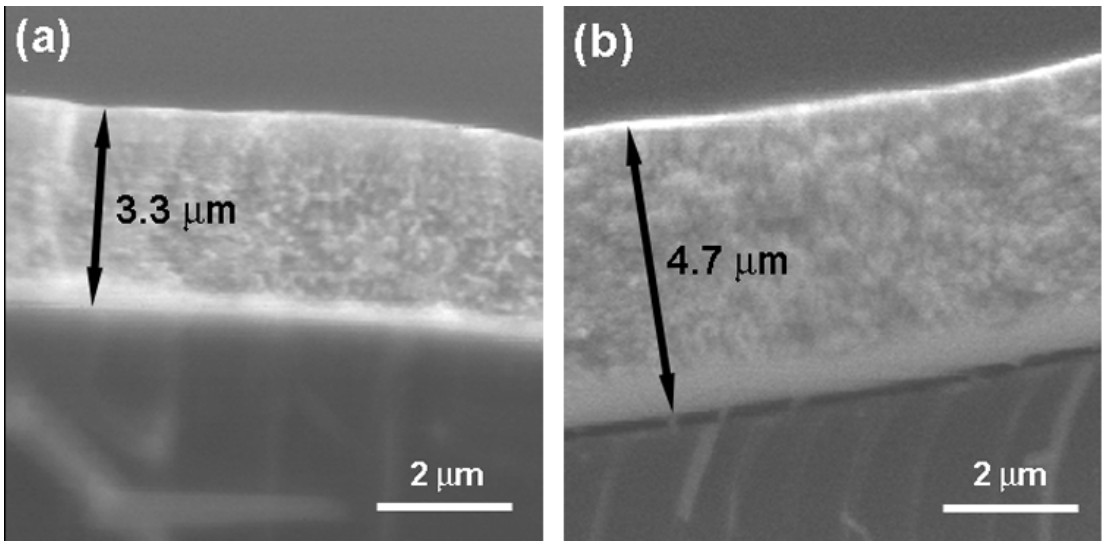

Figure 5.14 The cross-section SEM images of films: (a) $[PEI(9.9)/SiO_2(4.7)]_{50}$ and (b) [PEI(9.9, 3mM buffer)/SiO_2(4.7, 3mM buffer)]$_{50}$. The arrows indicate the thickness of thin films.[154]

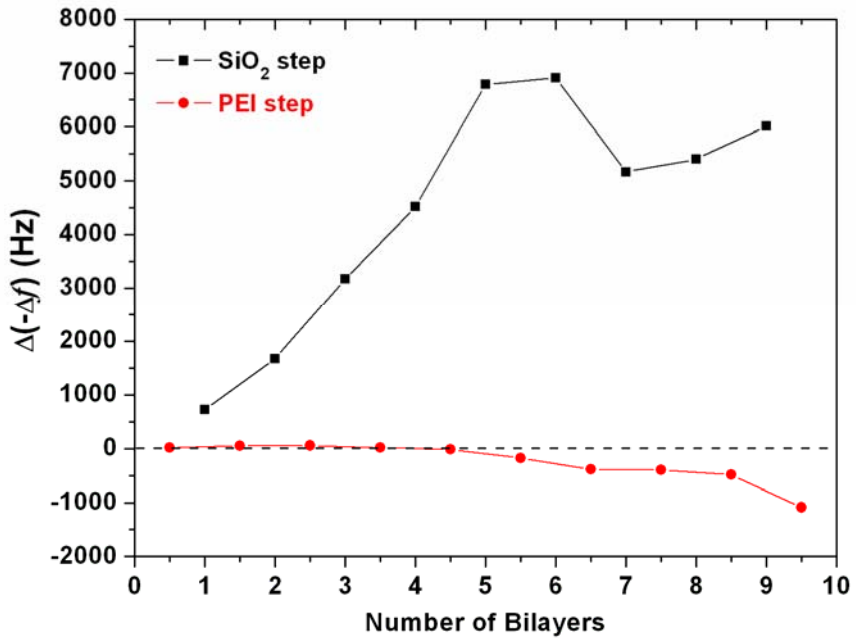

Figure 5.15 The QCM frequency change for each assembly steps of SiO_2 or PEI, $\Delta(-\Delta f)$, during the assembly of $[PEI(9.9, 3mM\ buffer)/SiO_2(4.7, 3mM\ buffer)]_{10}$ film.[154]

The small thin film thickness of the 50-bilayer thin films is due to a slower linear growth rate beyond the 10 bilayers. In Figure 5.15, the frequency change during each SiO_2 or PEI assembly steps, the $\Delta(-\Delta f)$, are generated. The $\Delta(-\Delta f)$, instead of the $-\Delta f$, has been used before to reveal the detail of the thin film growth,[106] and it is used here for the same purpose. As shown in the figure, during the exponential growth regime the $\Delta(-\Delta f)$ at PEI steps is minimal compared to that at the SiO_2 steps. After the exponential-linear transition, the $\Delta(-\Delta f)$ at PEI steps start to decrease to a negative value, which means some SiO_2 particles started to detach from the substrate during the PEI assembly step. At the 10^{th} bilayer, the $\Delta(-\Delta f)$ at PEI steps actually decrease to -1088 Hz, which is quite significant compared to that at the prior SiO_2 assembly step (6014 Hz). In other words, more than 18 wt% of the mass that had deposited during the 9^{th} SiO_2 layer was removed from the thin film during the following PEI assembly step. This ratio is seen to increase in the following assembly steps based on the trend of the curve. This type of thin film

material loss can also be observed in cracks developed during the growth of [PEI(9.9, 3mM buffer)/SiO_2(4.7, 3mM buffer)]$_{10}$ film (Figure 5.16(a)) and [PEI(9.9)/SiO_2(4.7)]$_{10}$ film (Figure 5.16(b)).

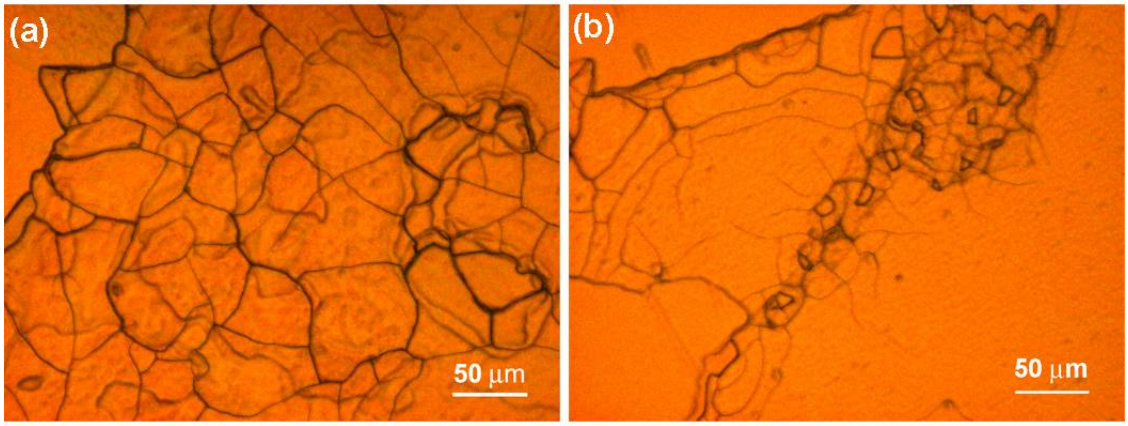

Figure 5.16 Optical image of (a) the [PEI(9.9, 3mM buffer)/SiO_2(4.7, 3mM buffer)]$_{10}$ thin film and (b) the [PEI(9.9)/SiO_2(4.7)]$_{10}$ film.[154]

The removal of SiO_2 from the thin film during the later PEI assembly steps is probably due to the sudden decrease of the positive charges in the thin films when the thin film is transferred from SiO_2 solution (pH equals to 4.7) to PEI solution (pH equals to 9.9). The charge density of PEI at pH of 9.9 is much smaller than that of PEI at pH of 4.7.[58] Therefore, the amount of positive charge in the thin film will suddenly decrease once the substrate is immersed in PEI solution at pH of 9.9 before the supply of newly deposited PEI, and thus the positive charges are not enough to "hold" all of the SiO_2 particles in place.

5.3.13. Inorganic Content of the *e*-LbL films

The SEM cross-section images (Figure 5.14) and the QCM results (Figure 5.15) indicate that both thin film [PEI(9.9)/SiO_2(4.7)]$_n$ and [PEI(9.9, 3mM buffer)/SiO_2(4.7, 3mM buffer)]$_n$ are primarily composed of nanoparticles. The inorganic content of the *e*-LbL film was further confirmed using TGA by heating the thin film and the colloidal SiO_2 particles up to 800°C. As shown in Figure 5.17, about 98 wt% of the colloidal SiO_2

particles is composed of non-combustible inorganic materials, and about 2 wt% of the SiO_2 particles are combustible organics, which might be the organic stabilizing agent for the SiO_2 colloidal suspension. Moreover, about 90 wt% of $[PEI(9.9)/SiO_2(4.7)]_{50}$ film is composed of non-combustible inorganic materials. It means that over 90% of the $[PEI(9.9)/SiO_2(4.7)]_{50}$ thin films is contributed by the colloidal SiO_2. According to the TGA results, the $[PEI(9.9, 3mM\ buffer)/SiO_2(4.7, 3mM\ buffer)]_{50}$ is also primarily composed of SiO_2 nanoparticles (over 90 wt%, data not shown).

This is the first time that such thick and dense films containing primarily inorganic nanoparticles have ever been manufactured by layer-by-layer assembly. The discovery of the pH-controlled *e*-LbL assembly of bicomponent PEI/SiO_2 thin films provides the first step towards being able to make multifunctional films with designed properties. This feature will be very important for any type of film in which the inorganic interparticle connection is very critical for the film functionality or where specific gradients in density are desired.

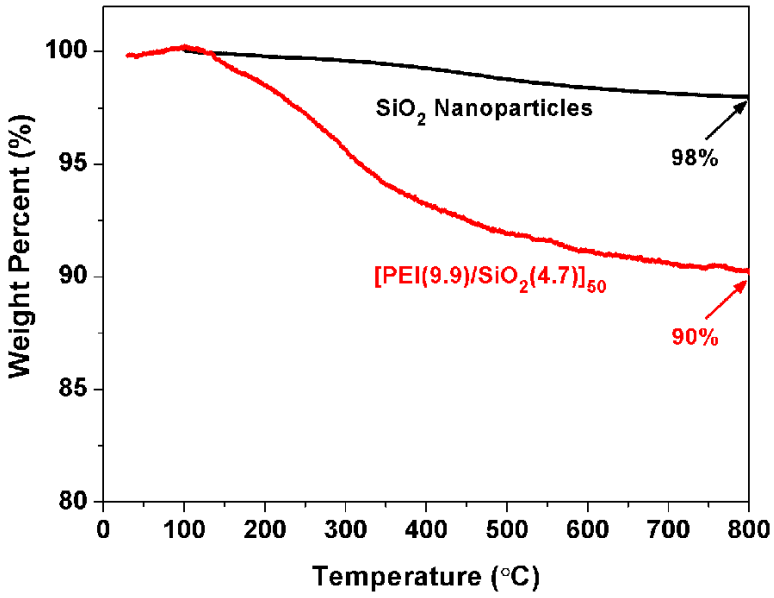

Figure 5.17 Thermogravimetric analysis of spin-coated colloidal SiO_2 nanoparticles and the $[PEI(9.9)/SiO_2(4.7)]_{50}$ thin film.[154]

5.3.14. LbL Assembly of $[PAA(2.2)/PEI\text{-}ITO(7)]_n$ Film

In order to explore the possibility of exponentially growing ITO thin films, an ITO thin film was assembled using PAA as the polyanion. PAA is a weak polyelectrolyte, and its pK_a is around 4.5.[122] Therefore, at a pH below 4.5, the PAA is weakly negatively charged, whereas at a pH above 4.5, the PAA can significantly gain more negative charges. Therefore, as shown in Figure 5.18, the $[PAA/PEI\text{-}ITO]_n$ film was assembled in PAA at a pH of 2.2 and in PEI-ITO at a pH of 7, in order to maximize the charge difference of PAA. PEI-ITO, instead of unmodified ITO, was chosen for this assembly, because unmodified ITO is not stable at pH above 5 (Figure 3.1), but the PEI-modified ITO at a PEI:ITO ratio of 1:200 at 0.1 wt% is stable at pH around 7. No NaCl was intentionally added into the PAA solutions. This thin film is thus denoted as $[PAA(2.2)/PEI\text{-}ITO(7)]_{10}$ for easier description.

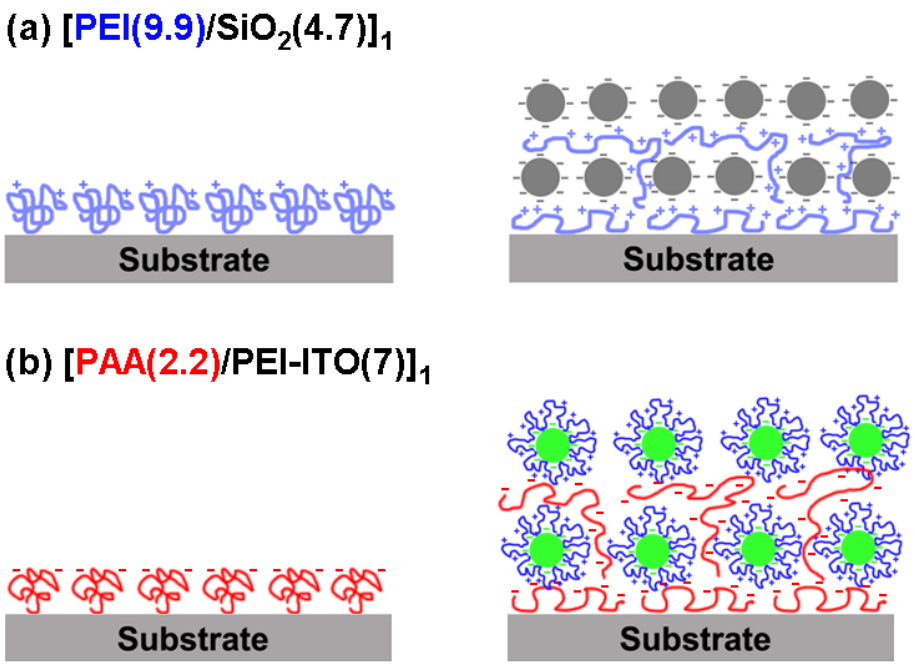

Figure 5.18 Schematic comparison of the first bilayer assembly of (a) $[PEI(9.9)/SiO_2(4.7)]_1$ and (b) $[PAA/PEI\text{-}ITO]_1$.

As shown in Figure 5.19, unlike the thin film $[PEI(9.9)/SiO_2(4.7)]_{10}$, the thin film $[PAA(2.2)/PEI\text{-}ITO(7)]_{10}$ grew linearly during the LbL assembly process. Even though the charge of PAA was increased from the PAA assembly step to the PEI-ITO assembly step due to the pH increase, the thin film grew linearly. It is still unclear why this assembly process exhibited *l*-LbL growth. One possible reason might be the strong interaction between PAA and PEI-ITO layers due to the PEI modification, compared to that between PEI and SiO_2 layers. The stronger interaction and polyelectrolyte chain entanglement between PAA and PEI-ITO layers might refrain the diffusion of PAA chains. Another possible reason might be the large ITO particle sizes. As shown in Figure 3.2, the ITO nanoparticles form 200 nm agglomerates in the colloidal suspensions, and this particle size is much bigger than that of the SiO_2 particles (~ 30 nm). The large particle size of ITO particles might hinder the diffusion of PAA chains during the assembly, which will eliminate the *e*-LbL growth.

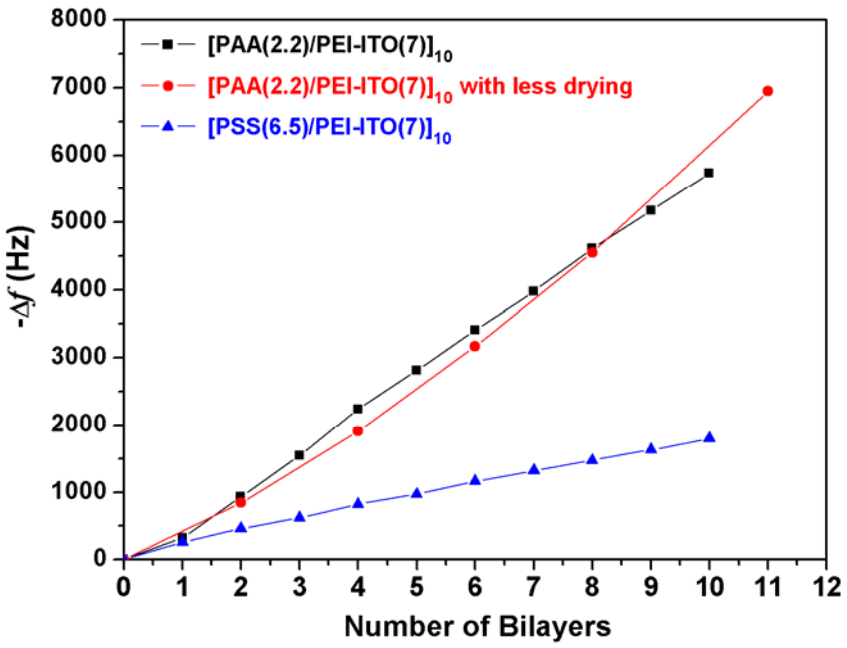

Figure 5.19 The $-\Delta f$ of QCM crystals during the assembly of $[PAA(2.2)/PEI\text{-}ITO(7)]_{10}$, $[PAA(2.2)/PEI\text{-}ITO(7)]_{11}$ with less drying, and $[PSS(6.5)/PEI\text{-}ITO(7)]_{10}$ films.

The buildup of film $[PAA(2.2)/PEI\text{-}ITO(7)]_{10}$ was also compared with that of film $[PSS(6.5)/PEI\text{-}ITO(7)]_{10}$. PSS is a strong polyelectrolyte, and thus the electrical charge of PSS will not change in this case. To make the comparison valid, no NaCl was added into the PSS solution. As shown in Figure 5.19, the film $[PSS(6.5)/PEI\text{-}ITO(7)]_{10}$ also grew linearly through the assembly process. Interestingly, the linear growth rate of $[PAA(2.2)/PEI\text{-}ITO(7)]_{10}$ film was more than two times that of the $[PSS(6.5)/PEI\text{-}ITO(7)]_{10}$ film. This can be attributed to the increasing negative charge of PAA in the film during the assembly of PEI-ITO at pH of 7. The excess of negative surface charge on film surface increased the linear growth rate.

It has been shown that the *e*-LbL growth process can be promoted by limiting the number of film drying steps during the assembly.[116] As shown in Figure 5.19, if the $[PAA(2.2)/PEI\text{-}ITO(7)]_{10}$ thin film was dried only at every other ITO layer, the film buildup process exhibited a trend towards exponential growth during the assembly of $[PAA(2.2)/PEI\text{-}ITO(7)]_{10}$. In fact, the exponential growth "strength factor" β during the assembly of $[PAA(2.2)/PEI\text{-}ITO(7)]_{10}$ by applying less drying steps was 0.067, while normal drying resulted in β of 0.006. In other words, the film growth of $[PAA(2.2)/PEI\text{-}ITO(7)]_{10}$ under regular drying condition was a typical *l*-LbL growth process, whereas the film growth with fewer drying steps showed a weak *e*-LbL growth process. This is probably due to the easier diffusion of PAA when fewer drying steps were applied. The drying step can probably introduce the anchor points of polyelectrolytes to the surrounding nanoparticles, and thus the diffusion of PAA can be hindered.

The film structure of $[PAA(2.2)/PEI\text{-}ITO(7)]_{10}$ with regular drying procedure and that of $[PAA(2.2)/PEI\text{-}ITO(7)]_{11}$ with less drying steps are compared in Figure 5.20. As shown in the figure, no obvious surface structure difference could be observed for these two films, which is probably due to the weak *e*-LbL growth process and the

polydispersed ITO nanoparticles. In addition, no two-scale structure was thus observed for the e-LbL grown films (Figure 5.20(b)).

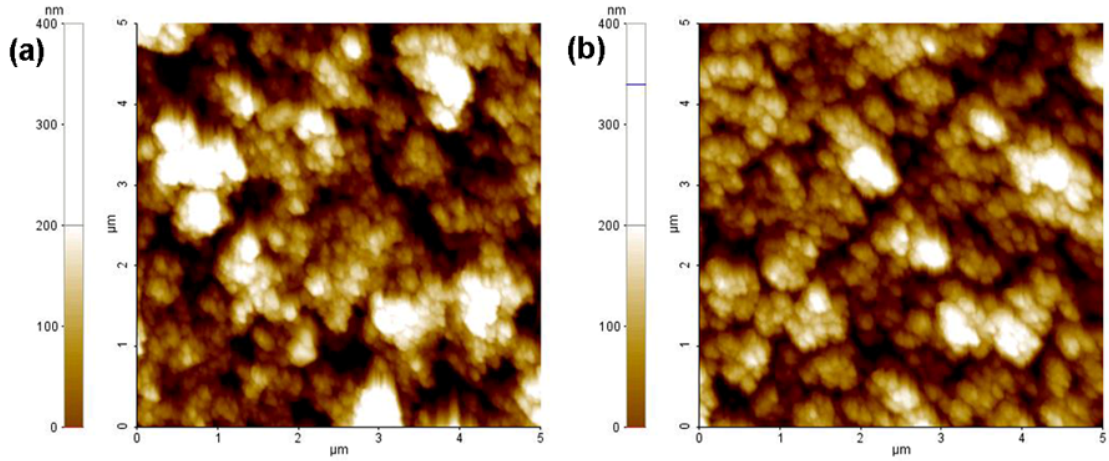

Figure 5.20. AFM images of (a) $[PAA(2.2)/PEI\text{-}ITO(7)]_{10}$ and (b) $[PAA(2.2)/PEI\text{-}ITO(7)]_{11}$ with less drying steps.

5.3.15. LbL Assembly of $[PDDA(9.9)/SiO_2(4.7)]_n$ Film

In order to justify the effect of weak polyelectrolyte on the *e*-LbL growth of hybrid thin films, PDDA, a strong polyelectrolyte, was used to prepare $[PDDA(9.9)/SiO_2(4.7)]_{10}$ thin film. As shown in Figure 5.21, similar to the $[PEI(9.9)/SiO_2(4.7)]_{10}$, the $[PDDA(9.9)/SiO_2(4.7)]_{10}$ also shows exponential growth in the initial three bilayers. The exponential growth "strength factor" β for the $PDDA(9.9)/SiO_2(4.7)$ counter-ion pair is 0.853, relatively smaller than that of the $PEI(9.9)/SiO_2(4.7)$. Due to this smaller "strength factor", the buildup of thin film $[PDDA(9.9)/SiO_2(4.7)]_{10}$ is slower than that of $[PEI(9.9)/SiO_2(4.7)]_{10}$.

The pH of PDDA solution and SiO_2 suspensions are also critical for growth process. As shown in Figure 5.21, after the 3rd bilayer, the exponential growth transferred to linear growth. After the 5th bilayer, the pH of the PDDA solutions and the SiO_2 suspensions changed to 7.8 and 6.0, respectively. In other words, the pH difference between the PDDA solutions and the SiO_2 suspensions decreased. By adjusting the pH

value of these two solutions back to the original value, the growth rate of thin film significantly increased during the 6th bilayer. However, this increase of film growth rate could not maintain for more steps, and the growth rate decreased again at the 7th bilayer. Similarly, the pH adjustment of the PDDA solution and the SiO_2 suspension increased the growth rate at the 8th bilayer.

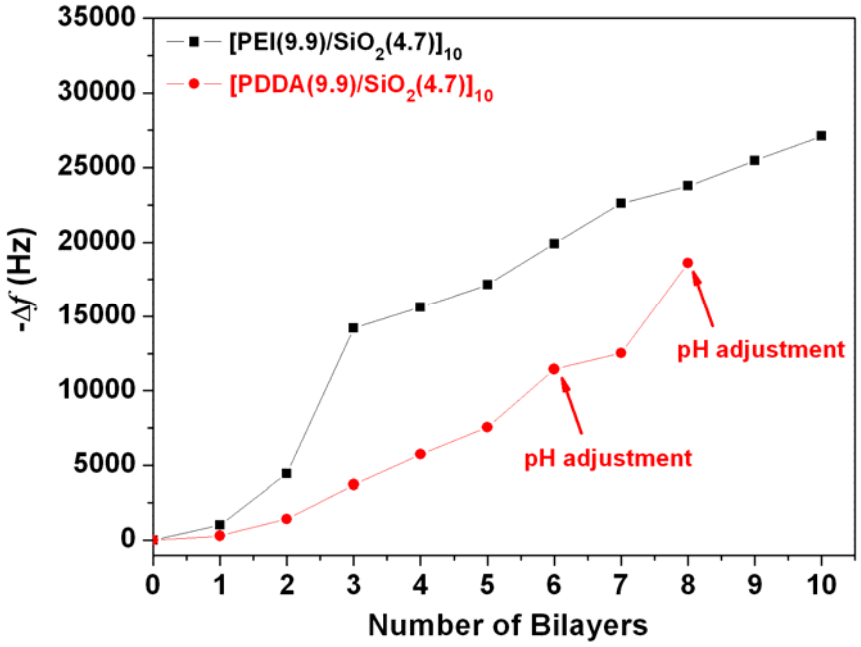

Figure 5.21. The -Δ*f* of QCM crystals during the assembly of $[PEI(9.9)/SiO_2(4.7)]_{10}$, and $[PEI(9.9)/SiO_2(4.7)]_{10}$ films.

5.4. Conclusions

A new type of exponentially grown organic/inorganic bicomponent composite thin film was demonstrated by LbL assembly of PEI and SiO_2 nanoparticles. The results show that the film growth rate is significantly dependent on the pH difference between the PEI and the SiO_2 solutions, the pH buffer strength, as well as the ionic strength. Only when the thin film is deposited with PEI at a high pH and with SiO_2 at a low pH, will the thin film exhibit *e*-LbL growth. The exponential growth strength was shown to significantly decrease when the pH difference decreased or the solutions had pH values in

reverse. Introducing pH buffer into the PEI and SiO_2 solution extends the exponential growth region somewhat, and also increases the growth rate in the subsequent linear growth regime. Unlike the all-organic thin film systems reported by other investigators, increasing the ionic strength of the PEI solution in this case eliminated the exponential growth due to the strong screening effect of NaCl on the positive charges of PEI chains.

In this work, the *e*-LbL grown $[PEI/SiO_2]_n$ thin films are primarily composed of inorganic SiO_2 nanoparticles. This is the first time bicomponent polyelectrolyte/inorganic nanoparticle thin films exhibited *e*-LbL growth. Thin films as thick as 3 μm were prepared, composed of over 90% inorganic SiO_2 nanoparticles within 10 bilayers. The extremely fast thin film growth is attributed not only to the "in-and-out" diffusion of PEI chains, but also to the PEI charge density increase when the pH is changed from a high to a low value. Due to the diffusion of PEI chains, *e*-LbL grown films exhibited a dual-scale structure with very smooth regions at a small scale (~2 μm) that form much rougher islands at a much larger length scale (~ 30 μm). The *e*-LbL growth process is also significantly affected by the substrate. The *e*-LbL growth on the SAM-modified QCM crystals is much faster than that on the silicon wafers, due to the different adsorption mechanism of the first PEI layers. The fundamental understanding of the pH controlled *e*-LbL growth of organic/inorganic bicomponent thin films will have significant impact on the LbL assembly field.

Unlike the thin film $[PEI(9.9)/SiO_2(4.7)]_{10}$, the thin film $[PAA(2.2)/PEI\text{-}ITO(7)]_{10}$ grew linearly during the LbL assembly process. However, this linear growth process can be transferred to a weak *e*-LbL growth process, when fewer drying steps are used during the LbL assembly. Furthermore, the linear growth rate of $[PAA(2.2)/PEI\text{-}ITO(7)]_{10}$ was shown to be about four times higher than that of $[PSS(6.5)/PEI\text{-}ITO(7)]_{10}$ due to the electrical charge increase of every PAA chain in the film.

CHAPTER 6

FABRICATION OF ELECTRICALLY CONDUCTIVE PAPER BY LBL ASSEMBLY OF PSS AND ITO ONTO CELLULOSE FIBERS

6.1. Introduction

In the past few years, functional papers such as conductive paper, catalyst paper, photoluminescent paper and magnetic paper have been manufactured by adding various fillers including conductive polymers, titanium oxide, luminescent polymers and ferric oxide.[162-166] These materials can respond to external stimuli, such as electric field, magnetic field and light. The combination of paper flexibility and extra-functionality gives these materials a wide variety of potential applications.

This chapter examines the possibility of directly coating cellulose fibers with functional inorganic nanoparticles using the LbL assembly method. The cellulose fibers are negatively charged due to their forming process normally being done during the pulping.[167] In traditional paper making method, polyelectrolytes are used to facilitate the retention of fillers.[164, 166, 168] However, using the traditional method, polyelectrolytes and fillers are applied simultaneously, and most of the particles agglomerate together and form big flocs in the paper mats. Compared to the traditional paper making process, the LbL method provides an opportunity to uniformly coat the cellulose fibers with functional nanoparticles. As a result, it is possible to fabricate conductive paper by coating the cellulose fibers with conductive nanoparticles.

Previously, LbL assembly has been used to manufacture conductive paper by using conductive polymer.[162, 163] In this chapter, the conductive paper was fabricated by LbL assembly of PSS and conductive ITO nanoparticles onto the cellulose fibers.

6.2. Experimental Procedure

In this chapter, the bleached kraft softwood cellulose fibers were generously supplied by the Institute of Paper Science and Technology (IPST) at Georgia Tech. These cellulose fibers were coated by LbL assembly of $[PSS/ITO]_{10}$, and this ITO-coated cellulose fibers were manufactured into paper handsheets using a standard procedure. The LbL assembly process was followed by measuring the surface charge of cellulose fiber using zetasizer. The electrical property and the surface structure of the paper were characterized by using impedance spectroscopy, conductive-AFM, SEM, and EDS. The experimental procedure for ζ-potential, impedance spectroscopy, conductive-AFM, SEM, and EDS follows the same procedure that was described in Chapter 2. Here, the procedure of LbL assembly on cellulose fibers, paper manufacturing, as well as the electrical characterization of paper is described.

6.2.1. LbL Assembly Process

The LbL assembly of 10 bilayers of PSS and ITO followed the same procedure that was described in Chapter 2. Only one bilayer of PEI and PSS was assembled as the precursor layer prior to the assembly of ITO nanoparticles. The concentration of PEI solution, PSS solution, and ITO suspension was 0.2, 0.01, and 0.01 wt%, respectively. The pH of the PEI solution, PSS solution, and ITO suspension was 8.5, 6.5, and 2.9, respectively. Compared to the LbL assembly on solid substrate, the LbL assembly on cellulose fibers was performed by suspending the fibers in the solution and filtering the coated fibers using a filter. The assembly of PEI and ITO nanoparticles was performed under gentle agitation for uniform coating, whereas the assembly of PSS was performed under no agitation to minimize the materials lost due to the fiber-to-fiber friction. In this chapter, both the ITO and PEI-ITO suspensions were used for the LbL assembly. For easier description, the cellulose fibers that were coated with 10 bilayers of PSS and ITO or PEI-ITO were denoted as $[PSS/ITO]_{10}$ or $[PSS/PEI\text{-}ITO]_{10}$.

6.2.2. Paper Manufacturing Process

Paper handsheets with dry basis weight of 60 g/m^2 were fabricated according to the TAPPI standard T-205.[169] A schematic of the paper manufacturing process from cellulose fibers is shown in Figure 6.1. As shown in the figure, during the paper manufacturing process, the ITO-coated cellulose fibers were first suspended in water, the water is then drained out from a screen, so that a wet fiber mat was finally formed on the screen. By drying this fiber mat, a sheet of paper can then be formed.[170] The experimental setup of the papermaking machine is shown in Figure 6.2. The papermaking machine consists of a sheet machine, in which the wet fiber mat was formed from the cellulose fibers, a hand press, and a mechanical press. This machine is located at IPST at Georgia Tech.

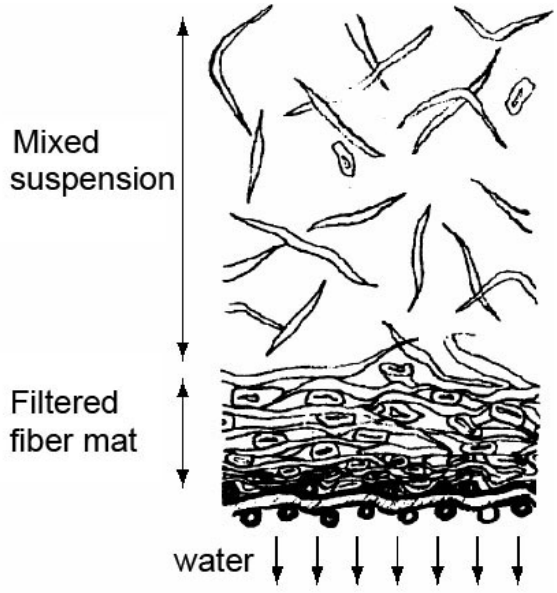

Figure 6.1 Illustration of the papermaking process from cellulose fibers. (The figure has been modified from the reference.)[171]

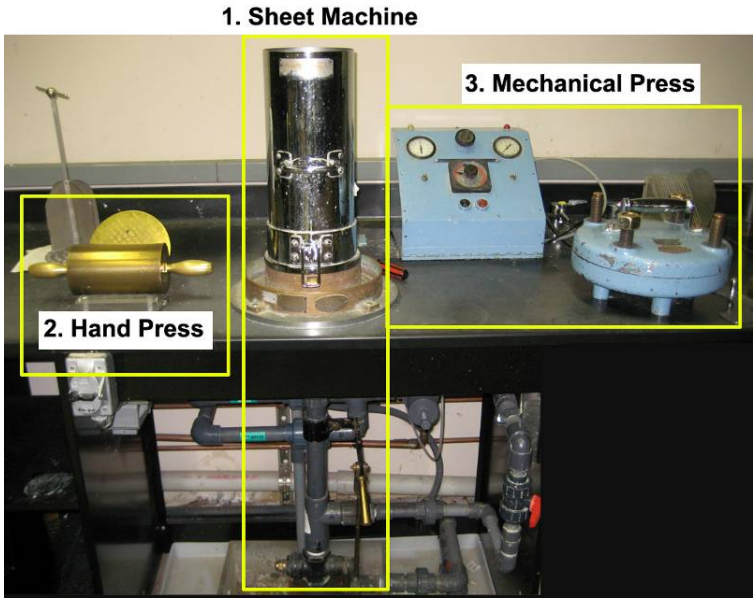

Figure 6.2 Experimental setup of a papermaking machine, including the sheet machine, hand press, and the mechanical press.

6.2.3. Electrical Characterization of Paper

The electrical data of an individual coated fiber and that of handsheets were collected using impedance spectroscopy. The detailed characterization methods were already described in Chapter 2, and only the sample preparation for the measurement is described here.

The electrical properties of the paper handsheets were measured along two directions: (i) in-plane (IP) and (ii) through-the-thickness (TT) directions. The dimensions of the samples measured along the IP and TT directions were 25 mm × 10 mm × 0.15 mm (Length × Width × Thickness), and 0.15 mm × 20 mm (Thickness × Diameter), respectively. The arrangement of the electrodes for the measurement along these two directions is given in Figure 6.3. As shown in Figure 6.3(a), the electrical contact for the measurement along IP direction was achieved by silver painting the two ends of the paper strip, and then using coaxial probers on a probe station attached to the impedance analyzer. On the other hand, as shown in Figure 6.3(b), the specimen setup

used for measurement along TT direction was the parallel-plate-method using 20 cm diameter copper plates as sample fixer and electrodes. The measurement setup for individual fibers was similar to that of paper measurement in the IP direction, in which the paper strip is substituted with one single wood fiber.

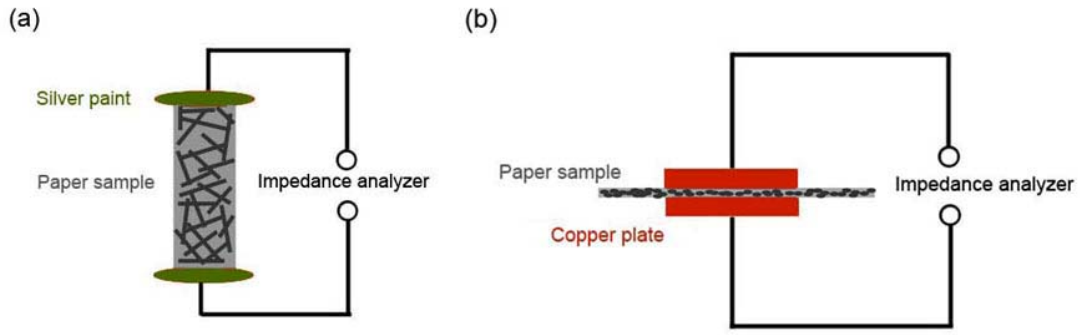

Figure 6.3 Schematic illustration of the electrical measurement setup of paper samples along the (a) in-plane (IP) direction and in the (b) through-the-thickness (TT) direction, respectively.[63]

The actual two-probe station and the impedance analyzer for the electrical measurement, the paper sample for the electrical measurement along the IP direction, and the fiber sample are shown in Figure 6.4. Reproducibility was ensured by measuring at least three samples for each of the different conditions.

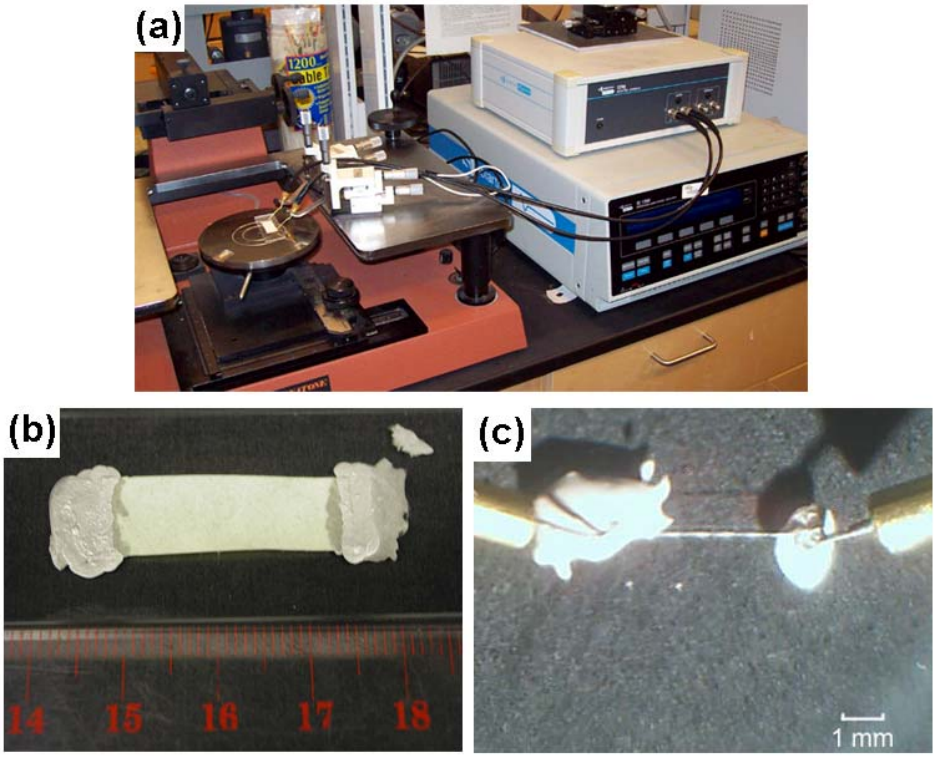

Figure 6.4 (a) The two-probe station and impedance analyzer for the electrical measurement, (b) the paper sample for measurement along the IP direction, and (c) the fiber sample for measurement.

The impedance and the conductivity of the paper handsheets were calculated using equations (2.2) and (2.3) described in Chapter 2. However, for the individual fibers, only its impedance can be derived. The conductivity of a single fiber could not be accurately calculated, due to the difficulty of precisely determining the silver contact area and cross-sectional thickness of the hollow fibers.

6.2.4. Thermogravimetric Analysis (TGA)

The content of ITO particles present in the conductive paper can be evaluated by using the thermogravimetric analysis (TGA, TA Instruments, Q5000 IR). Scans were obtained by heating a small piece of paper up to 700 °C at a heating rate of 10 °C/min under flowing air and measuring the amount of inorganic char, which was taken to be the remnant ITO nanoparticles.

6.3. Results and Discussion

6.3.1. ζ-potential of Cellulose Fibers during LbL Assembly

The ζ-potential of cellulose fibers along the LbL assembly process was evaluated after every assembly step. Some short fibers were taken after each rinsing step, so that the measurement would not be affected by residual polymer or nanoparticles in solution. As shown in Figure 6.5, the virgin fibers were negatively charged, and the surface charge reversed its sign after every assembly step of either polyelectrolytes or ITO. During the assembly of PEI and PSS, the surface charges were completely overcompensated by the charge of the fibers, and the magnitude of the ζ-potential of fibers was all above 30 mV. However, the assembly of one ITO layer could not completely reverse the surface charge, and the ζ-potential of fibers after ITO coating was below 30 mV. This value is reasonable since the ITO coating could not fully cover the fiber surface in only one step. This is also the reason why several ITO coating steps are necessary to form the interconnected ITO network on the fibers. This partial reversing of surface charge has also been observed in previous research on LbL assembly of enzyme and clay particles on wood fibers,[64, 67] and the similar surface charge effect was also discussed in great detail in Chapter 5. It is speculated that this occurred for a similar reason as in the case of these ITO nanoparticles, since neither the enzyme nor clay particles could fully cover the fiber surface in a single coating step.

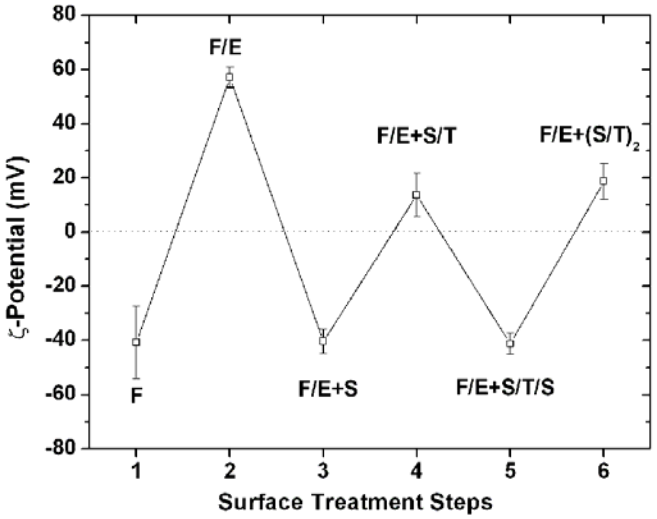

Figure 6.5 ζ-potential of cellulose fibers during the LbL assembly process. In the figure, F, E, S, and T stand for wood fibers, PEI, PSS and ITO, respectively.[63]

6.3.2. Surface Structure of the Assembled Films on Cellulose Fibers

The paper $[PSS/ITO]_{10}$ was investigated by optical imaging and SEM. As shown in Figure 6.6, the conductive paper appears greenish in color which comes from the ITO nanoparticles. As displayed in Figure 6.7(a) and (b), large portions of the fiber surface are coated by ITO nanoparticles. Percolated networks of ITO nanoparticles can form on the fiber surface, due to the preferential particles deposition on some surface defects, such as the regions around the surface microfibrils (Figure 6.7(b)). This preferential deposition can lead to percolation through the sample and can contribute to the long range conductivity of the paper. As seen in Figure 6.7(c), the local region of the percolated network is fully covered by nanoparticles. The particle size is generally around or below 100 nm, which is the same as was determined in a previous TEM measurement of raw powders (Figure 2.1). EDS analysis of the region shown in Figure 6.7(c), which is presented in Figure 6.7(d), clearly shows the presence of In, Sn and O, confirming that these nanoparticles are all ITO. The gold signal present is due to the sputter coating for SEM sample preparation.

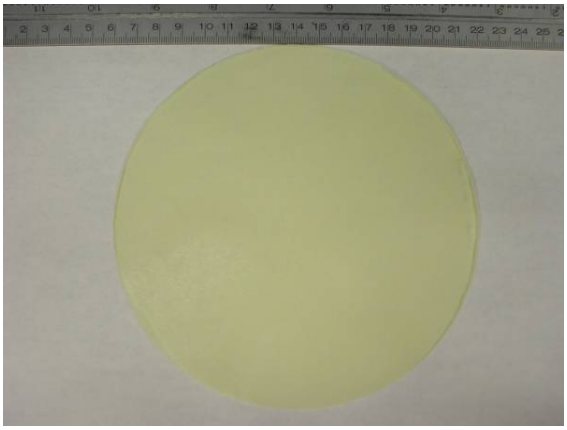

Figure 6.6 Optical image of the paper handsheet $[PSS/ITO]_{10}$.[63]

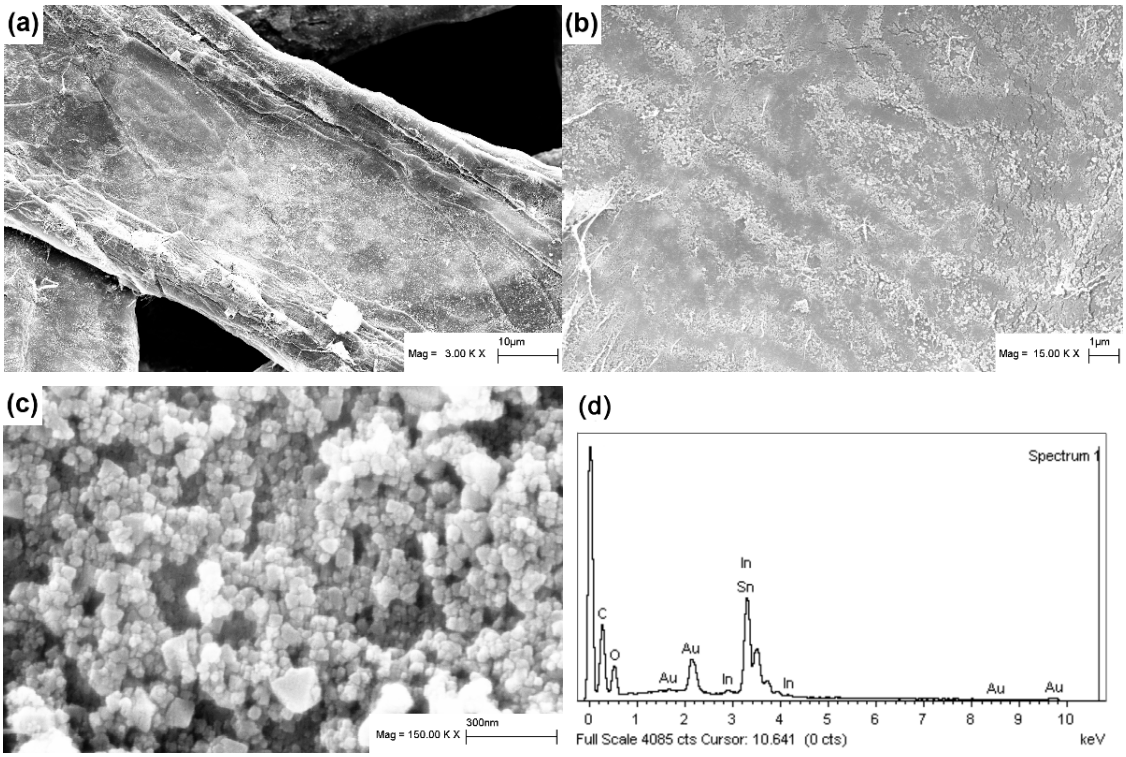

Figure 6.7 SEM micrographs and EDS pattern for paper $[PSS/ITO]_{10}$: (a), (b) and (c) SEM micrographs at different magnifications, (d) EDS element analysis of the whole area of (c).[63]

6.3.3. Electrical Properties

The impedance Nyquist plot of the plain paper, paper $[PSS/ITO]_1$, paper $[PSS/ITO]_5$, paper $[PSS/ITO]_{10}$, and fiber $[PSS/ITO]_{10}$ that were measured along the TT direction are shown in Figure 6.8. As shown in the figure, the plain paper exhibited the

typical behavior of insulating materials. When one layer of ITO nanoparticles is coated onto the wood fibers, the as-made paper $[PSS/ITO]_1$ showed a noticeable trend to form a semicircular curve in the impedance Nyquist plot. In addition, the more bilayers of $[PSS/ITO]_n$ coated onto the cellulose fibers, the smaller the diameter of the semicircle became. The paper $[PSS/ITO]_5$ exhibited a perfect semicircle, indicating that it was fully DC conductive. As shown in Figure 6.8(b), the impedance Nyquist plot of fiber $[PSS/ITO]_{10}$ also showed a complete semicircle, which indicates the presence of DC conductance in this single fiber. The actual magnitude of the DC resistance is much larger than that of the handsheet containing many of these single fibers because of the small dimensions of one single fiber.

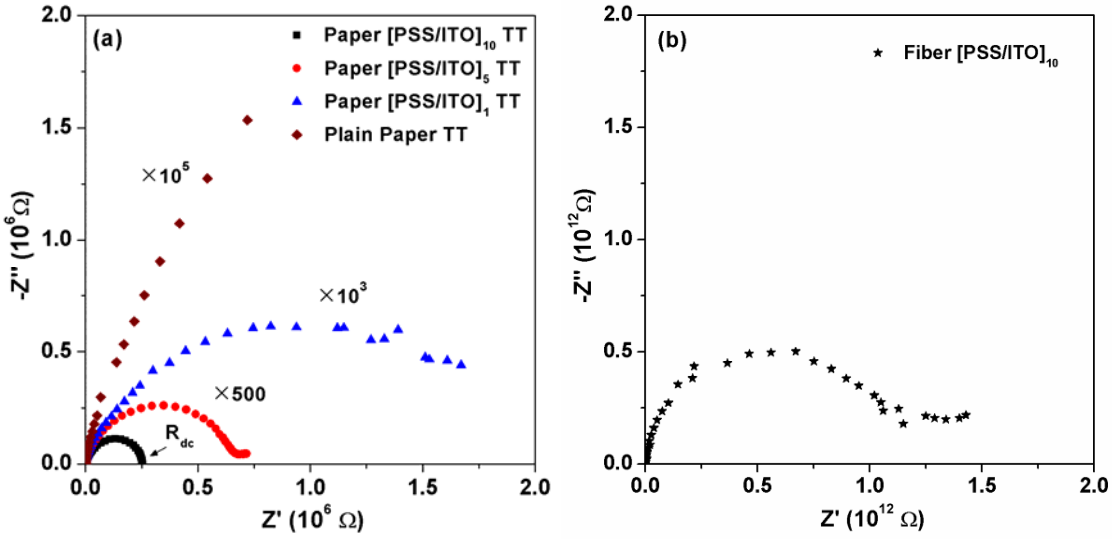

Figure 6.8 Impedance Nyquist plot of (a) plain paper and papers $[PSS/ITO]_1$, paper $[PSS/ITO]_5$, and paper $[PSS/ITO]_{10}$ measured along the TT direction, and (b) fiber $[PSS/ITO]_{10}$. The data of plain paper, paper $[PSS/ITO]_1$, and paper $[PSS/ITO]_5$ had to be suppressed by 10^5, 10^3 and 500 times respectively in order to be shown on the same complex plane graph as that of $[PSS/ITO]_{10}$.[63]

The paper AC conductivity (σ_{ac}) along the TT direction was calculated using equation (2.3), and the conductivity Bode plots are shown in Figure 6.9. As shown in the figure, the dependence of the σ_{ac} on the frequency can be divided into two regions: one is

the frequency independent region at the relatively low frequency range, the other one is the frequency dependent region at the relatively high frequency range. The frequency at which the conductivity response changed from frequency dependent to independent region is called the critical frequency. From the frequency independent region, one can derive the DC conductivity (σ_{dc}) of the materials. The σ_{dc} of all of the samples measured along both the IP and the TT directions are shown in Table 6.1. It can be seen from the table that the conductivity of paper made from fibers coated with ITO increases drastically when the number of bilayers increases. The σ_{dc} of paper $[PSS/ITO]_{10}$ are 1.9×10^{-8} S/cm and 5.2×10^{-6} S/cm in the TT and the IP directions, respectively. Compared to the conductivity of the plain paper, it was increased by more than six orders of magnitude in both cases. Therefore, when more ITO nanoparticles were deposited onto the cellulose fibers, the paper became more conductive. In the meantime, the frequency dependent region got smaller and smaller when the paper became more and more conductive. In addition, the response of the σ_{ac} of the plain paper was completely dominated by the frequency dependent region, and this means that the plain paper is completely insulating.

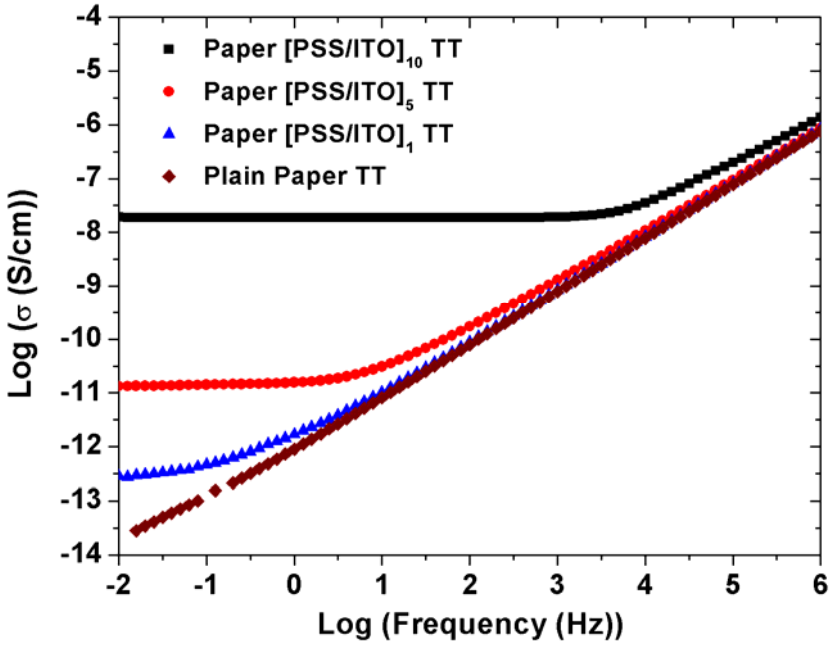

Figure 6.9 AC conductivity (σ_{ac}) of plain paper, paper $[PSS/ITO]_1$, paper $[PSS/ITO]_5$, and paper $[PSS/ITO]_{10}$ measured in the TT direction.[63]

Table 6.1 The electrical results of all paper sheets measured along both the in-plane and through-the-thickness directions.[63]

Paper Sample	Electrical Properties			
	R_{dc} (Ω)		σ_{dc} (S/cm)	
	TT	IP	TT	IP
Plain paper [a]	$> 3.0\times10^{11}$	$> 5.12\times10^{12}$	$< 2.8\times10^{-14}$	$< 2.5\times10^{-11}$
$[PSS/ITO]_1$ [b]	$\sim 1.8\times10^{10}$	$\sim 1.2\times10^{12}$	2.8×10^{-13}	3.2×10^{-11}
$[PSS/ITO]_5$	3.3×10^{8}	3.6×10^{10}	1.3×10^{-11}	1.6×10^{-9}
$[PSS/ITO]_{10}$	2.5×10^{5}	1.9×10^{7}	1.9×10^{-8}	5.2×10^{-6}

[a] The plain paper is completely insulating so that an exact R_{dc} and σ_{dc} cannot be obtained (values shown were estimated from data taken at 0.01 Hz). [b] The impedance semicircle curve of paper $[PSS/ITO]_1$ is not fully finished, so that the its R_{dc} is estimated by standard semicircle fitting.

The σ_{ac} of paper $[PSS/ITO]_{10}$ along both the IP and TT directions are shown in Figure 6.10. As shown in the figure, the conductivity along the IP direction is about 2-3 orders of magnitude higher than that of the same paper measured in the TT direction. This is observed not only for the ITO coated papers but also the plain paper (Table 6.1). For example, as shown in Figure 6.10(a), the critical frequencies for paper $[PSS/ITO]_{10}$ measured in the two directions are virtually the same. However, the magnitude of σ_{dc} for this paper in the IP and the TT directions are significantly different by more than two orders of magnitude. It can be concluded that this difference may be related to the anisotropic structure of the paper handsheet (Figure 6.10(b)). According to the SEM image on top of the paper handsheet (Figure 6.10(c)) and the cross-sectional image (Figure 6.10(d)), all of the cellulose fibers aligned along the paper plane and then they stacked up in the TT direction. This indicates that the conduction in the IP direction is expected to occur more along the fibers; however, the conduction in the TT direction is more along the contact regions between the fibers. In other words, a good fiber-to-fiber connection is more crucial for samples measured in the TT direction than that in the IP direction. This is why the conductivity of paper along the IP direction is two-orders-of-magnitude higher than that along the TT direction.

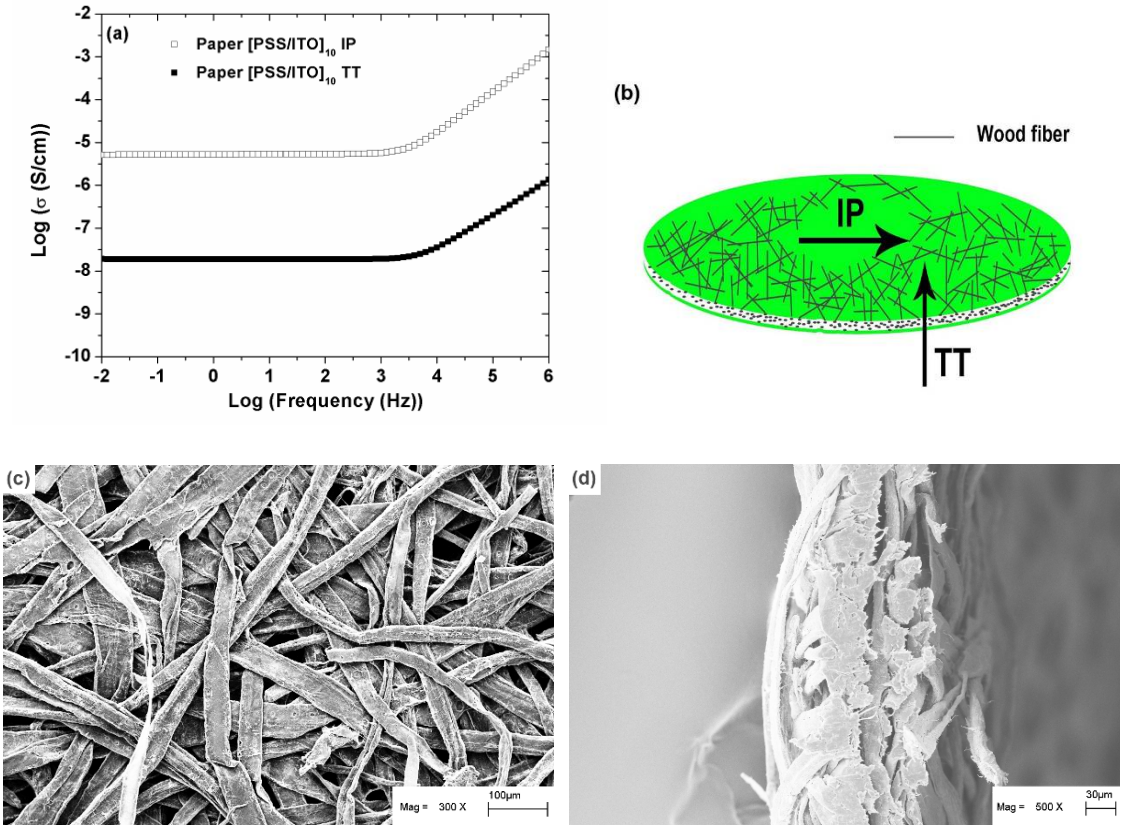

Figure 6.10 (a) Anisotropic conductivity of paper $[PSS/ITO]_{10}$ measured along the IP and TT directions, (b) Schematic of paper indicating electrical measurement directions, (c) and (d) SEM images of the handsheet taken from the in-plane and the cross sectional area, respectively.[63]

6.3.4. Conductive-AFM Imaging

Conductive-AFM analysis was carried out on the paper $[PSS/ITO]_{10}$, in order to confirm the presence of the percolation pathways resulting from the interconnected network of ITO nanoparticles in the paper. As shown in Figure 2.6, a bias voltage was applied underneath the paper, and the AFM tip was used to detect the current from the top of the paper. The presence of the percolation paths can be evaluated from the presence of the current detected. Since the scanning area of the AFM image (maximum 45 μm) is comparable to or smaller than the dimension of individual fibers (~ 40 μm), only one

single fiber was selected under the scanning probe microscope to perform Conductive-AFM analysis.

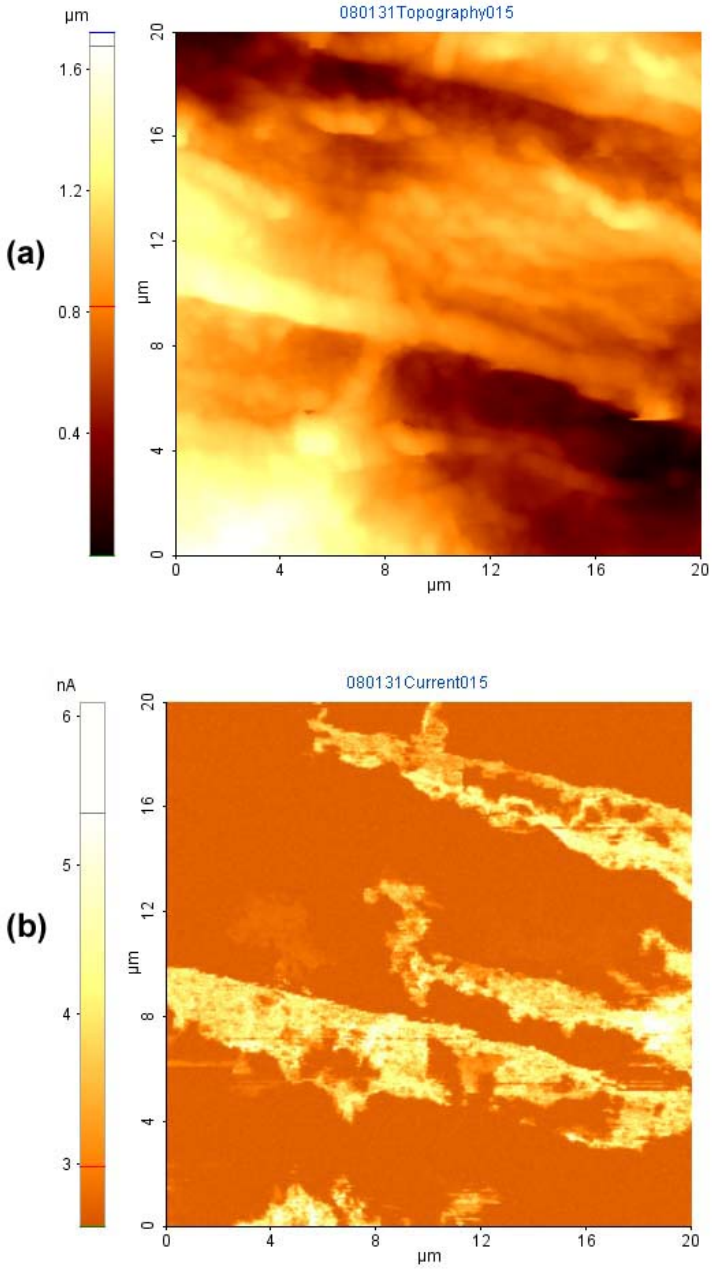

Figure 6.11 The conductive-AFM (a) topography image and (b) current image of paper $[PSS/ITO]_{10}$. The scanning area is 20 × 20 µm on the surface of one selected single fiber.[63]

As shown in the AFM topography image in Figure 6.11(a), aggregates of ITO particles can be found in some regions on the fiber surface, and substantial current (~5 nA) is detected in the corresponding regions in the current image (Figure 6.11(b)). The detected current is the current that percolated through the thickness of the paper and represents the end of the percolation paths. Furthermore, the percolated conductive paths on ITO-coated fibers is in perfect agreement with the SEM images (Figure 6.7(a) and (b)), both in terms of the shape and dimension of the percolated network.

6.3.5. Effect of Modification of the ITO Suspensions on Conductive Paper

In order to compare the effect of modification of the ITO suspensions using PEI, another paper was prepared using PEI-ITO at the PEI:ITO ratio of 1:200. The cellulose fibers were coated with five bilayers of PSS and PEI-ITO, and the samples were denoted as $[PSS/PEI\text{-}ITO]_5$. The electrical properties and the ITO content of this paper is compared to the paper $[PSS/ITO]_5$.

6.3.5.1. Effect of Modification on the Electrical Properties

The effect of PEI modification of ITO nanoparticles on the electrical properties of as-prepared papers was studied. As shown in Figure 6.12, the σ_{dc} of paper $[PSS/(PEI\text{-}ITO)]_5$ and paper $[PSS/ITO]_5$ are 3.6×10^{-9} and 2.1×10^{-11} S/cm in the TT direction, respectively. The σ_{dc} of paper $[PSS/(PEI\text{-}ITO)]_5$ is more than two-orders-of-magnitude higher than that of paper $[PSS/ITO]_5$. This improvement indicates that many more ITO nanoparticles were coated onto the cellulose fibers from the PEI-ITO suspension that that from the unmodified ITO suspensions. However, the σ_{dc} of paper $[PSS/ITO]_{10}$ and $[PSS/(PEI\text{-}ITO)]_{15}$ are the same to each other. In other words, the deposition of 15 bilayers of PSS and PEI-ITO on cellulose fibers does not render a paper that is more conductive than that made from the cellulose fibers that were coated

with 10 bilayers of PSS and ITO. Therefore, it is believed that the optimal conductivity of the paper under current condition along the TT directions is around 1.9×10^{-8} S/cm.

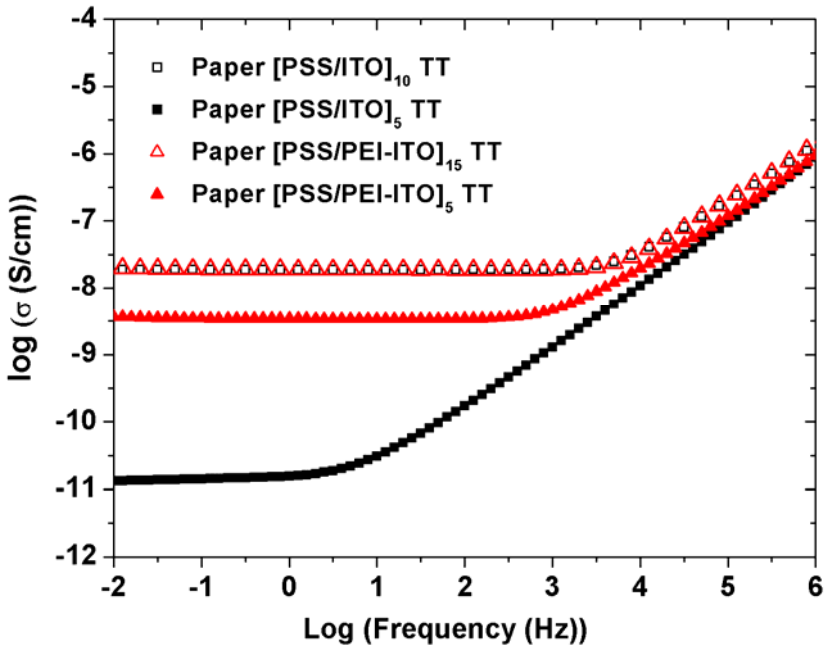

Figure 6.12 The σ_{ac} of paper $[PSS/ITO]_{10}$, paper $[PSS/ITO]_5$, paper $[PSS/PEI\text{-}ITO]_{15}$, and paper $[PSS/PEI\text{-}ITO]_5$.

6.3.5.2. Effect of PEI Modification on the Remnant ITO Content

The amount of ITO nanoparticles in both kinds of paper was evaluated by measuring the remnant char fraction using TGA analysis in flowing air. As shown in Figure 6.13, the ITO content in paper $[PSS/(PEI\text{-}ITO)]_5$ was determined to be almost double that in paper $[PSS/ITO]_5$ (8.17 wt% vs. 4.55 wt%). Therefore, this indicates that nearly twice the number of ITO particles was coated onto cellulose fibers from the PEI-modified ITO suspension than that from the unmodified ITO suspension.

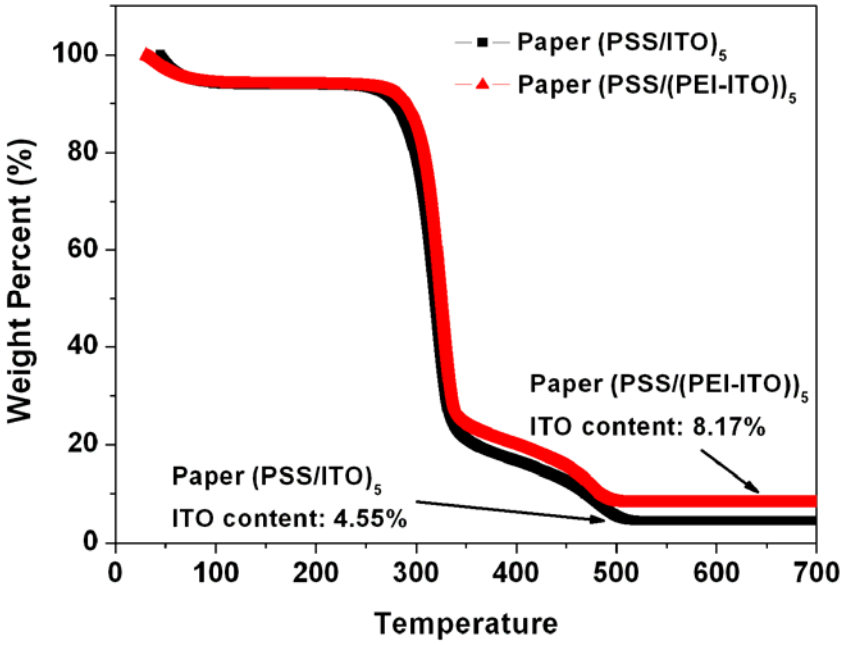

Figure 6.13 TGA thermogram of paper $[PSS/ITO]_5$ and paper $[PSS/(PEI-ITO)]_5$ from room temperature to 700°C. The remnant ITO particles in paper $[PSS/ITO]_5$ and paper $[PSS/(PEI-ITO)]_5$ are 8.17% and 4.55% respectively.[118]

6.4. Conclusions

Conductive paper was successfully fabricated by LbL assembly of semiconductive ITO nanoparticles onto cellulose fibers, and manufacturing these ITO-coated fibers into paper handsheets through conventional papermaking methods. The ITO nanoparticles were found to aggregate and form percolated networks on the cellulose fibers. This locally percolated network on the fibers translates into conductive percolation paths throughout the whole paper. The conductivity of as-prepared papers drastically increases when several bilayers of PSS and ITO are coated onto the wood fibers. Compared to plain paper made from virgin fibers, the conductivity of coated paper is improved by more than six orders of magnitude in both the in-plane and through-the-thickness directions. The optimal conductivity was obtained when 10

bilayers of PSS and ITO were coated onto the fibers. The σ_{dc} of paper $[PSS/ITO]_{10}$ was 5.2×10^{-6} S/cm and 1.9×10^{-8} S/cm in the IP and the TT directions, respectively. The conductivity of all papers in the IP direction was found to be 2-3 orders of magnitude higher than that in the TT direction. This is believed to be related to the anisotropic structure of paper handsheets.

The modification of ITO suspension by using PEI will significantly improve the deposition rate of ITO onto cellulose fibers. The conductivity of paper $[PSS/PEI\text{-}ITO]_5$ is more than two orders of magnitude higher than that of paper $[PSS/ITO]_5$. Furthermore, due to the increased assembly rate, the ITO content in the paper $[PSS/PEI\text{-}ITO]_5$ is two times higher than that of paper $[PSS/ITO]_5$. However, further increase the assembly bilayers on the cellulose fiber will make the difference of conductivity between the paper made from unmodified ITO nanoparticles and the paper made from PEI-modified ITO nanoparticles smaller. Both the paper $[PSS/ITO]_{10}$ and $[PSS/PEI\text{-}ITO]_{15}$ reaches the same conductivity value of 1.9×10^{-8} S/cm along the TT direction and 5.2×10^{-6} along the IP direction, indicating these conductivities is the optimal conductivity under the current conditions.

CHAPTER 7

FABRICATION OF CONDUCTIVE TRANSPARENT THIN FILMS

7.1. Introduction

Transparent conductive oxide thin films, such as ITO films, have long been used for manufacturing transparent conductive electrodes for optoelectronic devices, such as flat-panel displays, thin film solar cells, and touch screens.[23, 24] Traditionally, ITO thin films are fabricated by using sputter coating,[172-174] evaporation,[175, 176] chemical vapor deposition (CVD),[177] or sol-gel methods.[178] Using these processes, researchers are able to fabricate ITO thin films with high conductivity (~ 10^4 S/cm) and high transparency[23]. However, most of these techniques have the disadvantage of material that they waste ITO due to the naturally multidirectional deposition method and the poor target utilization.[24]

This chapter demonstrates that transparent conductive ITO thin films can also be fabricated by using the LbL assembly method. Due to the simplicity of this method, LbL assembled ITO thin films can be fabricated onto various substrates, including plastic films, glass, and silicon wafers. Furthermore, this method can also be applied onto substrates with irregular surfaces.

7.2. Experimental Procedure

In this chapter, silicon wafers and the ordinary write-on transparencies (Office Depot) were used as the substrate for depositing the transparent conductive $[PSS/ITO]_{10}$ thin films. The electrical properties, optical properties, and film structure were characterized by four-probe electrical measurements, UV/Vis spectroscopy, and AFM.

7.2.1. LbL Assembly Procedure

The LbL assembly of $[PSS/ITO]_{10}$ thin films followed the same procedure that was described in Chapter 2. The silicon wafers and the transparencies were pretreated prior to the LbL assembly. The silicon wafers were cleaned by sonicating the wafer first in acetone and then in isopropanol for 10 min. The transparency was cleaned by wiping the transparency with isopropanol, and then activating the surface in UV/Ozone (Novascan, PSD Pro-UV) at 50 °C for 15 min.

During the LbL assembly, only one bilayer of PEI and PSS was assembled as the precursor layer on each substrate prior to the assembly of ITO nanoparticles. The concentration of PEI solution, PSS solution, and ITO suspension was 0.02, 0.02, and 0.1 wt%, respectively. The pH of the PEI solution, PSS solution, and ITO suspension was 5, 2.9, and 2.9, respectively.

In this chapter, two hybrid films were fabricated on transparencies to evaluate the transmittance of the thin films. Two other films were fabricated on silicon wafers to evaluate the film structure, to measure film thickness, and to evaluate the film conductivity. The LbL assembly conditions of these four films are listed in Table 7.1.

Table 7.1 Summary of the LbL assembly conditions of the hybrid thin films $[PSS/ITO]_{10}$ and $[PSS/PEI/PSS/ITO]_{10}$.

Sample	Film composition	LbL assembly procedure		Substrate
Sa-1	$[PSS/ITO]_{10}$	PSS (5 min, w.o. NaCl)	ITO (20 min)	Transparency
Sa-2	$[PSS/ITO]_{10}$	PSS (5 min, 0.1M NaCl)	ITO (20 min)	Transparency
Sa-3	$[PSS/ITO]_{10}$	PSS (10 min, 0.1M NaCl)	ITO (20 min)	Silicon wafer
Sa-4	$[PSS/PEI/PSS/ITO]_{10}$	PSS (10 min, 0.1M NaCl)	ITO (20 min)	Silicon wafer

7.2.2. Transmittance Measurement

The transmittance of the ITO thin films on transparency was evaluated using UV/Vis/NIR spectrophotometer (Beckman DU-640) at wavelengths ranging from 200 to 1100 nm. The transmittance of all ITO film samples were compared with that of the plain transparency substrate. All of the transmittance measurement were evaluated using air as the background.

7.2.3. Four-probe Electrical Measurement

The electrical properties of conductive thin films on both transparency and silicon wafers were evaluated using four-probe electrical measurements. This technique was preferred over two probe technique for thin film measurement because it can eliminate the influence of the contact resistance. As shown in Figure 7.1, four probes with the same probe distance were made to contact with the conductive film. During the measurement, a direct current was applied through the outer two probes, and the voltage was measured through the inner two probes. The measurement was done in a sweep mode, in which the current was swept from 0 to a designated current, and the voltage was measured. The surface resistance (R_{sh}) was calculated using equation (7.1),[179] and its common unit is "Ω/sq". In equation (7.1), I is the applied current through the outer two probes, and V is the measured voltage through the inner two probes. In addition, the bulk conductivity (σ) and the bulk resistivity (ρ) can be calculated using equation (7.2),[179] in which t is the thickness of the thin films.

$$R_{sh} = 4.53\frac{V}{I} \qquad (7.1)$$

$$\sigma = 1/\rho = 1/R_{sh}t \qquad (7.2)$$

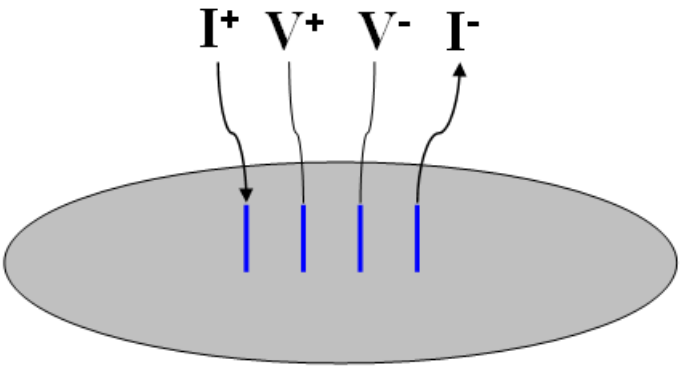

Figure 7.1 Schematic of the setup of four-probe electrical measurement.

7.2.4. Film Thickness Measurement by AFM

In order to obtain the conductivity of the thin films, one has to measure the film thickness (*t*). In this chapter, the film thickness of the thin films on silicon wafers was evaluated using AFM. One small scratch was made on the film using tweezers, and the AFM was used to measure the film thickness over this scratch. This procedure is similar to the one used in Chapter 5.

7.3. Results and Discussion

7.3.1. Transmittance of the ITO Films Deposited on Transparencies

The transmittance of the ITO films deposited on the transparencies is shown in Figure 7.2. As shown in the figure, the plain substrate is not transparent in the UV region (200 to 390 nm[180]), but it is quite transparent in the visible range (390 to 750 nm[180]) and the near infrared (NIR) range (750 to 1100 nm[180]). The transmittance of the plain substrate in the UV region is close to zero, but that in the visible and NIR range is close to 90%. The close-to-zero transmittance of the plain substrate in the UV region can be attributed to the strong light absorption by the band gap.[31] Similar to the plain substrate, the transmittance of ITO thin films on the substrate in the UV region is also close to zero,

due to the light absorption from both the substrate and the ITO films. In the visible range, the transmittance of ITO thin films on the substrate is lower than that of the plain substrate. For example, the transmittance of Sa-1 and Sa-2 at 550 nm is 78% and 70 %, respectively. This value is lower than that of the plain substrate, which is 88% at 550 nm.

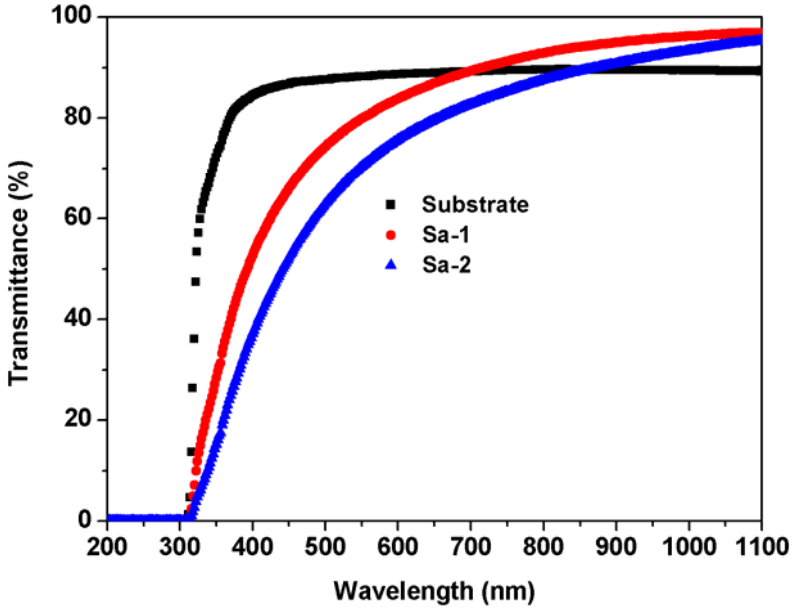

Figure 7.2 Transmittance of transparent plastic substrate and ITO thin films Sa-1 and Sa-2 for the wavelength range from 200 to 1100 nm.

The transmittance of Sa-1 is slightly higher than that of Sa-2. This is probably due to the rougher interface between the PSS and ITO layers, when the PSS was assembled at a higher ionic strength.[75, 148] In addition, the transmittance of both Sa-1 and Sa-2 increases as the wavelength increases. For example, the transmittance of Sa-1 and Sa-2 at 390 nm is 47% and 33%, respectively. On the other hand, the transmittance of Sa-1 and Sa-2 increased to 89% and 85% at 750 nm, respectively. The transmittance of both Sa-1 and Sa-2 further increased in the NIR range, and it is eventually higher than that of the plain substrate. For example, the transmittance of Sa-1 and Sa-2 surpassed the transmittance of the plain substrate at around 760 nm and 860 nm respectively. At the 1100 nm, the transmittance of Sa-1 and Sa-2 is respectively 96% and 95%, both of which

are substantially higher than that of the plain substrate (89%). The higher transmittance of the ITO thin films than the plain substrate can be a result of the antireflection of the thin films.[181, 182] It has been observed that porous films from colloidal SiO_2 particles can give rise to a higher transparency at a wavelength range that is four times larger than the film thickness due to the antireflection. Due to the decreased reflection, more light will be transmitted through the film, and thus the transmittance of the hybrid films on substrate will be increased.

7.3.2. Surface Structure and Film Thickness

In order to evaluate the thickness of $[PSS/ITO]_{10}$ thin films using AFM, Sa-3 and Sa-4 were prepared on silicon wafers. As shown in Figure 7.3, part of the thin films was scratched off using tweezers, and the height difference between the top of the film and the substrate was measured by AFM to evaluate the thin film thickness. The thickness was taken by averaging multiple points from a sufficiently large scanning area (20 μm × 20 μm). As shown in the figure, the average film thickness of Sa-3 $[PSS/ITO]_{10}$ is around 196 nm. This value was used for Sa-1 and Sa-2 to calculate their conductivity using equation (7.1) and (7.2), since the thin films Sa-1, Sa-2, and Sa-3 have similar film compositions. The average film thickness of Sa-4 $[PSS/PEI/PSS/ITO]_{10}$ is about 235 nm, thicker than that of the Sa-3. The thicker film of Sa-4 may be a result of the extra polyelectrolyte layers in every $[PSS/PEI/PSS/ITO]_n$ bilayer that are absent in every $[PSS/ITO]_n$ bilayer.

The surface structure of Sa-3 and Sa-4 was also characterized by AFM. As shown in Figure 7.4, both of the Sa-3 and Sa-4 films fully cover the substrate surface. Both of the films Sa-3 and Sa-4 exhibit a raspberry-like nanometer structure with a surface roughness of 66 and 61 nm in the 5 μm × 5 μm area, respectively. This structure can thus be potentially made into superhydrophobic transparent conductive thin films by surface

treating the structure with low surface energy material.[181] The thin film thickness, surface roughness, and the conductivity of these films are also summarized in Table 7.2.

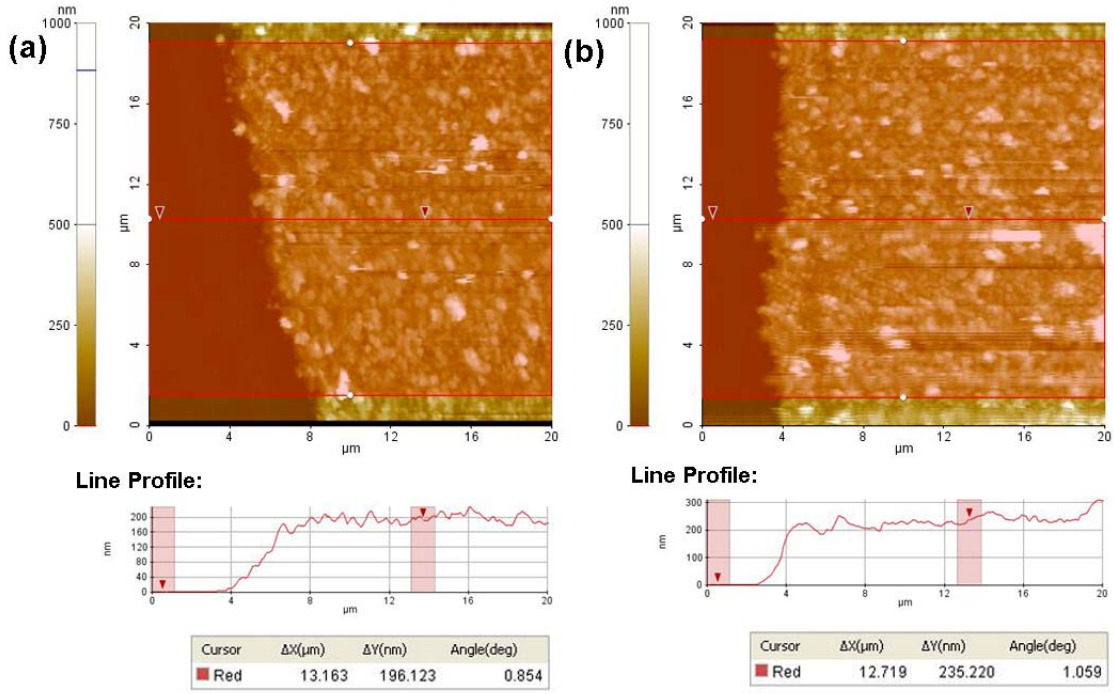

Figure 7.3 Thickness measurement of the (a)Sa-3 $[PSS/ITO]_{10}$ and (b)Sa-4 $[PSS/PEI/PSS/ITO]_{10}$ films on silicon wafers. Both of the AFM images were taken from a 20 μm × 20 μm area, and both of the height scales are set to the same scale of 0 to 1000 nm for easy comparison.

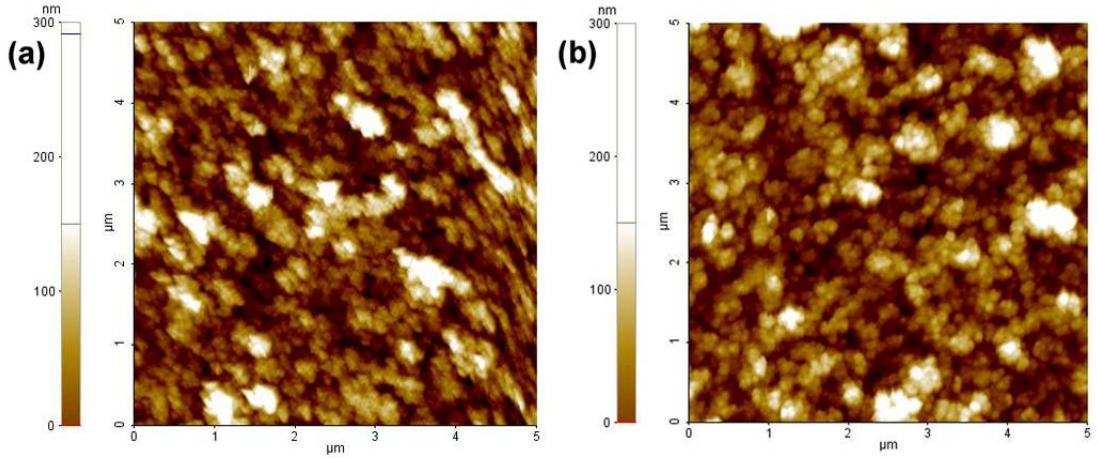

Figure 7.4 AFM surface topography of ITO thin films (a)Sa-3 $[PSS/ITO]_{10}$ and (b)Sa-4 $[PSS/PEI/PSS/ITO]_{10}$ on silicon wafers. All of the images are in a size of 5 μm × 5 μm, and the height scales are set to the same scale of 0~300 nm. The surface roughness of the thin films in 5 μm × 5 μm area is (a) 66 nm and (b) 61 nm, respectively.

Table 7.2 Summary of the film structure, thickness, and the conductivity of the thin films listed in Table 7.1.

Sample	Thickness (nm)	Surface Roughness [b] (nm)	Conductivity (S/cm)
Sa-1	196[a]	56	$1.15 \pm 0.07 \times 10^{-4}$
Sa-2	196[a]	66	$1.29 \pm 0.05 \times 10^{-4}$
Sa-3	196	66	$1.10 \pm 0.19 \times 10^{-4}$
Sa-4	235	61	$6.43 \pm 0.21 \times 10^{-5}$

[a] The film thickness of Sa-3 was used as the thickness of Sa-1 and Sa-2 for the calculation of film conductivity. This approximation is proved to be close enough by AFM imaging.
[b] Surface roughness is obtained from the AFM images of thin film in the 5 μm × 5 μm area.

7.3.3. Electrical Properties

The electrical conductivity of all of the ITO thin films was evaluated using the four-probe electrical measurement, and calculated using equations (7.l) and (7.2). The current was applied to the film by sweeping the current from 0 to 100 nA, and the voltage response was recorded. All of the thin films exhibited a linear response to the sweeping current, which means the thin films are DC conductive.

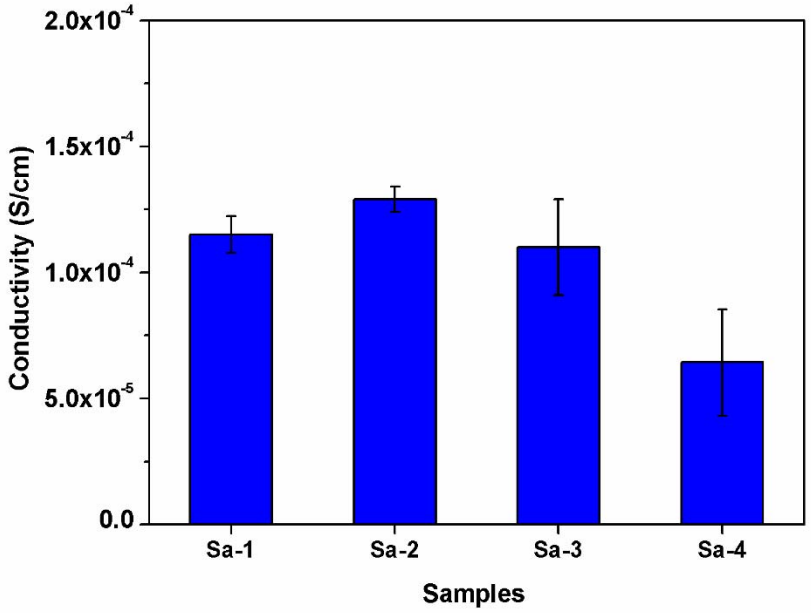

Figure 7.5 Conductivities of ITO thin films listed in Table 7.1.

As shown in Figure 7.5 and Table 7.2, the conductivity of thin films Sa-1, Sa-2, and Sa-3 are very close to each other. This result is reasonable, since all of these three films have similar film composition, except for the slightly different LbL assembly conditions (Table 7.1). Compared to the thin film $[PSS/ITO]_{10}$ (Sa-1, Sa-2, and Sa-3), the conductivity of thin film $[PSS/PEI/PSS/ITO]_{10}$ (Sa-4) decreased almost by half. This indicates that the number of insulating polyelectrolyte layers between the ITO assembly layers is critical for the electrical conductivity of the LbL assembled ITO thin films. One extra bilayer of PEI/PSS between every PSS and ITO layers decreased the electrical conductivity of thin film from $1.10 \pm 0.19\times10^{-4}$ to $6.43 \pm 0.21\times10^{-5}$ S/cm. It is to be noted that the conductivity of these films is much lower than that of the sputtered ITO thin film (over 10^3 S/cm[33]). However, it is possible to increase the conductivity of these films by post-deposition heat treatment.

7.4. Conclusions

In this chapter, a new method to prepare transparent conductive thin films was demonstrated by LbL assembly of $[PSS/ITO]_n$ thin films on ordinary write-on plastic transparencies. These thin films exhibited fairly high transparency in the visible range (~ 80% at 550 nm). Surprisingly, in the NIR range, they exhibited a higher transmittance than the plain substrate, which can be attributed to the antireflection of the thin films. The thin films exhibited a raspberry-like nanometer scale structure, and they can be potentially made into superhydrophobic films. The electrical conductivity of the thin films without any treatment is around 10^{-4} S/cm. It was found that the polyelectrolyte content in the thin film is critical for the film conductivity.

CHAPTER 8

CONCLUSIONS AND SUGGESTIONS FOR FUTURE WORK

8.1. Conclusions

In this thesis, several aspects of the fundamentals of the layer-by-layer (LbL) assembly of hybrid bicomponent thin films, which was composed of one polyelectrolyte material and one inorganic nanoparticle material, were studied. The inorganic nanoparticles studied in this work were primarily indium tin oxide (ITO) nanoparticles. The fundamental understanding of this process was applied to prepare conductive paper and transparent conductive thin films using conductive ITO nanoparticles.

ITO colloidal suspensions prepared from commercial ITO nanoparticles for the LbL assembly were not very stable, and the LbL assembly rate was low. In this work, a simple method was developed to stabilize the ITO suspension by modifying the ITO particle with PEI, and the LbL assembly rate of the $[PSS/ITO]_n$ thin films could be enhanced by two times at an appropriate PEI:ITO ratio. This LbL assembly rate enhancement was attributed to the stronger particle-surface interaction forces, a larger number of interaction sites between PEI-modified ITO with the PSS layers, as well as the weaker interparticle repulsive forces between the PEI-modified ITO nanoparticles.

Prior to the LbL assembly of hybrid thin films on a substrate, a polyelectrolyte precursor layer was often assembled on the substrate to reduce the substrate effect and render uniformly charged substrate surfaces. In this thesis, the effect of a precursor layer consisting of $[PEI/PSS]_4$ on the assembly of hybrid thin films $[ITO/PSS]_{9.5}$ was examined in detail. It was found that the precursor layer could significantly affect the initial "recovery regime" of the assembly process of the hybrid thin films by changing the surface charge of the precursor layer, but it did not affect the second "linear growth

regime" of the assembly process. The ionic strength in the PSS solutions could affect the film buildup rate from the PEI-modified ITO nanoparticles, but it did not affect that from the unmodified ITO nanoparticles. This distinction was attributed to the polymer-polymer interaction between the PEI-modified ITO and the PSS layers, which is affected significantly by the ionic strength of the PSS solutions.

Exponentially grown LbL (*e*-LbL) films are desirable because this method can increase the growth rate considerably, resulting in much thicker films in a shorter period of time than normally linearly grown LbL (*l*-LbL) thin films. For the first time, a new type of *e*-LbL grown bicomponent hybrid thin films was demonstrated by LbL assembly of PEI and SiO_2 nanoparticles. It was shown that this *e*-LbL growth process was significantly dependent on the pH of the PEI and the SiO_2 solutions, the ionic strength of the PEI solutions, as well as the substrate used. The *e*-LbL growth will only occur when the film is deposited with PEI at a high pH and SiO_2 at a low pH. The *e*-LbL films could grow to thicknesses as large as 1-3 μm within just 10 bilayers. These *e*-LbL thin films were primarily composed of inorganic materials (over 90 wt% as determined by TGA). Having mostly nanoparticles is highly desirable for the thin films whose photonic, electronic and optical properties are strongly dependent on the connectivity of the nanoparticles.[21] It is worth noting that thin films $[PAA/PEI\text{-}ITO]_n$ that were assembled from PAA at a low pH and PEI-modified ITO at a high pH also exhibited weak exponential growth behavior.

A new process to prepare conductive paper was developed by LbL assembly of $[PSS/ITO]_n$ thin films onto individual cellulose fibers prior to papermaking. These ITO-coated cellulose fibers could be used to manufacture conductive paper using traditional papermaking methods. It was found that the conductivity of the paper was drastically increased when several bilayers of PSS and ITO were deposited onto the cellulose fibers. Compared to plain papers, the conductivity of the paper was increased by more than six orders of magnitude when 10 bilayers of PSS and ITO were deposited onto

the cellulose fibers. The conductivity of all papers measured along the in-plane (IP) direction were found to be 2-3 orders of magnitude higher than those measured along the through-the-thickness (TT) direction, which was believed to be related to the anisotropy of the paper structures. Due to the higher assembly rate, the conductivity of the paper made from PEI-modified ITO was two orders of magnitude higher than that of the paper made from unmodified ITO.

A new method to prepare transparent conductive ITO thin films on plastic substrates was developed by LbL assembly of PSS and ITO. The thin films exhibited fairly high transmittance in the visible range (~ 80% at 550 nm), and a surprisingly higher transmittance in the NIR range that was higher than the substrate. This phenomenon was attributed to the antireflection of the thin films. The electrical conductivity of the thin film was around 10^{-4} S/cm without any heating treatment.

8.2. Suggestions for Future Work

8.2.1. Conductive Thin Films from Monodispersed ITO Nanoparticles

In this work, it was found that the stability of the ITO suspension was poor, and it was hard to study effect of the ionic strength of the ITO colloidal suspensions, because the commercially available ITO nanoparticles were polydispersed. Previous to the work presented in this thesis, monodispersed ITO nanoparticles with very small particle size (~ 7 nm) have been successfully synthesized in our lab.[183, 184] It would be very interesting to study the LbL assembly process of the monodispersed ITO nanoparticles in the near future.

It should be noted that these monodispersed ITO nanoparticles are prepared in organic solvents, and the ITO colloidal suspensions are normally stabilized by hydrophobic stabilizing agents.[183, 184] It is thus critical to disperse these ITO nanoparticles into an aqueous solvent for the electrostatic LbL assembly process. This

can be achieved either by synthesizing the colloidal particles with hydrophilic stabilizing agents [185-188] or by switching the stabilizing agents from the hydrophobic molecules to hydrophilic molecules using the place exchange methods.[189-192]

It would be very interesting to study the effect of ionic strength in the ITO suspensions, and the kinetics of the ITO assembly process by using the monodispersed ITO nanoparticles.

8.2.2. Temperature Amplified *e*-LbL growth of Conductive Thin Films

In chapter 5, it has been shown that $[PAA(2.2)/PEI\text{-}ITO(7)]_n$ exhibited a weak *e*-LbL growth process. The small exponential "growth strength" of this system was attributed to the hindered diffusion of PAA due to the using of PEI-modified ITO nanoparticles and the large particle size of commercially available ITO particles. It would be very interesting to further pursue the *e*-LbL growth of this thin film due to the special properties of ITO nanoparticles. One of the possible directions is to amplify the exponential "growth strength" by performing the LbL growth at elevated temperatures (e.g. at 50 °C). It has been shown that the traditional *l*-LbL thin film $[PDDA/PSS]_n$ undergo exponential growth at elevated temperatures.[108] Therefore, it maybe possible to amplify the diffusion of PAA during the LbL assembly to amplify the exponential growth of the $[PAA(2.2)/PEI\text{-}ITO(7)]_n$ films. In addition, it would be even more promising to study the exponentially grown thin films of ITO by using monodispersed ITO nanoparticles.

8.2.3. Self-assembly of Multifunctional Thin Films

In Chapter 5, it was found that the film buildup rate can be significantly amplified by adjusting the pH of the PEI solutions and the SiO_2 suspensions. In addition, the thin film $[PEI(4.7)/SiO_2(9.5)]_{10}$ showed a very interesting surface structure. As shown in Figure 8.1 at four different magnification of the same film, the surface of thin film

$[PEI(4.7)/SiO_2(9.5)]_{10}$ exhibited a self-organized cluster-like structure. The cluster domain is approximately 300 to 400 nm, and each cluster is composed of many smaller SiO_2 nanoparticles. In other words, this thin film structure is a very interesting cluster structure with nanometer roughness. This special structure can be potentially used to prepare antireflective superhydrophobic thin films.

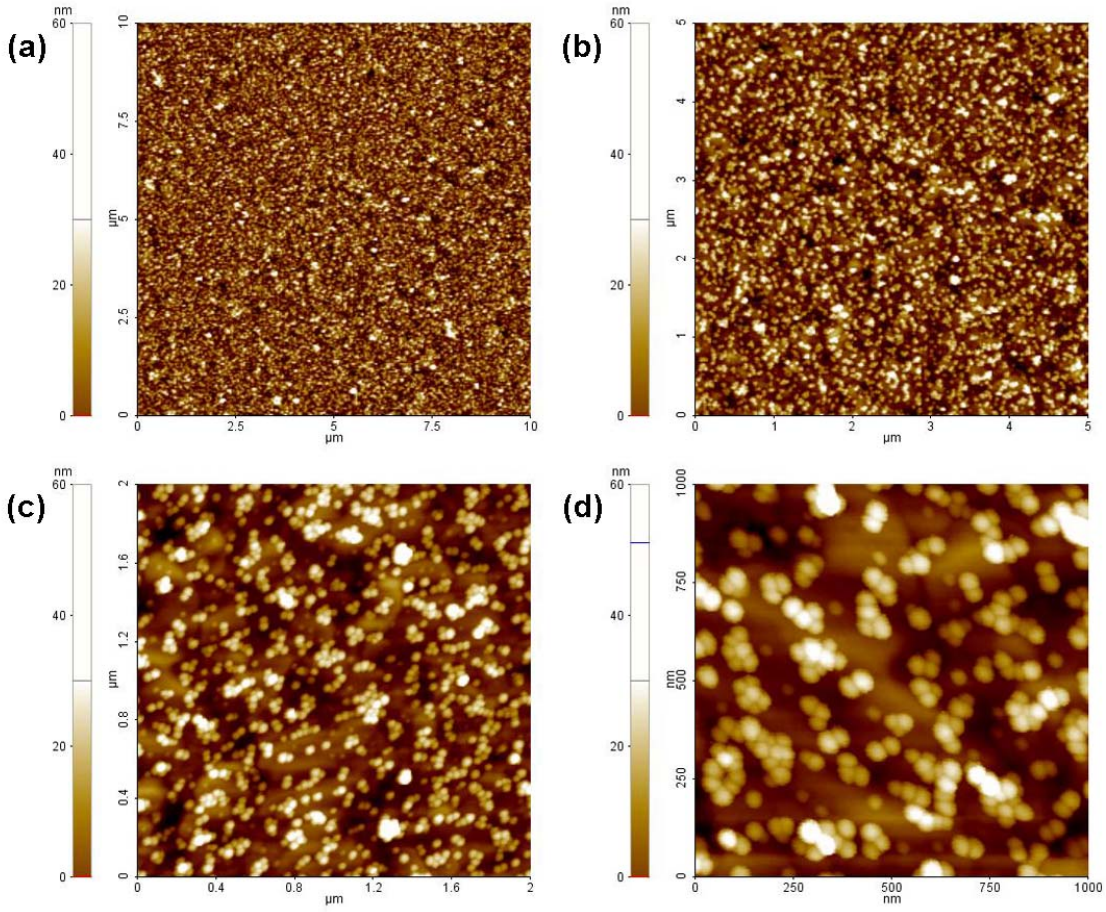

Figure 8.1 AFM image of thin film $[PEI(4.7)/SiO_2(9.5)]_{10}$ at different scales: (a) 10 μm × 10 μm, (b) 5 μm × 5 μm, (c) 2 μm × 2 μm, and (d) 1 μm × 1 μm.

In the silicon research area, investigators have put a lot of efforts on fabricating cone-shape structures on the silicon wafers using lithography or etching methods.[14, 193-195] It would be very promising to prepare such a structure using self-assembly methods. One of the advantages of using this method to prepare the antireflective

structure is that the cluster size can be easily tuned by changing the pH of the PEI solutions and the SiO_2 suspensions. Furthermore, it has also been shown that superhydrophobic surfaces could be easily prepared from SiO_2 by coating the surface with organic molecules with low surface energy.[181, 182, 196]

REFERENCES

[1] Decher, G., "Polyelectrolyte Multilayers, an Overview", in *Multilayer Thin Films: Sequential Assembly of Nanocomposite Materials*, Decher, G., Schlenoff, J. B., Wiley-VCH, Weinheim **2003**.

[2] Decher, G., "Fuzzy nanoassemblies: Toward layered polymeric multicomposites", *Science* **1997**, *277*, 1232.

[3] Decher, G., Hong, J. D., "Buildup of ultrathin multilayer films by a self-assembly process. 1. Consecutive adsorption of anionic and cationic bipolar amphiphiles on charged surfaces", *Makromolekulare Chemie - Macromolecular Symposia* **1991**, *46*, 321.

[4] Decher, G., Hong, J. D., Schmitt, J., "Buildup of ultrathin multilayer films by a self-assembly process. 3. consecutively alternating adsorption of anionic and cationic polyelectrolytes on charged surfaces", *Thin Solid Films* **1992**, *210*, 831.

[5] Iler, R. K., "Multilayers of colloidal particles", *J. Colloid Interface Sci.* **1966**, *21*, 569.

[6] Zhao, W., Xu, J. J., Chen, H. Y., "Electrochemical biosensors based on layer-by-layer assemblies", *Electroanalysis* **2006**, *18*, 1737.

[7] Hammond, P. T., "Form and function in multilayer assembly: New applications at the nanoscale", *Adv. Mater.* **2004**, *16*, 1271.

[8] Jiang, C. Y., Markutsya, S., Pikus, Y., Tsukruk, V. V., "Freely suspended nanocomposite membranes as highly sensitive sensors", *Nat. Mater.* **2004**, *3*, 721.

[9] Ariga, K., Hill, J. P., Ji, Q. M., "Layer-by-layer assembly as a versatile bottom-up nanofabrication technique for exploratory research and realistic application", *Phys. Chem. Chem. Phys.* **2007**, *9*, 2319.

[10] Johnston, A. P. R., Cortez, C., Angelatos, A. S., Caruso, F., "Layer-by-layer engineered capsules and their applications", *Curr. Opin. Colloid Interface Sci.* **2006**, *11*, 203.

[11] Schmidt, D. J., Moskowitz, J. S., Hammond, P. T., "Electrically Triggered Release of a Small Molecule Drug from a Polyelectrolyte Multilayer Coating", *Chem. Mat.* **2010**, *22*, 6416.

[12] Podsiadlo, P., Kaushik, A. K., Arruda, E. M., Waas, A. M., Shim, B. S., Xu, J. D., Nandivada, H., Pumplin, B. G., Lahann, J., Ramamoorthy, A., Kotov, N. A., "Ultrastrong and stiff layered polymer nanocomposites", *Science* **2007**, *318*, 80.

[13] Podsiadlo, P., Shim, B. S., Kotov, N. A., "Polymer/clay and polymer/carbon nanotube hybrid organic-inorganic multilayered composites made by sequential layering of nanometer scale films", *Coord. Chem. Rev.* **2009**, *253*, 2835.

[14] Min, W. L., Jiang, B., Jiang, P., "Bioinspired Self-Cleaning Antireflection Coatings", *Adv. Mater.* **2008**, *20*, 3914.

[15] Dubas, S. T., Farhat, T. R., Schlenoff, J. B., "Multiple membranes from "true" polyelectrolyte multilayers", *J. Am. Chem. Soc.* **2001**, *123*, 5368.

[16] El Haitami, A. E., Martel, D., Ball, V., Nguyen, H. C., Gonthier, E., Labbe, P., Voegel, J. C., Schaaf, P., Senger, B., Boulmedais, F., "Effect of the Supporting Electrolyte Anion on the Thickness of PSS/PAH Multilayer Films and on Their Permeability to an Electroactive Probe", *Langmuir* **2009**, *25*, 2282.

[17] Schlenoff, J. B., "Retrospective on the Future of Polyelectrolyte Multilayers", *Langmuir* **2009**, *25*, 14007.

[18] Alivisatos, A. P., "Perspectives on the physical chemistry of semiconductor nanocrystals", *J. Phys. Chem.* **1996**, *100*, 13226.

[19] Cant, N. E., Critchley, K., Zhang, H. L., Evans, S. D., "Surface functionalisation for the self-assembly of nanoparticle/polymer multilayer films", *Thin Solid Films* **2003**, *426*, 31.

[20] Caruso, F., Mohwald, H., "Preparation and characterization of ordered nanoparticle and polymer composite multilayers on colloids", *Langmuir* **1999**, *15*, 8276.

[21] Kotov, N. A., "Layer-by-Layer Assembly of Nanoparticles and Nanocolloids: Intermolecular Interactions, Structure and Materials Perspectives", in *Multilayer Thin Films: Sequential Assembly of Nanocomposite Materials*, Decher, G., Schlenoff, J. B., Wiley-VCH, Weinheim **2003**.

[22] Granqvist, C. G., Hultaker, A., "Transparent and conducting ITO films: new developments and applications", *Thin Solid Films* **2002**, *411*, 1.

[23] Ginley, D. S., Bright, C., "Transparent conducting oxides", *MRS Bull.* **2000**, *25*, 15.

[24] Lewis, B. G., Paine, D. C., "Applications and processing of transparent conducting oxides", *MRS Bull.* **2000**, *25*, 22.

[25] Badeker, K., "Concerning the electricity conductibility and the thermoelectric energy of several heavy metal bonds", *Ann. Phys.-Berlin* **1907**, *22*, 749.

[26] Groth, R., Kauer, E., "Thermal insulation of sodium lamps", *Philips Tech. Rev.* **1965**, *26*, 105.

[27] Brehm, J. U., Winterer, M., Hahn, H., Michael, G., Gutsch, A., in *Materials Resarch Society Symposium Proceedings*, Vol. 704, **2001**, W 5.3.

[28] Hamberg, I., Granqvist, C. G., Berggren, K. F., Sernelius, B. E., Engstrom, L., "Band-gap widening in heavily Sn-doped In_2O_3", *Phys. Rev. B* **1984**, *30*, 3240.

[29] Burstein, E., "Anomalous optical absorption limit in InSb", *Phys. Rev.* **1954**, *93*, 632.

[30] Moss, T. S., "The interpretation of the properties of indium antimonide", presented at *Proceedings of the Physical Society of London Section B*, **1954**.

[31] Coutts, T. J., Young, D. L., Li, X. N., "Characterization of transparent conducting oxides", *MRS Bull.* **2000**, *25*, 58.

[32] Weiher, R. L., Ley, R. P., "Optical properties of indium oxide", *J. Appl. Phys.* **1966**, *37*, 299.

[33] Chopra, K. L., Major, S., Pandya, D. K., "Transparent conductors - a status review", *Thin Solid Films* **1983**, *102*, 1.

[34] You, Y. Z., Kim, Y., Choi, D. H., Jang, H. S., Lee, J. H., Kim, D., "Electrical and optical study of ITO films on glass and polymer substrates prepared by DC magnetron sputtering type negative metal ion beam deposition", *Mater. Chem. Phys.* **2008**, *107*, 444.

[35] Hsieh, S. J., Chen, C. C., Say, W. C., "Process for recovery of indium from ITO scraps and metallurgic microstructures", *Mater. Sci. Eng. B-Adv. Funct. Solid-State Mater.* **2009**, *158*, 82.

[36] George, M. W., U.S. Geological Survey, Mineral Commodity Summaries, **2005**.

[37] Homma, S., Miyamoto, A., Sakamoto, S., Kishi, K., Motoi, N., Yoshimura, K., "Pulmonary fibrosis in an individual occupationally exposed to inhaled indium-tin oxide", *Eur. Resp. J.* **2005**, *25*, 200.

[38] Homma, T., Ueno, T., Sekizawa, K., Tanaka, A., Hirata, M., "Interstitial pneumonia developed in a worker dealing with particles containing indium-tin oxide", *J. Occup. Health* **2003**, *45*, 137.

[39] Buhler, G., Tholmann, D., Feldmann, C., "One-pot synthesis of highly conductive indium tin oxide nanocrystals", *Adv. Mater.* **2007**, *19*, 2224.

[40] Ogi, T., Iskandar, F., Itoh, Y., Okuyama, K., "Characterization of dip-coated ITO films derived from nanoparticles synthesized by low-pressure spray pyrolysis", *J. Nanopart. Res.* **2006**, *8*, 343.

[41] Cosgrove, T., *Colloid science principles, methods and applications*, Blackwell Pub., Oxford, UK ; **2005**.

[42] Ottewill, R. H., "Stabilization of polymer colloid dispersions", in *Emulsion polymerization and emulsion polymers*, Lovell, P. A., El-Aasser, M. S., J. Wiley, New York : **1997**.

[43] Malvern Instruments, "Zeta potential measurement using laser Doppler electrophoresis (LDE)", http://www.malvern.com/LabEng/technology/zeta_potential/zeta_potential_LDE.htm

[44] Dobias, B., "Electrical Phenomena at the Solid-liquid Interface", in *Solid-liquid Dispersions*, Dobias, B., Qiu, X., Rybinski, W. v., Marcel Dekker, Inc., New York **1999**.

[45] Henry, D. C., "The cataphoresis of suspended particles Part I - The equation of cataphoresis", *Proc. R. soc. Lond. Ser. A-Contain. Pap. Math. Phys. Character* **1931**, *133*, 106.

[46] Lee, D., Gemici, Z., Rubner, M. F., Cohen, R. E., "Multilayers of oppositely charged SiO_2 nanoparticles: Effect of surface charge on multilayer assembly", *Langmuir* **2007**, *23*, 8833.

[47] Napper, D. H., *Polymeric stabilization of colloidal dispersions*, Academic Press, London ; **1983**.

[48] Gebhardt, J. E., Fuerstenau, D. W., "Adsorption of Polyacrylic-acid at Oxide Water Interfaces", **1983**, *7*, 221.

[49] Lu, K., Kessler, C. S., Davis, R. M., "Optimization of a nanoparticle suspension for freeze casting", *J. Am. Ceram. Soc.* **2006**, *89*, 2459.

[50] Zhu, X. W., Uchikoshi, T., Suzuki, T. S., Sakka, Y., "Effect of polyethylenimine on hydrolysis and dispersion properties of aqueous Si_3N_4 suspensions", *J. Am. Ceram. Soc.* **2007**, *90*, 797.

[51] Tang, F. Q., Uchikoshi, T., Wawa, K., Sakka, Y., "Effect of polyethylenimine on the dispersion and electrophoretic deposition of nano-sized titania aqueous suspensions", *J. Eur. Ceram. Soc.* **2006**, *26*, 1555.

[52] Dietrich, A., Neubrand, A., "Effects of particle size and molecular weight of polyethylenimine on properties of nanoparticulate silicon dispersions", *J. Am. Ceram. Soc.* **2001**, *84*, 806.

[53] Wang, J., Gao, L., "Adsorption of polyethylenimine on nanosized zirconia particles in aqueous suspensions", *J. Colloid Interface Sci.* **1999**, *216*, 436.

[54] Chaufer, B., Rabiller-Baudry, M., Bouguen, A., Labbe, J. P., Quemerais, A., "Spectroscopic characterization of zirconia coated by polymers with amine groups", *Langmuir* **2000**, *16*, 1852.

[55] Sanchez-Cortes, S., Berenguel, R. M., Madejon, A., Perez-Mendez, M., "Adsorption of polyethyleneimine on silver nanoparticles and its interaction with a plasmid DNA: A surface-enhanced Raman scattering study", *Biomacromolecules* **2002**, *3*, 655.

[56] Hammond, P. T., "Chemistry Directed Deposition via Electrostatic and Secondary Interactions: A Nonlithographic Approach to Patterned Polyelectrolyte Multilayer Systems", in *Multilayer Thin Films: Sequential Assembly of Nanocomposite Materials*, Decher, G., Schlenoff, J. B., Wiley-VCH, Weinheim **2003**.

[57] Choi, J., Rubner, M. F., "Influence of the degree of ionization on weak polyelectrolyte multilayer assembly", *Macromolecules* **2005**, *38*, 116.

[58] Shepherd, E. J., Kitchener, J. A., "The ionization of ethyleneimine and polyethyleneimine", *J. Chem. Soc.* **1956**, 2448.

[59] Katchalsky, A., Spitnik, P., "Potentiometric titrations of polymethacrylic acid", *J. Polym. Sci.* **1947**, *2*, 432.

[60] Nagasawa, M., Rice, S. A., "A chain model for polyelectrolytes. 5. A study of the effect of local charge density", *J. Am. Chem. Soc.* **1960**, *82*, 5070.

[61] Mandel, M., "Potentiometric titration of weak polyacids", *Eur. Polym. J.* **1970**, *6*, 807.

[62] Schlenoff, J. B., "Charge Balance and Transport in Polyelectrolyte Multilayers", in *Multilayer Thin Films: Sequential Assembly of Nanocomposite Materials*, Decher, G., Schlenoff, J. B., Wiley-VCH, Weinheim **2003**.

[63] Peng, C. Q., Thio, Y. S., Gerhardt, R. A., "Conductive paper fabricated by layer-by-layer assembly of polyelectrolytes and ITO nanoparticles", *Nanotechnology* **2008**, *19*, 505603.

[64] Lin, Z. Y., Renneckar, S., Hindman, D. P., "Nanocomposite-based lignocellulosic fibers 1. Thermal stability of modified fibers with clay-polyelectrolyte multilayers", *Cellulose* **2008**, *15*, 333.

[65] Ladam, G., Schaad, P., Voegel, J. C., Schaaf, P., Decher, G., Cuisinier, F., "In situ determination of the structural properties of initially deposited polyelectrolyte multilayers", *Langmuir* **2000**, *16*, 1249.

[66] Caruso, F., Lichtenfeld, H., Donath, E., Mohwald, H., "Investigation of electrostatic interactions in polyelectrolyte multilayer films: Binding of anionic fluorescent probes to layers assembled onto colloids", *Macromolecules* **1999**, *32*, 2317.

[67] Xing, Q., Eadula, S. R., Lvov, Y. M., "Cellulose fiber-enzyme composites fabricated through layer-by-layer nanoassembly", *Biomacromolecules* **2007**, *8*, 1987.

[68] Lee, D., Omolade, D., Cohen, R. E., Rubner, M. F., "pH-Dependent structure and properties of TiO_2/SiO_2 nanoparticle multilayer thin films", *Chem. Mat.* **2007**, *19*, 1427.

[69] Sperling, L. H., *Introduction to physical polymer science*, Wiley, Hoboken, N.J. : **2006**.

[70] Vandesteeg, H. G. M., Stuart, M. A. C., Dekeizer, A., Bijsterbosch, B. H., "Polyelectrolyte adsorption - A subtle balance of forces", *Langmuir* **1992**, *8*, 2538.

[71] Hoogeveen, N. G., Stuart, M. A. C., Fleer, G. J., "Polyelectrolyte adsorption on oxides .1. Kinetics and adsorbed amounts", *J. Colloid Interface Sci.* **1996**, *182*, 133.

[72] Lourenco, J. M. C., Ribeiro, P. A., do Rego, A. M. B., Fernandes, F. M. B., Moutinho, A. M. C., Raposo, M., "Counterions in poly(allylamine hydrochloride) and poly(styrene sulfonate) layer-by-layer films", *Langmuir* **2004**, *20*, 8103.

[73] Shi, X. Y., Sanedrin, R. J., Zhou, F. M., "Structural characterization of multilayered DNA and polylysine composite films: Influence of ionic strength of DNA solutions on the extent of DNA incorporation", *J. Phys. Chem. B* **2002**, *106*, 1173.

[74] Boddohi, S., Killingsworth, C. E., Kipper, M. J., "Polyelectrolyte multilayer assembly as a function of pH and ionic strength using the polysaccharides chitosan and heparin", *Biomacromolecules* **2008**, *9*, 2021.

[75] Schlenoff, J. B., Ly, H., Li, M., "Charge and mass balance in polyelectrolyte multilayers", *J. Am. Chem. Soc.* **1998**, *120*, 7626.

[76] Liu, G. M., Zhao, J. P., Sun, Q. Y., Zhang, G. Z., "Role of chain interpenetration in layer-by-layer deposition of polyelectrolytes", *J. Phys. Chem. B* **2008**, *112*, 3333.

[77] Sun, Q. L., Tong, Z., Wang, C. Y., Ren, B. Y., Liu, X. X., Zeng, F., "Charge density threshold for LbL self-assembly and small molecule diffusion in polyelectrolyte multilayer films", *Polymer* **2005**, *46*, 4958.

[78] Lefaux, C. J., Zimberlin, J. A., Dobrynin, A. V., Mather, P. T., "Polyelectrolyte spin assembly: Influence of ionic strength on the growth of multilayered thin films", *J. Polym. Sci. Pt. B-Polym. Phys.* **2004**, *42*, 3654.

[79] Lazzara, T. D., Lau, K. H. A., Abou-Kandil, A. I., Caminade, A. M., Majoral, J. P., Knoll, W., "Polyelectrolyte Layer-by-Layer Deposition in Cylindrical Nanopores", *ACS Nano* **2010**, *4*, 3909.

[80] Dubas, S. T., Schlenoff, J. B., "Factors controlling the growth of polyelectrolyte multilayers", *Macromolecules* **1999**, *32*, 8153.

[81] Shiratori, S. S., Rubner, M. F., "pH-dependent thickness behavior of sequentially adsorbed layers of weak polyelectrolytes", *Macromolecules* **2000**, *33*, 4213.

[82] Kozlovskaya, V., Kharlampieva, E., Jones, K., Lin, Z. Q., Tsukruk, V. V., "pH-Controlled Assembly and Properties of LbL Membranes from Branched Conjugated Poly(alkoxythiophene sulfonate) and Various Polycations", *Langmuir* **2010**, *26*, 7138.

[83] Ostrander, J. W., Mamedov, A. A., Kotov, N. A., "Two modes of linear layer-by-layer growth of nanoparticle-polyelectrolyte multilayers and different interactions in the layer-by-layer deposition", *J. Am. Chem. Soc.* **2001**, *123*, 1101.

[84] Tettey, K. E., Yee, M. Q., Lee, D., "Layer-by-Layer Assembly of Charged Particles in Nonpolar Media", *Langmuir* **2010**, *26*, 9974.

[85] Sruanganurak, A., Sanguansap, K., Tangboriboonrat, P., "Layer-by-layer assembled nanoparticles: A novel method for surface modification of natural rubber latex film", *Colloid Surf. A-Physicochem. Eng. Asp.* **2006**, *289*, 110.

[86] Wang, F., Peters, S., Guzda, J., Blunk, R. H., Angelopoulos, A. P., "Silica Nanoparticle Layer-by-Layer Assembly on Gold", *Langmuir* **2009**, *25*, 4384.

[87] Lee, S. W., Kim, B. S., Chen, S., Shao-Horn, Y., Hammond, P. T., "Layer-by-Layer Assembly of All Carbon Nanotube Ultrathin Films for Electrochemical Applications", *J. Am. Chem. Soc.* **2009**, *131*, 671.

[88] Liu, H. Y., Rusling, J. F., Hu, N. F., "Electroactive core-shell nanocluster films of heme proteins, polyelectrolytes, and silica nanoparticles", *Langmuir* **2004**, *20*, 10700.

[89] Liu, Y. J., Wang, Y. X., Claus, R. O., "Layer-by-layer ionic self-assembly of Au colloids into multilayer thin-films with bulk metal conductivity", *Chem. Phys. Lett.* **1998**, *298*, 315.

[90] Cho, J. H., Caruso, F., "Investigation of the interactions between ligand-stabilized gold nanoparticles and polyelectrolyte multilayer films", *Chem. Mat.* **2005**, *17*, 4547.

[91] Hicks, J. F., Seok-Shon, Y., Murray, R. W., "Layer-by-layer growth of polymer/nanoparticle films containing monolayer-protected gold clusters", *Langmuir* **2002**, *18*, 2288.

[92] Song, W. B., Okamura, M., Kondo, T., Uosaki, K., "Sequential layer-by-layer growth of Au nanoclusters protected by a mixed self-assembled monolayer with a polymer binding layer - Effects of pH and ionic strength of the polymer solution", *J. Electroanal. Chem.* **2008**, *612*, 105.

[93] Rogach, A. L., Koktysh, D. S., Harrison, M., Kotov, N. A., "Layer-by-layer assembled films of HgTe nanocrystals with strong infrared emission", *Chem. Mat.* **2000**, *12*, 1526.

[94] Pal, E., Sebok, D., Hornok, V., Dekany, I., "Structural, optical, and adsorption properties of ZnO_2/poly(acrylic acid) hybrid thin porous films prepared by ionic strength controlled layer-by-layer method", *J. Colloid Interface Sci.* **2009**, *332*, 173.

[95] Elzbieciak, M., Wodka, D., Zapotoczny, S., Nowak, P., Warszynski, P., "Characteristics of Model Polyelectrolyte Multilayer Films Containing Laponite Clay Nanoparticles", *Langmuir* **2010**, *26*, 277.

[96] Tang, Q. W., Li, Q. H., Lin, J. M., Fan, S. J., Hu, D., Wu, J. H., "High Conducting Multilayer Films From Poly(acrylic acid) and Graphite by Layer-by-Layer Self-Assembly", *Polym. Compos.* **2010**, *31*, 145.

[97] Su, P. G., Cheng, K. H., "Layer-by-layer assembly of mica and polyelectrolyte for use in low-humidity sensor", *Sens. Actuator B-Chem.* **2009**, *137*, 555.

[98] Lvov, Y., Ariga, K., Onda, M., Ichinose, I., Kunitake, T., "Alternate assembly of ordered multilayers of SiO_2 and other nanoparticles and polyions", *Langmuir* **1997**, *13*, 6195.

[99] Serizawa, T., Takeshita, H., Akashi, M., "Electrostatic adsorption of polystyrene nanospheres onto the surface of an ultrathin polymer film prepared by using an alternate adsorption technique", *Langmuir* **1998**, *14*, 4088.

[100] Sennerfors, T., Bogdanovic, G., Tiberg, F., "Formation, chemical composition, and structure of polyelectrolyte-nanoparticle multilayer films", *Langmuir* **2002**, *18*, 6410.

[101] Johnson, C. A., Lenhoff, A. M., "Adsorption of charged latex particles on mica studied by atomic force microscopy", *J. Colloid Interface Sci.* **1996**, *179*, 587.

[102] Alazemi, M., Dutta, I., Wang, F., Blunk, R. H., Angelopoulos, A. P., "Electrically Conductive Thin Films Prepared from Layer-by-Layer Assembly of Graphite Platelets", *Adv. Funct. Mater.* **2009**, *19*, 1118.

[103] Su, P. G., Lee, C. T., Chou, C. Y., Cheng, K. H., Chuang, Y. S., "Fabrication of flexible NO_2 sensors by layer-by-layer self-assembly of multi-walled carbon nanotubes and their gas sensing properties", *Sens. Actuator B-Chem.* **2009**, *139*, 488.

[104] Kim, J. H., Fujita, S., Shiratori, S., "Fabrication and characterization of TiO_2 thin film prepared by a layer-by-layer self-assembly method", *Thin Solid Films* **2006**, *499* 83.

[105] Elbert, D. L., Herbert, C. B., Hubbell, J. A., "Thin polymer layers formed by polyelectrolyte multilayer techniques on biological surfaces", *Langmuir* **1999**, *15*, 5355.

[106] Picart, C., Lavalle, P., Hubert, P., Cuisinier, F. J. G., Decher, G., Schaaf, P., Voegel, J. C., "Buildup mechanism for poly(L-lysine)/hyaluronic acid films onto a solid surface", *Langmuir* **2001**, *17*, 7414.

[107] Pardo-Yissar, V., Katz, E., Lioubashevski, O., Willner, I., "Layered polyelectrolyte films on Au electrodes: Characterization of electron-transfer features at the charged polymer interface and application for selective redox reactions", *Langmuir* **2001**, *17*, 1110.

[108] Salomaki, M., Vinokurov, I. A., Kankare, J., "Effect of temperature on the buildup of polyelectrolyte multilayers", *Langmuir* **2005**, *21*, 11232.

[109] Fu, J. H., Ji, J., Shen, L. Y., Kueller, A., Rosenhahn, A., Shen, J. C., Grunze, M., "pH-Amplified Exponential Growth Multilayers: A Facile Method to Develop Hierarchical Micro- and Nanostructured Surfaces", *Langmuir* **2009**, *25*, 672.

[110] McAloney, R. A., Sinyor, M., Dudnik, V., Goh, M. C., "Atomic force microscopy studies of salt effects on polyelectrolyte multilayer film morphology", *Langmuir* **2001**, *17*, 6655.

[111] Kujawa, P., Moraille, P., Sanchez, J., Badia, A., Winnik, F. M., "Effect of molecular weight on the exponential growth and morphology of hyaluronan/chitosan multilayers: A surface plasmon resonance spectroscopy and atomic force microscopy investigation", *J. Am. Chem. Soc.* **2005**, *127*, 9224.

[112] Picart, C., Mutterer, J., Richert, L., Luo, Y., Prestwich, G. D., Schaaf, P., Voegel, J. C., Lavalle, P., "Molecular basis for the explanation of the exponential growth of polyelectrolyte multilayers", *Proc. Natl. Acad. Sci. U. S. A.* **2002**, *99*, 12531.

[113] Lavalle, P., Voegel, J. C., Vautier, D., Senger, B., Schaaf, P., Ball, V., "Dynamic aspects of films prepared by a sequential deposition of species: perspectives for smart and responsive materials", *Adv. Mater.* **2011**, *23*, 1191.

[114] Lavalle, P., Gergely, C., Cuisinier, F. J. G., Decher, G., Schaaf, P., Voegel, J. C., Picart, C., "Comparison of the structure of polyelectrolyte multilayer films exhibiting a linear and an exponential growth regime: An in situ atomic force microscopy study", *Macromolecules* **2002**, *35*, 4458.

[115] Richert, L., Lavalle, P., Payan, E., Shu, X. Z., Prestwich, G. D., Stoltz, J. F., Schaaf, P., Voegel, J. C., Picart, C., "Layer by layer buildup of polysaccharide films: Physical chemistry and cellular adhesion aspects", *Langmuir* **2004**, *20*, 448.

[116] Podsiadlo, P., Michel, M., Lee, J., Verploegen, E., Kam, N. W. S., Ball, V., Qi, Y., Hart, A. J., Hammond, P. T., Kotov, N. A., "Exponential growth of LBL films with incorporated inorganic sheets", *Nano Lett.* **2008**, *8*, 1762.

[117] Liu, X. K., Zhou, L., Liu, F., Ji, M. Y., Tang, W. G., Pang, M. J., Sun, J. Q., "Exponential growth of layer-by-layer assembled coatings with well-dispersed ultrafine nanofillers: a facile route to scratch-resistant and transparent hybrid coatings", *J. Mater. Chem.* **2010**, *20*, 7721.

[118] Peng, C. Q., Thio, Y. S., Gerhardt, R. A., "Enhancing the Layer-by-Layer Assembly of Indium Tin Oxide Thin Films by Using Polyethyleneimine", *J. Phys. Chem. C* **2010**, *114*, 9685.

[119] Park, Y. T., Ham, A. Y., Grunlan, J. C., "High Electrical Conductivity and Transparency in Deoxycholate-Stabilized Carbon Nanotube Thin Films", *J. Phys. Chem. C* **2010**, *114*, 6325.

[120] Lvov, Y., Ariga, K., Ichinose, I., Kunitake, T., "Assembly of Multicomponent Protein Films by Means of Electrostatic Layer-by-layer Adsorption", *J. Am. Chem. Soc.* **1995**, *117*, 6117.

[121] Podsiadlo, P., Michel, M., Critchley, K., Srivastava, S., Qin, M., Lee, J. W., Verploegen, E., Hart, A. J., Qi, Y., Kotov, N. A., "Diffusional Self-Organization in Exponential Layer-By-Layer Films with Micro- and Nanoscale Periodicity", *Angew. Chem.-Int. Edit.* **2009**, *48*, 7073.

[122] Smith, M., *March's advanced organic chemistry: Reactions, mechanisms, and structure*, Wiley-Interscience, Hoboken, N.J. **2007**.

[123] Caruso, F., Spasova, M., Saigueirino-Maceira, V., Liz-Marzan, L. M., "Multilayer assemblies of silica-encapsulated gold nanoparticles on decomposable colloid templates", *Adv. Mater.* **2001**, *13*, 1090.

[124] Evans, D. F., *The colloidal domain : where physics, chemistry, biology, and technology meet*, Wiley-VCH, New York **1999**.

[125] Sauerbrey, G., "Berwendung Von Schwingquarzen Zur Wagung Dunner Schichten Und Zur Mikrowagung", *Z. Phys. Chem.* **1959**, *155*, 206.

[126] Luo, E. Z., Xu, J. B., Wu, W., Wilson, I. H., Zhao, B., Yan, X., "Identifying conducting phase from the insulating matrix in percolating metal-insulator nanocomposites by conducting atomic force microscopy", *Appl. Phys. A-Mater. Sci. Process.* **1998**, *66*, S1171.

[127] Yang, H. C., Shin, T. J., Ling, M. M., Cho, K., Ryu, C. Y., Bao, Z. N., "Conducting AFM and 2D GIXD studies on pentacene thin films", *J. Am. Chem. Soc.* **2005**, *127*, 11542.

[128] Gerhardt, R. A., "Impedance Spectroscopy and Mobility Spectra", in *Encyclopedia of Condensed Matter Physics*, Bassani, G., Liedl, G., Wyder, P., Elsevier, Oxford **2005**, 350.

[129] Warad, H. C., Ghosh, S. C., Hemtanon, B., Thanachayanont, C., Dutta, J., "Luminescent nanoparticles of Mn doped ZnS passivated with sodium hexametaphosphate", *Sci. Technol. Adv. Mater.* **2005**, *6*, 296.

[130] Le Guevel, X., Wang, F. Y., Stranik, O., Nooney, R., Gubala, V., McDonagh, C., MacCraith, B. D., "Synthesis, Stabilization, and Functionalization of Silver Nanoplates for Biosensor Applications", *J. Phys. Chem. C* **2009**, *113*, 16380.

[131] Rogach, A. L., Koktysh, D. S., Harrison, M., Kotov, N. A., "Layer-by-layer assembled films of HgTe nanocrystals with strong infrared emission", *Chem. Mater.* **2000**, *12*, 1526.

[132] Cant, N. E., Zhang, H. L., Critchley, K., Mykhalyk, T. A., Davies, G. R., Evans, S. D., "Fabrication and characterization of self-assembled nanoparticle/polyelectrolyte multilayer films", *J. Phys. Chem. B* **2003**, *107*, 13557.

[133] Zhang, J. X., Xu, Q., Ye, F., Lin, Q. L., Jiang, D. L., Iwasa, M., "Effect of citric acid on the adsorption behavior of polyethylene imine (PEI) and the relevant stability of SiC slurries", *Colloid Surf. A* **2006**, *276*, 168.

[134] Meszaros, R., Thompson, L., Bos, M., de Groot, P., "Adsorption and electrokinetic properties of polyethylenimine on silica surfaces", *Langmuir* **2002**, *18*, 6164.

[135] Socrates, G., *Infrared and Raman characteristic group frequencies: Tables and charts*, Wiley, Chichester, U.K. **2001**.

[136] Klonkowski, A. M., Grobelna, B., Widernik, T., Jankowska-Frydel, A., Mozgawa, W., "The coordination state of copper(II) complexes anchored and grafted onto the surface of organically modified silicates", *Langmuir* **1999**, *15*, 5814.

[137] Rao, P. S., Smitha, B., Sridhar, S., Krishnaiah, A., "Preparation and performance of poly(vinyl alcohol)/polyethyleneimine blend membranes for the dehydration of 1,4-dioxane by pervaporation: Comparison with glutaraldehyde cross-linked membranes", *Sep. Purif. Technol.* **2006**, *48*, 244.

[138] Arkas, M., Tsiourvas, D., "Organic/inorganic hybrid nanospheres based on hyperbranched poly(ethylene imine) encapsulated into silica for the sorption of toxic metal ions and polycyclic aromatic hydrocarbons from water", *J. Hazard. Mater.* **2009**, *170*, 35.

[139] Golander, C. G., Eriksson, J. C., "ESCA studies of the adsorption of polyethyleneimine and glutaraldehyde-reacted polyethyleneimine on polyethylene and mica surfaces ", *J. Colloid Interface Sci.* **1987**, *119*, 38.

[140] Tsyganenko, A. A., Pozdnyakov, D. V., Filimonov, V. N., "Infrared study of surface species arising from ammonia adsorption on oxide surfaces", *J. Mol. Struct.* **1975**, *29*, 299.

[141] Lu, Z. H., Eadula, S., Zheng, Z. G., Xu, K., Grozdits, G., Lvov, Y., "Layer-by-layer nanoparticle coatings on lignocellulose wood microfibers", *Colloid Surf. A* **2007**, *292*, 56.

[142] Schneider, G., Decher, G., "Functional core/shell nanoparticles via layer-by-layer assembly. investigation of the experimental parameters for controlling particle aggregation and for enhancing dispersion stability", *Langmuir* **2008**, *24*, 1778.

[143] Sui, Z. J., Schlenoff, J. B., "Phase separations in pH-responsive polyelectrolyte multilayers: Charge extrusion versus charge expulsion", *Langmuir* **2004**, *20*, 6026.

[144] Itano, K., Choi, J. Y., Rubner, M. F., "Mechanism of the pH-induced discontinuous swelling/deswelling transitions of poly(allylamine hydrochloride)-containing polyelectrolyte multilayer films", *Macromolecules* **2005**, *38*, 3450.

[145] Jeon, J., Panchagnula, V., Pan, J., Dobrynin, A. V., "Molecular dynamics simulations of mutilayer films of polyelectrolytes and nanoparticles", *Langmuir* **2006**, *22*, 4629.

[146] Rodriguez, M. C., Kawde, A. N., Wang, J., "Aptamer biosensor for label-free impedance spectroscopy detection of proteins based on recognition-induced switching of the surface charge", *Chem. Commun.* **2005**, 4267.

[147] Scribner Associates Inc. Zview Software

[148] Peng, C. Q., Thio, Y. S., Gerhardt, R. A., "The Effect of Precursor-layer Surface Charge on the Layer-by-Layer Assembly of Polyelectrolyte / Nanoparticle Multilayers", *Langmuir* **2011**, Submitted.

[149] Barsoukov, E., Macdonald, J. R., *Impedance spectroscopy : theory, experiment, and applications*, Wiley-Interscience, Hoboken, N.J. **2005**.

[150] Chen, K. M., Jiang, X. P., Kimerling, L. C., Hammond, P. T., "Selective self-organization of colloids on patterned polyelectrolyte templates", *Langmuir* **2000**, *16*, 7825.

[151] Srivastava, S., Podsiadlo, P., Critchley, K., Zhu, J., Qin, M., Shim, B. S., Kotov, N. A., "Single-Walled Carbon Nanotubes Spontaneous Loading into Exponentially Grown LBL Films", *Chem. Mat.* **2009**, *21*, 4397.

[152] Lauter, V., Ambaye, H., Goyette, R., Lee, W. T. H., Parizzi, A., "Highlights from the magnetism reflectometer at the SNS", *Physica B* **2009**, *404*, 2543.

[153] http://www.sns.gov/instruments/SNS/factsheets/Instrument_4a.pdf

[154] Peng, C. Q., Thio, Y. S., Gerhardt, R. A., Ambaye, H., Lauter, V., "pH-Controlled Exponential Layer-by-layer Growth of Polyelectrolytes / Nanoparticles Multilayers", *Chem. Mat.* **2011**, Submitted.

[155] Evans, D. F., *The colloidal domain: where physics, chemistry, biology, and technology meet*, VCH Publishers, New York, NY **1994**.

[156] Laugel, N., Betscha, C., Winterhalter, M., Voegel, J. C., Schaaf, P., Ball, V., "Relationship between the growth regime of polyelectrolyte multilayers and the polyanion/polycation complexation enthalpy", *J. Phys. Chem. B* **2006**, *110*, 19443.

[157] Hubsch, E., Ball, V., Senger, B., Decher, G., Voegel, J. C., Schaaf, P., "Controlling the growth regime of polyelectrolyte multilayer films: Changing from exponential to linear growth by adjusting the composition of polyelectrolyte mixtures", *Langmuir* **2004**, *20*, 1980.

[158] Boulmedais, F., Ball, V., Schwinte, P., Frisch, B., Schaaf, P., Voegel, J. C., "Buildup of exponentially growing multilayer polypeptide films with internal secondary structure", *Langmuir* **2003**, *19*, 440.

[159] Porcel, C., Lavalle, P., Ball, V., Decher, G., Senger, B., Voegel, J. C., Schaaf, P., "From exponential to linear growth in polyelectrolyte multilayers", *Langmuir* **2006**, *22*, 4376.

[160] Porcel, C., Lavalle, P., Decher, G., Senger, B., Voegel, J. C., Schaaf, P., "Influence of the polyelectrolyte molecular weight on exponentially growing multilayer films in the linear regime", *Langmuir* **2007**, *23*, 1898.

[161] Penfold, J., Thomas, R. K., "The application of the specular reflection of neutrons to the study of surfaces and interfaces", *J. Phys.-Condes. Matter* **1990**, *2*, 1369.

[162] Agarwal, M., Lvov, Y., Varahramyan, K., "Conductive wood microfibres for smart paper through layer-by-layer nanocoating", *Nanotechnology* **2006**, *17*, 5319.

[163] Wistrand, I., Lingstrom, R., Wagberg, L., "Preparation of electrically conducting cellulose fibres utilizing polyelectrolyte multilayers of poly(3,4-ethylenedioxythiophene): poly(styrene sulphonate) and poly(allyl amine)", *Eur. Polym. J.* **2007**, *43*, 4075.

[164] Fukahori, S., Iguchi, Y., Ichiura, H., Kitaoka, T., Tanaka, H., Wariishi, H., "Effect of void structure of photocatalyst paper on VOC decomposition", *Chemosphere* **2007**, *66*, 2136.

[165] Sarrazin, P., Valecce, L., Beneventi, D., Chaussy, D., Vurth, L., Stephan, O., "Photoluminescent paper based on poly(fluorene-co-fluorenone) particles adsorption on modified cellulose fibers", *Adv. Mater.* **2007**, *19*, 3291.

[166] Zakaria, S., Ong, B. H., Ahmad, S. H., Abdullah, M., Yamauchi, T., "Preparation of lumen-loaded kenaf pulp with magnetite (Fe_3O_4)", *Mater. Chem. Phys.* **2005**, *89*, 216.

[167] Bhardwaj, N. K., Duong, T. D., Hoang, V., Nguyen, K. L., "Determination of fiber charge components of Lo-Solids unbleached kraft pulps", **2004**, *274*, 543.

[168] Vandeven, T. G. M., "Kinetic aspects of polymer and polyelectrolyte adsorption on surfaces", *Adv. Colloid Interface Sci.* **1994**, *48*, 121.

[169] TAPPI Standard T 205: Forming Handsheets for Physical Tests of Pulp

[170] Biermann, B. J., *Handbook of Pulping and Papermaking*, Academic Press, **1996**.

[171] Patterson, T. Pulp and Paper Manufacturing II Class notes Spring 2008

[172] Shigesato, Y., Paine, D. C., "A microstructural study of low-resistivity tin-doped indium oxide prepared by DC magnetron sputtering", *Thin Solid Films* **1994**, *238*, 44.

[173] Kim, D., Han, Y., Cho, J. S., Koh, S. K., "Low temperature deposition of ITO thin films by ion beam sputtering", *Thin Solid Films* **2000**, *377*, 81.

[174] Kim, H., Gilmore, C. M., Pique, A., Horwitz, J. S., Mattoussi, H., Murata, H., Kafafi, Z. H., Chrisey, D. B., "Electrical, optical, and structural properties of indium-tin-oxide thin films for organic light-emitting devices", *J. Appl. Phys.* **1999**, *86*, 6451.

[175] George, J., Menon, C. S., "Electrical and optical properties of electron beam evaporated ITO thin films", *Surf. Coat. Technol.* **2000**, *132*, 45.

[176] Ma, H. L., Zhang, D. H., Ma, P., Win, S. Z., Li, S. Y., "Preparation and Properties of Transparent Conducting Indium Tin Oxide-Films Deposited by Reactive Evaporation", *Thin Solid Films* **1995**, *263*, 105.

[177] Chandrasekhar, R., Choy, K. L., "Innovative and cost-effective synthesis of indium tin oxide films", *Thin Solid Films* **2001**, *398*, 59.

[178] Ota, R., Seki, S., Sawada, Y., Ogawa, M., Nishide, T., Shida, A., Ide, M., "Indium-tin-oxide films prepared by dip coating using an ethanol solution of indium chloride and tin chloride", *Surf. Coat. Technol.* **2003**, *169*, 521.

[179] Smits, F. M., "Measurement of sheet resistivities with the 4-point probe", *Bell System Technical Journal* **1958**, *37*, 711.

[180] Starr, C., Evers, C. A., Starr, L., *Biology: Concepts and Applications*, Thomson Brooks/Cole, **2005**.

[181] Bravo, J., Zhai, L., Wu, Z. Z., Cohen, R. E., Rubner, M. F., "Transparent superhydrophobic films based on silica nanoparticles", *Langmuir* **2007**, *23*, 7293.

[182] Li, X. Y., Du, X., He, J. H., "Self-Cleaning Antireflective Coatings Assembled from Peculiar Mesoporous Silica Nanoparticles", *Langmuir* **2010**, *26*, 13528.

[183] Gilstrap, R. A., Capozzi, C. J., Carson, C. G., Gerhardt, R. A., Summers, C. J., "Synthesis of a Nonagglomerated Indium Tin Oxide Nanoparticle Dispersion", *Adv. Mater.* **2008**, *20*, 4163.

[184] Capozzi, C. J., Ivanov, I. N., Joshi, S., Gerhardt, R. A., "The effect of the atmosphere on the optical properties of as-synthesized colloidal indium tin oxide", *Nanotechnology* **2009**, *20*, 7.

[185] Boal, A. K., Rotello, V. M., "Intra- and intermonolayer hydrogen bonding in amide-functionalized alkanethiol self-assembled monolayers on gold nanoparticles", *Langmuir* **2000**, *16*, 9527.

[186] Grabar, K. C., Freeman, R. G., Hommer, M. B., Natan, M. J., "Preparation and characterization of Au colloid monolayers", *Anal. Chem.* **1995**, *67*, 735.

[187] Zhang, F. X., Srinivasan, M. P., "Layer-by-layer assembled gold nanoparticle films on amine-terminated substrates", *J. Colloid Interface Sci.* **2008**, *319*, 450.

[188] Jiang, C. Y., Markutsya, S., Tsukruk, V. V., "Collective and individual plasmon resonances in nanoparticle films obtained by spin-assisted layer-by-layer assembly", *Langmuir* **2004**, *20*, 882.

[189] Hostetler, M. J., Templeton, A. C., Murray, R. W., "Dynamics of place-exchange reactions on monolayer-protected gold cluster molecules", *Langmuir* **1999**, *15*, 3782.

[190] Boal, A. K., Das, K., Gray, M., Rotello, V. M., "Monolayer exchange chemistry of gamma-Fe_2O_3 nanoparticles", *Chem. Mat.* **2002**, *14*, 2628.

[191] Simard, J., Briggs, C., Boal, A. K., Rotello, V. M., "Formation and pH-controlled assembly of amphiphilic gold nanoparticles", *Chem. Commun.* **2000**, 1943.

[192] Brown, L. O., Hutchison, J. E., "Controlled growth of gold nanoparticles during ligand exchange", *J. Am. Chem. Soc.* **1999**, *121*, 882.

[193] Yu, Z. N., Gao, H., Wu, W., Ge, H. X., Chou, S. Y., "Fabrication of large area subwavelength antireflection structures on Si using trilayer resist nanoimprint lithography and liftoff", *J. Vac. Sci. Technol. B* **2003**, *21*, 2874.

[194] Huang, Y. F., Chattopadhyay, S., Jen, Y. J., Peng, C. Y., Liu, T. A., Hsu, Y. K., Pan, C. L., Lo, H. C., Hsu, C. H., Chang, Y. H., Lee, C. S., Chen, K. H., Chen, L. C., "Improved broadband and quasi-omnidirectional anti-reflection properties with biomimetic silicon nanostructures", *Nat. Nanotechnol.* **2007**, *2*, 770.

[195] Tuteja, A., Choi, W., Mabry, J. M., McKinley, G. H., Cohen, R. E., "Robust omniphobic surfaces", *Proc. Natl. Acad. Sci. U. S. A.* **2008**, *105*, 18200.

[196] Zhai, L., Cebeci, F. C., Cohen, R. E., Rubner, M. F., "Stable superhydrophobic coatings from polyelectrolyte multilayers", *Nano Lett.* **2004**, *4*, 1349.